Characteristics of the Venus lower atmosphere at different altitudes and mixing properties computed using Direct Numerical Simulation

Stefano Morellina

Jet Propulsion Laboratory, California Institute of Technology, Pasadena, CA 91109, USA

2018

Contents

1 Introduction

Venus, the hottest planet in the Solar System, is still subject of intense research, and due to the scant number of successful missions conducted on the planet, several aspects of its atmosphere remain mysterious. The origin of the variety of the species detected on the Venus surface is still not known; the species could be present as product of local chemical reactions, or being transported from upper layers of the atmosphere. Venus missions have increasingly diminished over time, after several mission failures due to the extremes environment conditions on its surface. The exploration has actually focused on other target planets like Mars, but the exploration of Venus is still a topic of discussion and there are mission proposals for the future. This planet could be full of surprises; having the most Earth-like atmosphere between 50-65 km above the surface, with 21% oxygen, 78% nitrogen, 0.5 bar of pressure and 27 °C of temperature, it is thought that Venus could even host the life, perhaps bacterial colonies could be present similar to those found in clouds on Earth. Moreover, the study of the Venus atmosphere and the understanding of the mechanisms tied to the runaway greenhouse effect that have affected the planet is of great interest for better understanding the climate change on Earth, and perhaps provide us with a clearer vision of the past and the future of our planet.

During the early Venus history, the Venus Planetary Boundary Layer (PBL) was pivotal in the establishment of the planet super-rotation. Indeed, the PBL is one of the governing elements in determining the characteristics of the planet's upper troposphere and tropopause. Thus, understanding the Venus PBL is crucial in the Venus exploration. The purpose of this study is to highlight some of the crucial aspects of the Venus lower atmosphere. Starting from available probe data regarding the chemical composition of the atmosphere, pressure and temperature values at different altitudes, and from direct and indirect measurements of winds speed, computations of the atmosphere properties such as density, viscosity, thermal conductivity, and an evaluation of the characteristic non-dimensional numbers such as the Reynolds number and the Prandtl number have been here conducted underlining the distribution of these quantities with the altitude. A thermodynamic stability analysis was conducted to determine the thermodynamic regime of the Venus lower atmosphere; by computing the thermodynamic stability locus of the mixture, and finding the regions of stability and instability. Finally, a fundamental study of the mixing properties of the species present in the Venus lower atmosphere at different altitudes has been conducted using Direct Numerical Simulation, a computational method wherein all scales overwhelmingly responsible for the dissipation are resolved.

2 Calculation and validation of the mixture density

A literature search indicated that to investigate on the characteristics of the Venus lower atmosphere, a 7-species mixture can be considered representative. In table 1 are listed the molar fraction values of the composition, that are an average of data from several missions on Venus [22]. The pressure of 92 bars and the temperature of 735 Kelvins are representative of the conditions at the Venus surface [25, 7].

Species	Molar Fraction	Critical pressure [bar]	Critical temperature [K]
CO_2	0.964816395	73.74	304.12
N_2	0.035	33.98	126.2
SO_2	0.00015	78.84	430.8
H_2O	0.00003	220.64	647.14
H_2S	$3x10^{-6}$	89.63	373.4
HCl	$6x10^{-7}$	83.1	324.69
HF	$5x10^{-9}$	65.0	461.0

Table 1: 7-species model for the Venus Lower Atmosphere [22]. The critical pressure and temperature conditions for the species are listed [37].

The mixture density is among the quantities governing a variety of phenomena, the knowledge of which is required to estimate the dynamic characteristics of the atmosphere and to implement accurate models for several engineering purposes, such as simulating atmospheric entry. For a mixture of several species, the thermodynamic state is completely defined by four variables: pressure, temperature, density and molar fraction, which are related by the Equation of State (EOS). Despite the perfect gas EOS, i.e. $p = \rho R_u T$, where p is the pressure, ρ is the density, T is the temperature, and $R_u = 8.314$ [J/(mol·K)] is the universal gas constant, being widely used in most engineering applications, this equation is not in general accurate to describe the evolution of the thermodynamic variables of fluids in supercritical conditions, where real gas effects typically appear. Supercritical fluids are in the thermodynamic (T, p) plane at temperatures and pressures above its critical point, where there is no distinction between liquid and gas phases; and in this regime, changes of thermodynamic and transport properties such as density, enthalpy, isobaric specific heat and viscosity are involved compared to sub-critical conditions [39]. An illustration of the variety of thermodynamic states in which a fluid can be found is presented in figure 1.
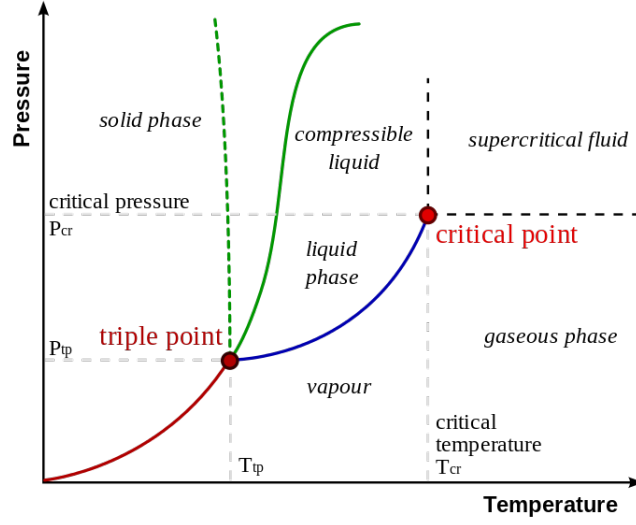
Figure 1: Pressure-temperature phase diagram with the various regions of the thermodynamic regime.

Since most of the species forming the Venus lower atmosphere have critical points below the prevailing conditions (refer to table 1), the cubic Peng-Robinson Equation of State (PR-EOS) was selected for the density computation, in order to take into account possible real-gas effects. The mixture density is therefore obtained by resolving:

$$p = \frac{R_u T}{(v_{pr} - b_{mix})} - \frac{a_{mix}}{(v_{pr}^2 + 2b_{mix}v_{pr} - b_{mix}^2)} \tag{1}$$

For the molar volume, v_{pr}, and computing $\rho = m/v_{pr}$, where m is the molar mass of the mixture. Here T is the temperature of the mixture, is the molar PR volume, a_{mix} and b_{mix} are function of T and the molar fraction X_i and are defined as follows:

$$a_{mix} = \sum_{\alpha}\sum_{\gamma} X_\alpha X_\gamma a_{\alpha\gamma}(T), \quad b_{mix} = \sum_{\alpha} X_\alpha b_\alpha; \tag{2}$$

where indices do not follow the Einstein notation, and

$$a_{\alpha\gamma} = (1 - k'_{\alpha\gamma})\sqrt{\alpha_{\alpha\alpha}\gamma_{\gamma\gamma}}, \tag{3}$$

$$\alpha_{\alpha\alpha}(T) = 0.457236(R_u T_{c,\alpha})^2 \frac{\left[1 + c_\alpha \left(1 - \sqrt{T_{red,\alpha}}\right)\right]^2}{p_{c,\alpha}} \tag{4}$$

$$c_\alpha = 0.37464 + 1.5422\Omega_\alpha - 0.26992\Omega_\alpha^2 \tag{5}$$

$$T_{c,\alpha\gamma} = (1 - k_{\alpha\gamma})\sqrt{T_{c,\alpha}T_{c,\gamma}} \text{ with } k_{\alpha\alpha} = 0 \tag{6}$$

$$v_{c,\alpha\gamma} = \frac{1}{8}(v_{c,\alpha}^{1/3} + v_{c,\gamma}^{1/3})^3 \tag{7}$$

$$Z_{c,\alpha\gamma} = \frac{1}{2}(Z_{c,\alpha} + Z_{c,\gamma}) \tag{8}$$

$$p_{c,\alpha\gamma} = \frac{R_u T_{c,\alpha\gamma} Z_{c,\alpha\gamma}}{v_{c,\alpha\gamma}} \tag{9}$$

Here $T_{red,\alpha} \equiv \frac{T}{T_{c,\alpha}}$, $T_{c,\alpha}$ is the critical temperature, $T_{red,\alpha\gamma} \equiv \frac{T}{T_{c,\alpha\gamma}}$, $Z_{c,\alpha}$ being the critical compressibility factor defined as $Z = p/(\rho T R_u/m)$, $v_{c,\alpha}$ being the critical volume, $p_{c,\alpha}$ is the critical pressure and Ω_α is the acentric factor. The relationship between parameters $k_{\alpha\gamma}$ and $k'_{\alpha\gamma}$ is

$$(1 - k_{\alpha\gamma}) = (1 - k'_{\alpha\gamma})\frac{(v_{c,\alpha}v_{c,\gamma})^{1/2}}{v_{c,\alpha\gamma}} \tag{10}$$

All values of $k'_{\alpha\gamma}$ used here are listed in table 2; for all pairs not listed in this table, $k'_{\alpha\gamma} = 0$ is used. The equations here above are the mixing rules which specify how the equation of state of the pure components will be combined to evaluate the properties of the mixture. Solving

Species 1	Species 2	k'
CO_2	N_2	-0.017
CO_2	H_2O	0.12
CO_2	H_2S	0.0974
N_2	SO_2	0.08
N_2	H_2S	0.1767
H_2O	H_2S	0.04

Table 2: Binary interaction parameters when the first species has a relatively low molar mass. Parameters not listed are set to be null. References Knapp et al. [24].

the PR-EOS for the mixture molar volume v_{pr}, the mixture mass density is easily obtained as follows:

$$\rho = \frac{m}{v_{pr}} \tag{11}$$

where ρ is in [kg/m^3], m is:

$$m = \sum_{\alpha} m_\alpha X_\alpha \tag{12}$$

Here, m_α is the species molar mass. Usually to find the roots of a cubic EOS it is rewritten as function of the compressibility factor Z [43].

$$Z^3 + p_1 Z^2 + p_2 Z + p_3 = 0 \tag{13}$$

When multiple real roots are present, the smallest root is considered the liquid root, the mid root is considered unstable and it is discarded, and the largest root is taken as vapor root. The values of the molar mass, molar volume and density obtained for the 7-species mixture (tab. 1), are summarized in table 3.

Mixture molar mass [$kg/kmol$]	43.4523
Mixture compressibility factor	1.0095
Mixture molar volume [$m^3/kmol$]	0.6706
Mixture density [kg/m^3]	64.7972

Table 3: Mixture molar mass, compressibility factor, molar volume and density computed through resolution of the PR-EOS.

Therefore, at the temperature and pressure conditions present on the Venus surface, the mixture has a compressibility factor nearly unitary. Further computations have shown the same behavior at different altitudes, for the first 65 km, showing similar results to those obtained with coarser models and already present in literature [40]. This suggest that a perfect-gas model would still be accurate enough to describe the evolution of the mixture thermodynamic properties, depending on the accuracy required from the application. Nevertheless, the real-gas PR-EOS is retained in every computation of this study.

In order to evaluate the value of the mixture density computed from the PR-EOS, a comparison with the generalized compressibility factor Z has been done (figure 4.3 in [37]), where the reduced temperature, T_c and pressure, p_c, of the carbon dioxide is used. The generalized compressibility chart shows a value of Z around unity, similar to the value obtained from the resolution of the PR-EOS. A more refined check on density is given from the comparison with data from NIST [31] database, which provide an accurate data bank of the thermophysical properties of several fluids in a certain range of temperatures and pressures. Since carbon dioxide and nitrogen represent over 99,9% of the mixture in molar fraction, a rough average of the density values from NIST database, weighted on molar fractions of these species has been performed, and the averaged value was then compared to that computed from the PR-EOS

for the 7-species model. Density values compare favorably, as shown in table 4, indicating reliability of the PR-EOS to model the mixture.

NIST database	Density $[kg/m^3]$	PR-EOS (7-Species)	error
CO_2	65.894		
N_2	39.808		
CO_2-N_2mix	64.9967	64.7972	0.3%

Table 4: Comparison between the mixture density computed by resolution of the PR-EOS and the density of a molar mass-weighted average of a CO_2-N_2 mixture with the species individual values taken from NIST database [31].

3 Transport properties

3.1 Calculation of the mixture viscosity

To compute the individual species viscosity, μ_α, the Lucas method [39] has been selected due to its high-p-accuracy capabilities:

$$\mu_\alpha = \frac{Z_2 \, F_P}{\xi_\alpha \, 10^{-7}} \tag{14}$$

where μ_α is in $[Pa \cdot s]$. The calculation of the coefficients Z_2, F_P, ξ_α is shown in the following lines. We define the reduced inverse viscosity as:

$$\xi_\alpha = 0.176 \left(\frac{T_c}{m_\alpha^3 p_{c,\alpha}^4} \right)^{1/6} \tag{15}$$

where ξ is in $[\mu P]^{-1}$, T_c the reduced temperature in kelvins, m is in $[g/mol]$, and $p_{c,\alpha}$ is the reduced pressure in bar. The correction factor for polarity effect, F_P° is

$$
\begin{aligned}
F_P^\circ &= 1 & 0 \le dipm_r < 0.022 \\
F_P^\circ &= 1 \; + 30.55(0.292 - Z_c)^{1.72} & 0.022 \le dipm_r < 0.075 \\
F_P^\circ &= 1 \; + 30.55(0.292 - Z_c)^{1.72} \left| 0.96 + 0.1(T_r - 0.7) \right| & 0.075 \le dipm_r
\end{aligned}
\tag{16}
$$

where Z_c is the critical compressibility factor of the pure species, $dipm_r$ the reduced dipole moment defined as:

$$dipm_r = 52.46 \frac{dipm^2 P_c}{T_c^2} \tag{17}$$

$dipm$ being the dipole moment of the species in $debyes$, p_c in bar, and T_c in Kelvin. The effect of high pressure on viscosity is taken in account using two parameters Z_1 and Z_2 :

$$Z_1 = \left[0.807 T_r^{0.618} - 0.357 \exp(-0.449 T_r) + 0.340 \exp(-4.058 T_r) + 0.018 \right] F_P^\circ \tag{18}$$

If $(1 < T_r < 40)$ and $(0 < P_r \leq 100)$, then

$$Z_2 = Z_1 \left[1 + \frac{aP_r^{1.3088}}{bP_r^f + (1 + cP_r^d)^{-1}} \right] \tag{19}$$

$$\text{with} \quad a = 1.245 \ 10^{-3} \frac{5.1726T_r^{-0.3286}}{T_r}; \qquad d = 1.73\frac{\exp(2.2310T_r^{-7.6351})}{T_r};$$

$$b = a(1.6553T_r - 1.2723); \qquad f = 0.9425\exp(-0.1853T_r^{0.4489});$$

$$c = 0.4489\frac{\exp(3.0578T_r^{-37.7332})}{T_r}$$

If $(T_r \leq 1)$ and $(P_r < 1)$, then

$$Z_2 = 0.600 + 0.760P_r^\alpha + (6.990P_r^\beta - 0.6)(1 - T_r) \tag{20}$$

$$\text{with} \quad \alpha = 3.262 + 14.98P_r^{5.508}; \quad \beta = 1.390 + 5.746P_r$$

for all other cases of T_r and P_r, $Z_1 = Z_2$ has been taken. Therefore, the high pressure correction for polarity is:

$$F_P = \frac{1 + (F_P^\circ - 1)\left(\frac{Z_2}{Z_1}\right)^{-3}}{F_P^\circ} \tag{21}$$

To compute the mixture viscosity, μ, the Wilke method [39] is used providing:

$$\mu = \sum_{\alpha=1}^{N} X_\alpha \omega_\alpha^M \mu_\alpha \tag{22}$$

$$\left(\omega_\alpha^M\right)^{-1} = \sum_{\beta=1}^{N} \phi_{\alpha\beta} X_\beta \tag{23}$$

$$\phi_{\alpha\beta} = \frac{\left[1 + (\mu_\alpha/\mu_\beta)^{1/2} (m_\beta/m_\alpha)^{1/4}\right]^2}{[8(1 + m_\alpha/m_\beta)]^{1/2}} \tag{24}$$

where ω_α^M are weighting factors [39].

3.2 Validation of the viscosity value

As well as done for the density, a comparison between the viscosity value obtained following the Lucas-Wilkie methods and that from the NIST database has been performed. Because

most of the mixture is composed by carbon dioxide and nitrogen, a rough average of the viscosity values from NIST database, weighted on molar fractions of these species has been performed, and the average value was then compared to that computed from Lucas-Wilke methods for the 7-species model. A favorable match of the viscosity values is shown in table 5.

NIST database	Viscosity $[Pa \cdot s]$	Lucas-Wilke method (7-Species)	Error
CO_2	3.3476 x 10^{-5}		
N_2	3.4570 x 10^{-5}		
CO_2-N_2mix	3.3508 x 10^{-5}	3.4546 x 10^{-5}	3.0%

Table 5: Comparison between the mixture viscosity computed following the Lucas-Wilke method and the viscosity of a molar mass-weighted average of a CO_2-N_2 mixture with the species individual values taken from NIST database[31].

3.3   Calculation of the mixture molecular thermal conductivity

The individual species molecular thermal conductivity, λ_α, has been computed for each component of the mixture, using the Stiel-Thodos method [39, 16].

$$\lambda_\alpha = \lambda_\alpha^0 + \frac{FE_p}{\Gamma Z_{c,\alpha}^5} \tag{25}$$

Where $Z_{c,\alpha}$ is the critical compressibility factor of the species α, and the coefficients FE_p, λ_α^0, Γ are computed as follows:

$$
\begin{aligned}
FE_p &= 1.22 \times 10^{-2}[\exp(0.535\rho_r) - 1] & \rho_r &< 0.5 \\
FE_p &= 1.14 \times 10^{-2}[\exp(0.67\rho_r) - 1.069] & 0.5 &< \rho_r < 2.0 \\
FE_p &= 2.60 \times 10^{-3}[\exp(1.155\rho_r) + 2.016] & 2.0 &< \rho_r < 2.8
\end{aligned}
\tag{26}
$$

with ρ_r the reduced density $\rho/\rho_c = V_c/V$.

$$\lambda_\alpha^0 = R_u[3.75 + f_{int}(C_p^\circ/R_u - 2.5)]\frac{\eta^\circ}{m} \tag{27}$$

with m in $[kg/mol]$.

$$f_{int} = \frac{1}{0.7862 - 0.7109\omega + 1.3168\omega^2} \tag{28}$$

Here, ω is the acentric factor. The ideal heat capacities for the individual species, C_p°/R_u, is computed as follows:

$$C_p^\circ/R_u = a_0 + a_1 T + a_2 T^2 + a_3 T^3 + a_4 T^4 \tag{29}$$

with the constants a_0, a_1, a_2, a_3, a_4 given in [37] (Appendix A, Section C).

$$\eta^\circ = \frac{Z_1}{\xi \ 10^{-7}} \tag{30}$$

where equations 18 and 15 are used for Z_1 and ξ computations. The reduced, inverse thermal conductivity, Γ,

$$\Gamma = 210\left(\frac{T_c m^3}{P_c^4}\right)^{1/6} \tag{31}$$

is in $[W/(m\cdot K)]^{-1}$, T_c is in kelvin, m in g/mol, and p_c in bars. Therefore, the mixture molecular thermal conductivity has been computed following the Wassiljewa-Mason-Saxena method [37].

$$\lambda_{mol} = \sum_{\alpha=1}^{N} X_\alpha \omega_\alpha^Q \lambda_\alpha \tag{32}$$

where according to the assumption made by Reid et al. [39],

$$\omega_\alpha^Q = \omega_\alpha^M. \tag{33}$$

The value of λ_{mol} computed following the methods shown above was then compared to a value obtained from NIST database, exactly as done for density and viscosity (refer to tables 4, 5). A comparison of the thermal conductivity values is shown in table 6.

NIST database	Thermal Conductivity $[W/(m \cdot K)]$	Wassiljewa-Mason-Saxena (7 species)	Error
CO_2	0.05388		
N_2	0.05313		
CO_2-N_2mix	0.05385	0.05856	8.0%

Table 6: Comparison between the mixture molecular thermal conductivity computed following the Wassiljewa-Mason-Saxena method and the molecular thermal conductivity of a molar mass-weighted average of a CO_2-N_2 mixture with the species individual values taken from NIST database[31].

3.4   Calculation of the mixture molecular Prandtl number

The Prandtl number is a dimensionless number which characterizes the thermal behavior of the fluid, comparing momentum diffusivity to molecular thermal diffusivity. It is defined as follows:

$$\text{Pr} = \frac{C_p \mu}{\lambda} \tag{34}$$

where μ is the viscosity $[Pa\,s]$, C_p the specific isobaric heat capacity $[J/(kg\,K)]$, λ is the thermal conductivity $[W/(m\,K)]$. (We distinguish between the molecular thermal conductivity λ_{mol}, and an effective thermal conductivity λ_{eff}, which lead to obtain the molecular Prandtl number and the effective Prandtl number respectively. The difference between molecular and effective properties physically resides in turbulence [27]). Another quantity required to compute the Prandtl number is the specific heat capacity, C_p. Since the computation of C_p involves calculation of derivatives of the EOS, leading to error accumulation, and since the considered mixture is composed mostly of carbon dioxide and nitrogen, a molar fraction-weighted average between the carbon dioxide specific heat, $C_p^{CO_2}$, and the nitrogen specific heat, $C_p^{N_2}$, has been used to estimate the mixture molecular Prandtl number, which is therefore computed using equation 34, with the mixture viscosity and the mixture molecular thermal conductivity computed following respectively the Lucas-Wilke and Wassiljewa-Mason-Saxena methods. A comparison with NIST data bank has been performed for Pr, as shown in table 7.

Pr (7 species, Lucas-Wilke method/Wassiljewa et al.[37])	0.6715
Pr (2 species, data from NIST database)	0.7350
Error	8.6%

Table 7: Comparison between the mixture molecular Prandtl number computed following the Lucas-Wilke and the Wassiljewa-Mason-Saxena methods and the molecular Prandtl number of a molar mass-weighted average of a CO_2-N_2 mixture with the species individual values of viscosity, thermal conductivity, and specific heat capacity taken from NIST database[31].

4 Dynamic characteristics: calculation of the Reynolds number

The Reynolds number,

$$\mathrm{Re} = \frac{\rho V L}{\mu} \tag{35}$$

which expresses the ratio between the inertial and the viscous forces in a flow, has been estimated aiming to a characterization of the dynamic of the flow at the Venus surface. Whenever the Reynolds number is small, the viscous forces are strong enough to dampen the flow fluctuations, and the flow assumes laminar characteristics. On the contrary, if the Reynolds number is large enough, then the viscous forces are no longer able to dampen the flow fluctuations, which following a series of hydrodynamic instabilities finally lead to turbulent transition. A characteristic length scale and a characteristic velocity are required to compute this dimensionless number. To this purpose, an investigation on these values has been conducted. The winds near the surface of Venus have a much smaller speed than those in the upper atmosphere, where the super rotation phenomenon occurs; direct and indirect measurements showed that an average speed is 0.3 to 1.0 m/s [3][29]. Concerning the characteristic length scale, it must be related to the phenomenon to be observed. Visible images of surface observations show stones and boulders of about 50 cm, as shown in figure 2(a). Radar images of surface from orbit show surface structural elements with a repeat distance of approximately 5 km, as shown in figure 2(b). Some aspects are stochastic, others are regular. For simulations of the atmosphere at 50 km altitude, the interest is in the macrostructure of the surface, so that perhaps 50 m could be chosen as length scale as a good starting point.

Considering a flow velocity, V, of 1 m/s and a characteristic length scale, L, of 50 m, the Reynolds number computed with the PR-EOS density and Lucas-Wilke method viscosity is shown in table 8, and the obtained value is compared to that calculated using the NIST database. The order of magnitude of the Reynolds number suggests a highly-turbulent flow

Reynolds number (7-species, PR-EOS/Lucas-Wilke method)	93783992
Reynolds number (2-species, data from NIST database)	96986657
Error	3.3%

Table 8: Comparison between the Reynolds number computed by resolution of the PR-EOS and following the Lucas-Wilke method and the Reynolds number for a molar mass-weighted average of a CO_2-N_2 mixture with the species individual values of density and viscosity taken from NIST database[31]. The characteristic length scale and velocity scale used to compute the Reynolds number are the same for both methods.

regime for the layer closest to the surface. The vertical distribution of the Reynolds number will be considered in Sec. 5.
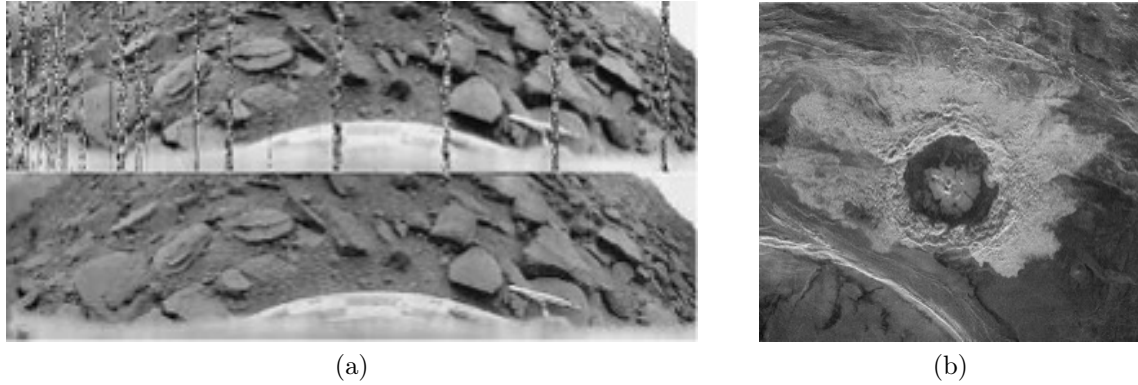

(a)   (b)

Figure 2: (a) Venus surface from Venera lander showing rocks of about 50 cm. (b) Venus surface from Magellan orbiter showing 5 km features.

5 Distribution of the mixture properties and the dynamic characteristics with altitude

After the calculation of the mixture properties and the dynamic characteristics for the reference mixture at ground pressure and temperature conditions, an extension to other altitudes has beed done to investigate the distribution of these quantities in the first 65 km of the planet's atmosphere. Data about the distribution of the temperature and pressure values with altitude are those from Venera 8-12 and Pioneer Venus missions [25], and are shown in figure 3; these compare favorably with data computed from models [40, 13, 7]. Therefore, the thermodynamic and transport properties of the 7-species mixture are computed for each altitude with a step of 5 km, following the same methodology used in the previous sections. In figure 4 is shown the distribution with altitude of the density, viscosity, molecular thermal conductivity and molecular Prandtl number for the 7-species mixture. In order to compute the distribution of the Reynolds number with altitude, a mean profile of the zonal (east-to-west) wind on Venus as measured by tracking the Pioneer Venus entry probes has been taken into account [6] (refer to figure 5 (a)). The resulting Reynolds number for each altitude, computed by using eq. 35 and a characteristic length scale of 50 m is shown in figure 5 (b). As expected, the Reynolds number values are linearly sensitive to the chosen length scale; for that reason different values of Re are show in table 9 for different choices of the length scale.
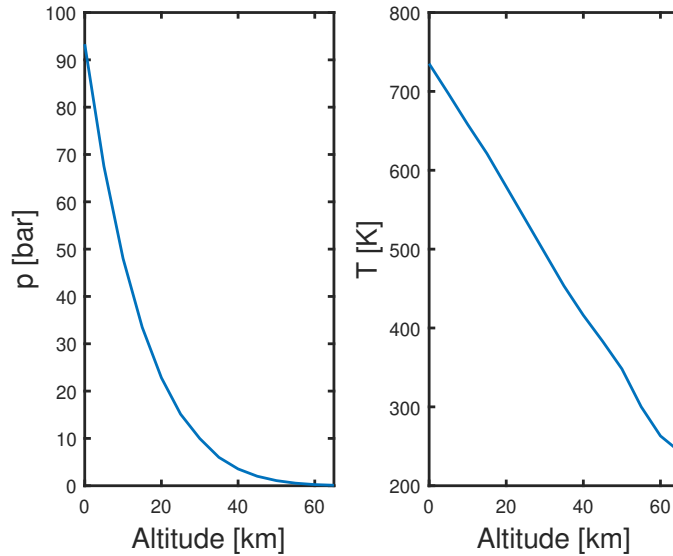

Figure 3: Vertical distribution of the pressure and temperature values in the Venus lower atmosphere [25, 7].

As already mentioned, the Reynolds number value depends on which length scale the phenomenon is observed; for instance, values of the Reynolds number corresponding to a length scale in the meter range would be of interest for aerothermodynamics studies on space probes such as landers and rovers, or for entry problems. As can be observed in figure 5 (b) and in table 9, the high Reynolds number at these altitudes suggests a fully-turbulent regime in the entire lower atmosphere of Venus. An estimate of the vertical distribution of the Mach number is also performed, considering the same velocity profiles used for the Reynolds number computation, and the speed of sound of carbon dioxide taken from the NIST database using the temperature and pressure values correspondent to each altitude. The values obtained for the speed of sound are perfectly in accord with those computed in the DNS realizations (section 7), showing the small influence of all minor species on the speed of sound value. Moreover, the small error on the speed of sound computation is very small compared to the variability and the measurements errors of the velocity profiles, leading to reasonably accurate magnitude of the Mach number. The vertical distribution of the Mach number is depicted in figure 6, where is it possible to observe a trend similar to that of the velocity vertical distribution.
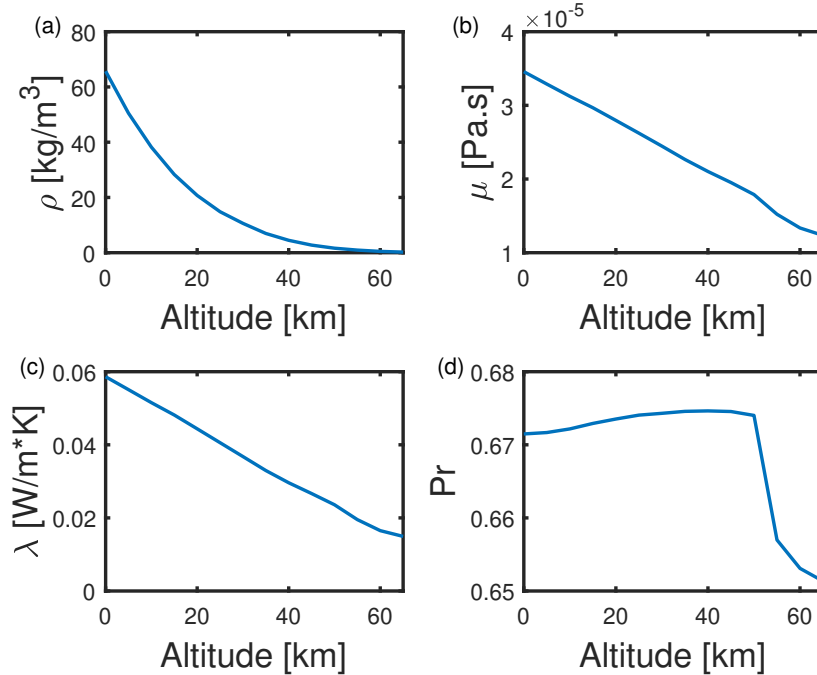

Figure 4: Vertical distribution of the density (a), viscosity (b), molecular thermal conductivity (c) and molecular Prandtl number (d) values in the Venus lower atmosphere.

Altitude $[km]$	$L = 50\,m$	$L = 5\,m$	$L = 0.5\,m$
0	$9.3783\ 10^7$	$9.3783\ 10^6$	$9.3783\ 10^5$
5	$7.6751\ 10^7$	$7.6751\ 10^6$	$7.6751\ 10^5$
10	$1.8351\ 10^8$	$1.8351\ 10^7$	$1.8351\ 10^6$
15	$4.7688\ 10^8$	$4.7688\ 10^7$	$4.7688\ 10^6$
20	$7.4157\ 10^8$	$7.4157\ 10^7$	$7.4157\ 10^6$
25	$7.9183\ 10^8$	$7.9183\ 10^7$	$7.9183\ 10^6$
30	$6.2935\ 10^8$	$6.2935\ 10^7$	$6.2935\ 10^6$
35	$4.6104\ 10^8$	$4.6104\ 10^7$	$4.6104\ 10^6$
40	$4.0505\ 10^8$	$4.0505\ 10^7$	$4.0505\ 10^6$
45	$3.1665\ 10^8$	$3.1665\ 10^7$	$3.1665\ 10^6$
50	$2.5005\ 10^8$	$2.5005\ 10^7$	$2.5005\ 10^6$
55	$1.8226\ 10^8$	$1.8226\ 10^7$	$1.8226\ 10^6$
60	$1.1028\ 10^8$	$1.1028\ 10^7$	$1.1028\ 10^6$
65	$8.1918\ 10^7$	$8.1918\ 10^6$	$8.1918\ 10^5$

Table 9: Reynolds number vertical distribution, for different choices of the characteristic length scale L.
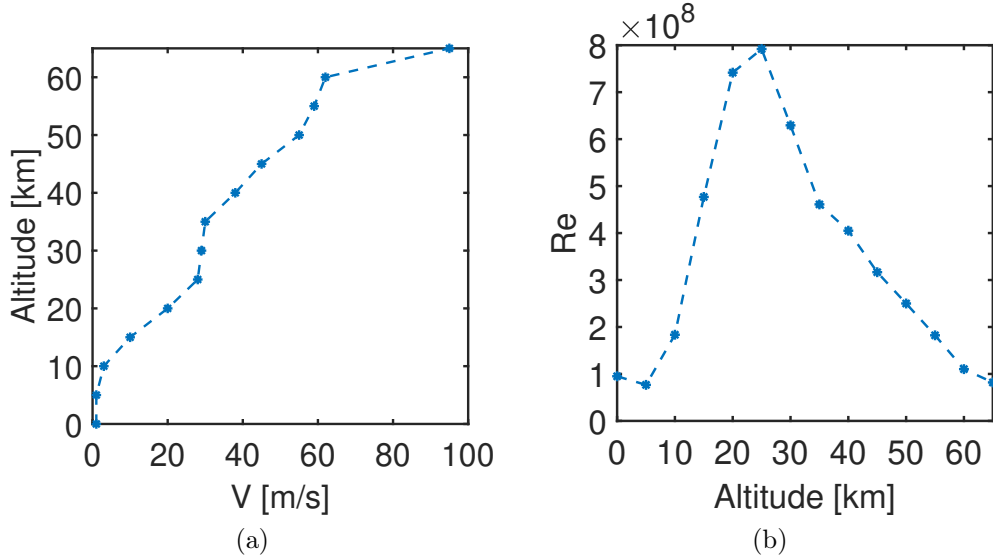
Figure 5: (a)Velocity distribution with altitude in the Venus lower atmosphere. (b) Vertical distribution of the Reynolds number in the Venus lower atmosphere.

Aiming to study the macrostructure of a layer of the Venus atmosphere, Large Eddy Simulations (LES) could be used to obtain solutions at high Reynolds number. These LES are complex, time consuming simulations and requiring substantial modelling. On the other hand, Direct Numerical Simulations (DNS) are unfeasible at such large Reynolds number values because of the extremely high computational cost that would be required. DNS at lower Reynolds number can be envisaged to study mixing properties of the flow that could also be observed at higher Reynolds number; this discussion will be addressed in section 7.

Figure 6: Vertical distribution of the Mach number in the Venus lower atmosphere.

6 Thermodynamic regime

A thermodynamic stability analysis of the Venus lower atmosphere was conducted in order to clarify its thermodynamic regime and to investigate the possibility of 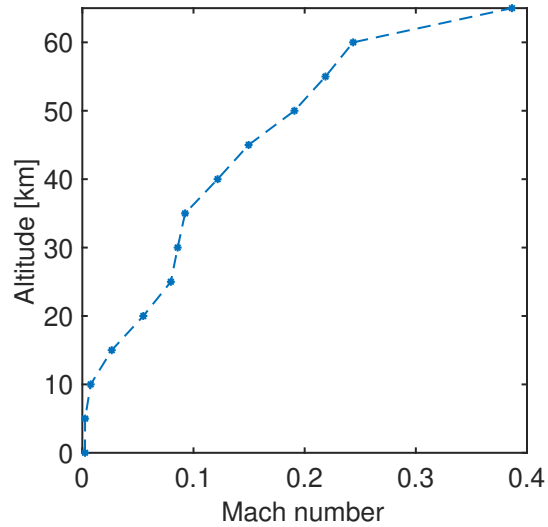having unsteady phenomena such as phase transition, since these would be allowed to happen only under certain thermodynamic conditions. With this purpose, regions of stability and instability are determined in the thermodynamic phase diagram of the mixture, on which the conditions of pressure and temperature typical of Venus are shown.

6.1 Thermodynamic stability

The thermodynamic state of a system can be represented in a (p, T, v)-phase diagram (see fig. 7), where it is possible to identify two important loci, so called "the binodal" and "the spinodal", the projections of which onto the (p, v) plane are shown in figure 8. The binodal, or coexistence curve, limits the equilibrium region from the metastable and unstable ones. Under the binodal curve, another significant curve, i.e. the spinodal, represents the stability limit of the thermodynamic system, so that if the thermodynamic state of the system resides under the spinodal locus, non-equilibrium phenomena will be present, and the system will be affected by unsteadiness. On the (p, v) plane (fig. 8), two regions between the coexistence and the spinodal curves identify two metastable phases encountered by a fluid transitioning from a stable to an unstable thermodynamic state, leading to a metastable-vapour nucleation regime on the vapor-side, and to a liquid-metastable bubble regime on the liquid side. When a system is in its thermodynamic equilibrium, i.e. above the coexistence curve, the thermodynamic information alone is sufficient to completely describe the system. On the contrary, time-dependent conservation equations must be solved in addition to the thermodynamic information in order to describe an unstable system, such as an unsteady evaporating spray.

Several scientific and engineering applications deal with unsteady multi-phase flows, for example nuclear reactors cooling systems or injection systems in combustion chambers of automotive or aerospace engines. In order to improve the performances of those systems, accurate modelling of such flows requires to distinguish liquid regions from vapour ones and predict phase changes. To such purpose, in Computational Fluid Dynamics (CFD) the thermodynamic stability of fluids must be checked in each point of the discretized computational domain. In addition, real-gas EOS alone is not sufficient to describe the state of the system, since multiple solutions for the molar volume v can be present at specified (p, T). For instance, the cubic Peng-Robinson EOS can have two non-physical imaginary roots for v and one real root, which is the physical one and corresponds to a single-phase regime. However, three real roots may also be present: the smallest root, v_l, associated to the liquid phase,

the larger root, v_v, associated to the vapour phase, and the middle root is not considered because it is located in the unstable regime. It is also possible to have two coincident real solutions, and then the system is at a critical condition. The lack of uniqueness of the solution for the cubic EOS leads to the necessity of the resolution of the Navier-Stokes (NS) conservation equations [10]. Indeed, only one of the eventually multiple roots of the EOS will match the NS conservation equations, revealing whether the system is in liquid phase rather than in vapour phase at any point of the domain. In case of multi-species mixtures, the species partial-density conservation equations must be solved in addition to the NS and EOS equations, in order to determine the chemical composition of the mixture in each point of the flow; accurate models for mass-diffusion have been proposed by Harstad & Bellan [18, 17]. The spinodal locus provides a global knowledge about the instability of a mixture, showing its thermodynamic behavior when varying pressure, temperature and composition, and is therefore characterized by the condition in which the macroscopic system is unstable. Further information on stability criteria and spinodal computation can be found in chap. 7 of [44]. The method for the spinodal locus computation for mixtures is that of Castiglioni & Bellan (2018) [8][9], and is described in appendix A.
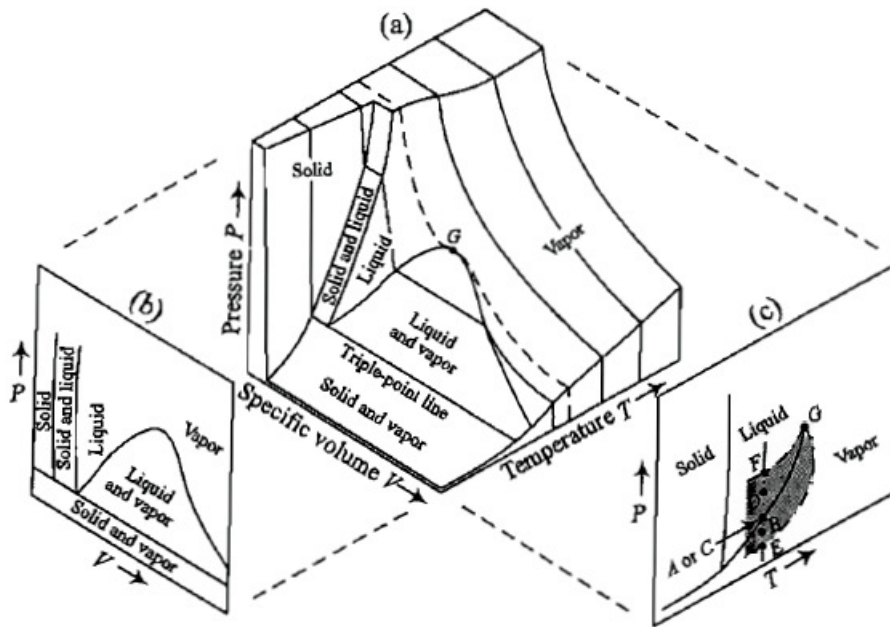

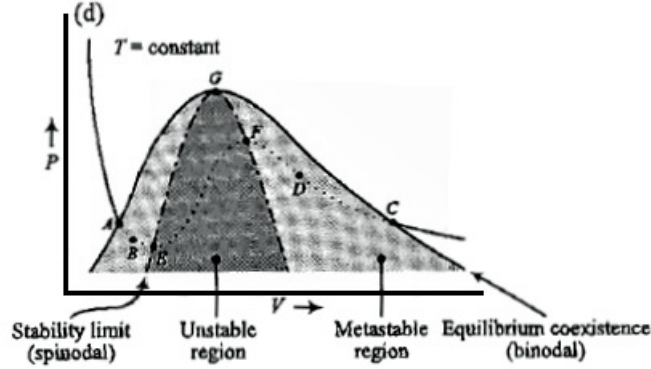
Figure 7: (p, T, v) Phase-diagram.

Figure 8: Binodal and spinodal loci onto the (p, v) plane.

6.2 Results of the thermodynamic regime analysis

Thermodynamic maps for the Venus lower atmosphere mixture have been computed, following the same methodology adopted in [8], and using the same code, already validated for the spinodal computation. A stability analysis for a variety of mixtures was conducted in order to highlight the thermodynamic characteristics of the Venus lower atmosphere and its sensitivity to the variation of the species molar fractions. The mixtures used for computations are selected from data resulting from several missions on Venus [22], and are listed in table 10.

	1 species	2 species	5 species	7 species	11 species
χ_{CO_2}	1	0.96499	0.96482	0.964816395	0.964693
χ_{N_2}	-	0.03501	0.03500	0.03500	0.03500
χ_{SO_2}	-	-	0.00015	0.00015	0.00015
χ_{H_2O}	-	-	3×10^{-5}	3×10^{-5}	3×10^{-5}
χ_{H_2S}	-	-	3×10^{-6}	3×10^{-6}	3×10^{-6}
χ_{HCl}	-	-	-	6×10^{-7}	6×10^{-7}
χ_{HF}	-	-	-	5×10^{-9}	-
χ_{Ar}	-	-	-	-	7×10^{-5}
χ_{CO}	-	-	-	-	3×10^{-5}
χ_{He}	-	-	-	-	1.2×10^{-5}
χ_{Ne}	-	-	-	-	7×10^{-6}
χ_{OCS}	-	-	-	-	4.4×10^{-6}

Table 10: Set of mixtures used for the thermodynamic regime computations for the Venus lower atmosphere. Molar fractions of the relative species are shown. Data from [22].

Spinodal loci are computed for the mixtures listed in table 10 and represented in figure 9. Although in a small amount, it is possible to observe a remarkable influence of the nitrogen in changing the values and the shape of the spinodal locus, i.e. the thermodynamic stability properties of the mixture; whereas the presence of the minor species seems to be negligible. Projections of the spinodal loci onto the (p, T) and (p, v) planes are also shown in figures 10 (a) and 11 (a). The thermodynamic regime of the lower Venus atmosphere is then located on the same plane and compared to the stability limits, i.e. the spinodal loci, computed for the mixtures listed in table 10. A range of temperature between 350K and 750K, and a range of pressure between 1 bar and 92 bars is shown in figure 10 (b), where it is possible to observe that the Venus lower atmosphere regime is always above the critical temperature of the mixture (since the critical temperature is on the spinodal), with supercritical conditions present in the first few kilometers above the surface. The distribution of the temperature and pressure values with altitude are those from probes [7], and the molar volume at each altitude is computed from PR-EOS, considering the 7-species mixture. The values of pressure and molar volume resulting from computations for different altitudes with a step of 5 km are shown in figure 11 (b), where it is clearly shown that the mixture thermodynamic regime is always above the spinodal locus, no matter the altitude considered. Therefore, in figure 11 (b) is shown that for the assumed composition [22], unstable regime is not reached, and neither is metastable-vapour nucleation regime considering the large distance between the spinodal locus and the points of interest for the Venus lower atmosphere onto the (p, v) phase diagram. Thus, the Venus lower atmosphere temperature is always above the maximum temperature of the spinodal locus of the mixture, and therefore, only a stable regime thermodynamically occurs in the Venus lower atmosphere, meaning that no rain can happen in the lower atmosphere of Venus. This result should be taken in a guarded manner, since the mixture considered for this study is of averaged compositions of the major species measured by probes in the lowest part of the atmosphere, as accurate data including composition gradients of the species are not available. Sulfuric acid clouds are known to reside in the higher part of the atmosphere, starting from about 50 km up, with a sulfuric acid haze in the part immediately below. The average mixture used in this study does not represent such high altitudes, since sulfuric acid is not considered as species, and only results for the lowest altitudes can be considered consistent.
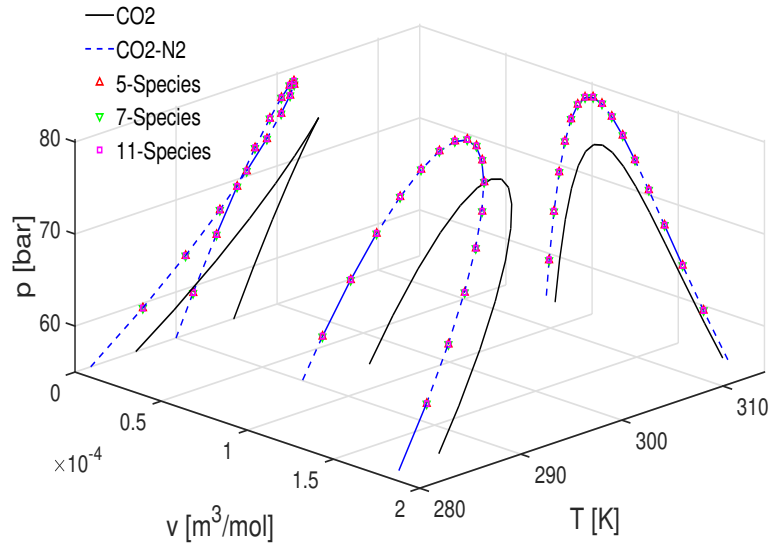
Figure 9: Spinodal loci for several mixtures (table 10) at constant composition, and its projections onto the (p, T) and (p, v) planes.
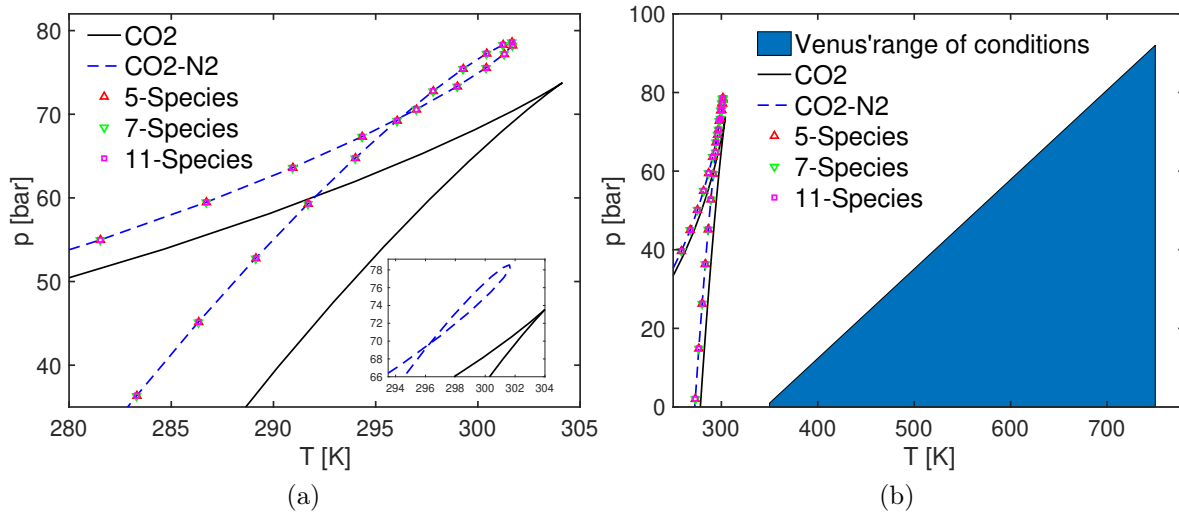
Figure 10: (a) Comparison between spinodal loci for different mixtures , onto the (p,T) plane. (b) The Venus lower atmosphere regime is highlighted on the thermodynamic phase diagram, where spinodal loci of Venus-like lower atmosphere mixtures are shown.
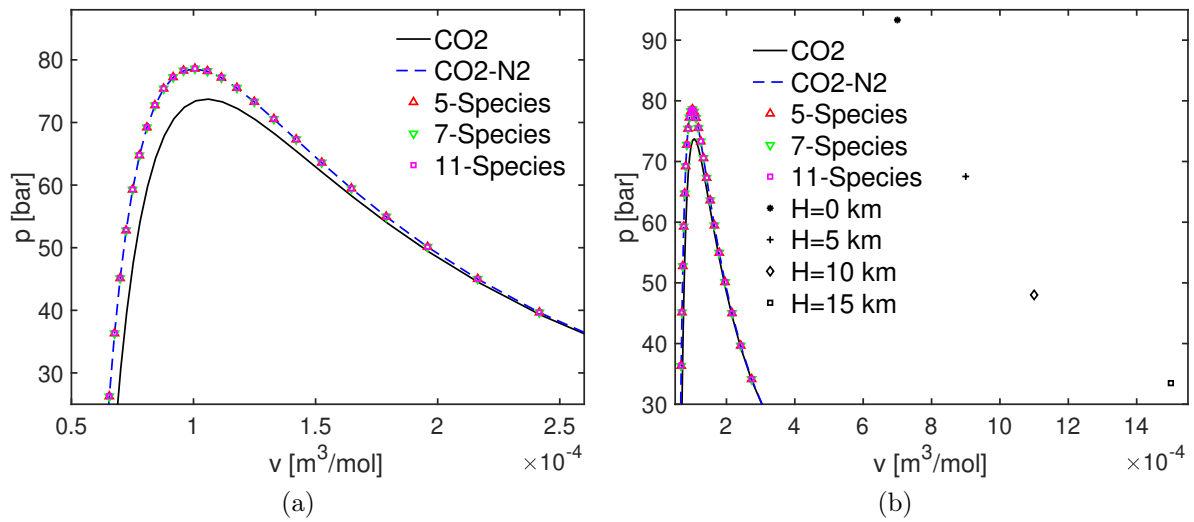
Figure 11: (a) Comparison between spinodal loci for different mixtures, onto the (p,v) plane. (b) Pressure and molar volume conditions in the Venus lower atmosphere are shown for various heights, H, on the thermodynamic phase diagram, where spinodal loci of Venus-like lower atmosphere mixtures are shown.

7 Direct Numerical Simulation

Computational Fluid Dynamics (CFD) is largely used to predict the behavior of a fluid in a variety of applications. Several types of simulations can be considered to study a particular case, starting from the low computational cost Reynolds Averaged Navier-Stokes (RANS) simulations, widely used in industry to get information about the average characteristics of a flow. In RANS simulations only the mean flow is solved, while all the turbulent structures are modelled with consequent loss of information according to the models accuracy. In Large Eddy Simulation (LES) the large scales are resolved, whereas the smallest scales, so called Subgrid-Scales (SGS), are modelled, leading to providing more than mean flow resolution when compared to RANS simulations. Only in Direct Numerical Simulation (DNS) all the scales overwhelmingly responsible for dissipation are resolved, allowing a fundamental investigation of the flow characteristics. Since all length scales must be solved in DNS, the Reynolds number become a limiting factor; indeed, since the length scales extend over a wider range while increasing Reynolds number, it follows that the larger the Reynolds number is (i.e. increasing turbulence) the finer the computational domain mesh must be in order to capture the entirety of the structures, from the largest to the smallest ones. In multispecies flows with Prandtl number or Schmidt number grater than unity, the limiting factors become the resolution of the thermal and species-diffusion length scales, leading to even finer grid requirements. Since the complete resolution of the governing equations is carried out, DNS represent a virtual experiment, reproducing the physical aspects in the most accurate way, enabling to study some poorly understood phenomena, or even discover new ones.

CFD simulations can be performed to attain a better understanding of the Venus atmosphere. In this context, it is clear that DNS is unfeasible at the characteristic Reynolds number on the planet, which is $O(10^9)$, as computed in sec. 4. Considering that the computational cost of a DNS grows as Re^3, it is evident that simulating flows at Reynolds numbers of millions is unfeasible. Simulations of planetary atmospheres at physical Reynolds numbers are simply not feasible using the DNS method, since the Reynolds numbers are typically very large, and the computational costs are unaffordable [45]. The situation is different for LES, where higher values of the Reynolds number can be addressed. Regardless of the type of simulation, the size of the computational domain should be chosen in function of the phenomena to be observed; if interested in studying the macrostructure of a portion of the atmosphere (i.e. large computational domains), gravity and eventually Coriolis terms should be included in the momentum conservation equation, in order to account for the formation of the hydrostatic density gradient and therefore to predict the basic state of the atmosphere, i. e. the vertical distribution of the pressure, temperature, density and chemical composition of the atmosphere in equilibrium. A wall condition should also be introduced to simulate the interaction with the Venus surface.

When studying atmospheric circulation, whether the Coriolis force plays a role in the problem will depend on the Rossby number, $Ro = U/Lf$, where U and L are, respectively, the characteristic velocity and the length scales of the phenomenon and $f = 2\Omega \sin(\phi)$ is the Coriolis frequency, Ω is the angular frequency of planetary rotation and ϕ is the latitude. When the Rossby number is large, then the Coriolis force is negligible, and the balance is between pressure and centrifugal forces, so-called cyclostrophic balance; on the contrary, when the Rossby number is small, the centrifugal force is negligible and the balance is between Coriolis and pressure forces, so-called geostrophic balance [21]. Since Venus has an extremely small sideral rotational period, revolving on itself 243 times slower than the Earth, the resulting Rossby number is high, meaning that the inertial force overcomes the Coriolis force. For that reason the circulation in Venus's troposphere follows the cyclostrophic flow [41], where the Coriolis force is neglected.

Smaller computational domains are suitable if interested to study non-equilibrium and perturbation phenomena (e.g. mixing) of the basic state at certain altitudes. In this context, whether the gravity term is important or not is determined by the Froude number, $Fr = U/\sqrt{gL}$, where g is the gravity acceleration of the planet ($8.87\,[m/s^2]$ on Venus), whereas U and L are, respectively, the characteristic velocity and the length scales of the phenomenon. If the Froude number is very large, then the gravity effect on the flow is negligible when compared to the inertial term; on the contrary, if the Froude number is small, then gravity plays a significant role and should be included in the models. A discussion on the choice of the domain size, justified by the calculation of the Froude number for different scenarios will be addressed in sec. 7.3.

Whatever the choice of the computational domain size, accurate LES of the atmosphere require accurate SGS models to be implemented, and this is not straightforward when considering supercritical multispecies mixtures, which is the case of the Venus lower atmosphere. In such flows there is a strong coupling between species-mass transfer, thermal-transfer, and momentum transfer, and it is not uncommon for some counterintuitive phenomenon to occur, such as uphill diffusion which is still subject of intense research and its study represents the state-of-art in fluid dynamics research [27, 8]. The nature of these types of phenomena plays at molecular length scales and therefore they cannot be captured by LES, but they can only be observed at resolution of the smallest scales (i.e. DNS). In this context, collecting a DNS database, even if at necessarily low Reynolds number, could be a good starting point to investigate physical phenomena which could persist at higher Reynolds number, and to build Subgrid-Scale (SGS) models to implement accurate LES. DNS is therefore chosen as method of simulation, since it allows to explore details which are undetectable using other computational methods (e.g. LES or RANS) because of the embedded approximate submodels.

The Venus lower atmosphere is thought to be highly stratified [13], therefore it could be

interesting to set up large domain simulations to understand how turbulence plays a role in the mixing of the species compared to the gravity effect which tends to stratify them. On the other hand, small domain computations can simulate perturbations of the basic state of the planetary atmosphere at different altitudes, and highlight, for example, how supercritical conditions play a role in mixing, high-pressure and temperature effects, or the influence of the minor species in the mixing process. This latter approach is the choice for the present study. In this part of the work, we do not aim to simulate a physical case actually present on Venus, but rather conduct a fundamental study which focuses on understanding the influence of some parameters on the mixing of the species present in the Venus lower atmosphere at realistic thermodynamic conditions, relevant for further studies on the planet's atmosphere. We investigate the high-pressure turbulent multi-species mixing at thermodynamic conditions typical of certain altitudes.

7.1 Governing equations

7.1.1 Conservation equations

The typical conservation equations which express the conservation of quantities such as mass, momentum and energy, are called the Navier-Stokes (NS) conservation equations. When dealing with multispecies mixtures, other equations must be solved in addition to the Navier-Stokes equations, and these are the species-mass transport equations, describing the temporal-spatial evolution of the species partial-densities. The conservation equation for mass, momentum, energy and species-transport are those of Masi et al. [27]:

$$\frac{\partial \rho}{\partial t} + \frac{\partial}{\partial x_j} \left[\rho u_j \right] = 0, \tag{36}$$

$$\frac{\partial}{\partial t} \left(\rho u_i \right) + \frac{\partial}{\partial x_j} \left[\rho u_i u_j + p \delta_{ij} - \sigma_{ij} \right] = 0, \tag{37}$$

$$\frac{\partial}{\partial t} \left(\rho e_t \right) + \frac{\partial}{\partial x_j} \left[\left(\rho e_t + p \right) u_j - u_i \sigma_{ij} + q_j \right] = 0, \tag{38}$$

$$\frac{\partial}{\partial t} \left(\rho Y_\alpha \right) + \frac{\partial}{\partial x_j} \left[\rho Y_\alpha \, u_j + J_{\alpha j} \right] = 0, \tag{39}$$

where $\alpha \in [1, N-1]$, t denotes the time, x is a Cartesian coordinate, subscripts i and j refer to the spatial coordinates, u_i is the velocity, $e_t = e + u_i u_i / 2$ is the total energy (i.e. internal energy, e, plus kinetic energy), Y_α is the mass fraction of species α and N is the number of species, σ_{ij} is the Newtonian viscous stress tensor

$$\sigma_{ij} = \mu \left(2 S_{ij} - \frac{2}{3} S_{kk} \delta_{ij} \right), \quad S_{ij} = \frac{1}{2} \left(\frac{\partial u_i}{\partial x_j} + \frac{\partial u_j}{\partial x_i} \right), \tag{40}$$

where μ is the viscosity, S_{ij} is the strain-rate tensor, and $J_{\alpha j}$ and q_j are the j-direction species-α mass flux and heat flux, respectively.

Accurate models for the computation of $\mathbf{J}_\alpha$ and $\mathbf{q}$, derived by Harstad & Bellan [18], are selected to carry out DNS simulations. Before proceeding with a description of those models, we want to highlight their high accuracy.

Mass diffusion in a binary mixture can be described by the well known Fick's diffusion law, however, it is not the same for multi-specie mixtures, where the phenomenology is different from Fick's mass diffusion. For example, a phenomenon which cannot be described by the Fick's diffusion law is the uphill diffusion, experimentally observed by Duncan & Toor [12]. The experiment consists in a tube connecting two bulbs filled with two different binary mixtures, involving three species, kept at equal pressures and temperatures, and observe what happens to the concentration of the species when opening the valve. One tank is initially filled with nitrogen, N2, and carbon dioxide, CO2, whereas the other one is initially filled with N2 and hydrogen, H2, but the initial molar fraction of N2 is different in the two bulbs. When the valve is opened, CO2 and H2 start to diffuse from the bulb where the respective species mass concentration is higher toward the bulb in which the species mass concentration is lower, as can intuitively be thought and described by Fick's diffussion law. However, after a short time during which N2 also diffuses in this manner, N2 diffuses from regions at low mass concentration to ones at higher mass concentrations, accumulating over the time. This counterintuitive phenomenon is called reverse diffusion or uphill diffusion, and cannot be predicted by Fick's law. It is clear that some other physics plays a role in multicomponent mass transfer. This physics is incorporated into Harstad & Bellan models [18], and this implementation in simulations has reproduced the uphill diffusion phenomenon[27, 8], showing high accuracy of the models.

The full matrices of mass-diffusion coefficients and thermal-diffusion factors derived by Harstad & Bellan [18] are used to express the mass and heat fluxes. Instead of using a set of N dependent species equations for eq. 39, a set of $(N-1)$ independent species equations are solved for the species mass fractions. $\mathbf{J}_\alpha$ and $\mathbf{q}$ are expressed as follows:

$$\mathbf{J}_\alpha = -\rho \left[Y_\alpha \left(D_{T,\alpha} \right) \frac{\nabla T}{T} + Y_\alpha \left(D_{p,\alpha} \right) \frac{\nabla p}{p} + \sum_{\beta=1}^{N-1} \left(D'_{\alpha\beta} \frac{m_\alpha}{m_\beta} \right) \nabla Y_\beta \right], \tag{41}$$

$$\mathbf{q} = -\lambda \nabla T + \sum_{\alpha=1}^{N-1} \mathbf{J}_\alpha \left[\left(\frac{h_\alpha}{m_\alpha} - \frac{h_N}{m_N} \right) - R_u T \left(\frac{\bar{\alpha}_{T,\alpha}^b}{m_\alpha} - \frac{\bar{\alpha}_{T,N}^b}{m_N} \right) \right] \tag{42}$$

where

$$D_{T,\alpha} = -\sum_{\beta=1}^{N} \bar{\alpha}_{T,\beta}^{b} \mathbb{D}_{\beta\alpha}, \qquad D_{p,\alpha} = \frac{p}{R_u T} \sum_{\beta=1}^{N} v_\beta \mathbb{D}_{\beta\alpha}, \tag{43}$$

$$D_{\alpha\gamma} = \sum_{\beta=1}^{N} \mathbb{D}_{\alpha\beta} \alpha_{D\beta\gamma}, \tag{44}$$

$$\bar{\alpha}_{T,\alpha}^{b} = \sum_{\beta=1}^{N} X_\beta \alpha_{T,\beta\alpha}^{b}, \tag{45}$$

$$D'_{\alpha\beta} = D_{\alpha\beta} - \left(1 - \frac{m_\beta}{m_N}\right) \left(\sum_{\gamma=1}^{N-1} D_{\alpha\gamma} X_\gamma\right). \tag{46}$$

Here, $X_\alpha = Y_\alpha m/m_\alpha$ represents the species molar fraction; m_α is the species molar mass; m is the mixture molar mass, computed as an average between single species molar masses weighted on its molar fractions $m = \sum_{\gamma=1}^{N} m_\gamma X_\gamma$; $v_\alpha = (\partial v/\partial X_\alpha)_{T,p,X_\beta(\beta\neq\alpha)}$ is the partial molar volume, where the molar volume is $v = 1/n$ and $n = \rho/m$ is the molar density; $h_\alpha = (\partial h/\partial X_\alpha)_{T,p,X_\beta(\beta\neq\alpha)}$ is the partial molar enthalpy, where the molar enthalpy is $h = G - T(\partial G/\partial T)_{p,X}$ with G being the Gibbs energy; R_u is the universal gas constant; $D_{\alpha\gamma}$ are the pairwise mass diffusion coefficients; $\alpha_{T,\alpha\beta}^{b}$ are the binary thermal diffusion factors; and λ is the thermal conductivity. The mass-diffusion factors, $\alpha_{D\alpha\beta}$, are calculated from thermodynamics as

$$\alpha_{D\alpha\beta} \equiv \frac{1}{R_u T} X_\alpha \frac{\partial \mu_\alpha}{\partial X_\beta} = (\delta_{\alpha\beta} - \delta_{\alpha N}) + X_\alpha (R_{\alpha\beta} - R_{\alpha N}) \tag{47}$$

with $1 \leqslant \alpha \leqslant N$, $1 \leqslant \beta \leqslant N-1$, and

$$R_{\alpha\beta} \equiv \frac{\partial \ln \gamma_\alpha}{\partial X_\beta} \tag{48}$$

with $1 \leqslant \alpha \leqslant N$, $1 \leqslant \beta \leqslant N$. Here, μ_α is the chemical potential of species α written in terms of $N-1$ species; $\gamma_\alpha \equiv \varphi_\alpha/\varphi_\alpha^o$ where φ is the fugacity coefficient written in terms of N species and the superscript o denotes the pure ($X_\alpha = 1$) limit. Matrix elements $\mathbb{D}_{\beta\gamma}$ are the solution of the mixing rules equations ([18])

$$\sum_{\beta=1}^{N} \left[\delta_{\alpha\beta} - (1 - \delta_{\alpha\beta}) X_\beta \frac{\bar{\mathcal{D}}_\alpha}{\mathcal{D}_{\alpha\beta}^{b}}\right] \frac{\mathbb{D}_{\beta\gamma}}{X_\beta} = \bar{\mathcal{D}}_\alpha \frac{(\delta_{\alpha\gamma} - Y_\alpha)}{X_\alpha} \tag{49}$$

where

$$\bar{\mathcal{D}}_\alpha = 1/\sum_{\substack{\beta=1 \\ \beta \neq \alpha}}^{N} \left(\frac{X_\beta}{\mathcal{D}_{\alpha\beta}^b} \right). \tag{50}$$

Solutions for $\mathbb{D}_{\beta\gamma}$ may be obtained by an approximate inversion ([14]) as follows:

$$\mathbb{D}_{\beta\gamma} \simeq X_\beta \mathbb{D}_{\beta\gamma}^{(1)}, \tag{51}$$

$$\mathbb{D}_{\alpha\beta}^{(1)} = \frac{(1+Y_\alpha)}{X_\alpha} \mathcal{D}_\alpha^* \delta_{\alpha\beta} + (1-\delta_{\alpha\beta}) \frac{\mathcal{D}_\alpha^* \mathcal{D}_\beta^*}{\mathcal{D}_{\alpha\beta}^b} - \left(\sigma_\alpha \mathcal{D}_\alpha^* + \sigma_\beta \mathcal{D}_\beta^* \right) + \sum_{\gamma=1}^{N} \left(Y_\gamma \sigma_\gamma \mathcal{D}_\gamma^* \right), \tag{52}$$

$$\mathcal{D}_\alpha^* = (1 - Y_\alpha) \bar{\mathcal{D}}_\alpha, \tag{53}$$

$$\sigma_\alpha = \frac{m_\alpha}{m} (1 + Y_\alpha) + \sum_{\substack{\beta=1 \\ \beta \neq \alpha}}^{N} Y_\beta \frac{\mathcal{D}_\beta^*}{\mathcal{D}_{\alpha\beta}^b} \tag{54}$$

where $\mathcal{D}_{\alpha\beta}^b$ is the full approximation binary-diffusion matrix. This method leads to a singularity when the mixture is composed of only one species. In that case equation (50) is no longer used and the diffusion coefficients are evaluated using the binary-diffusion matrix, by setting $\mathcal{D}_\alpha^* = \mathcal{D}_{\alpha N}^b$ where N represents the index associated with the solvent. This method was tested against an exact Gauss inversion and it gave the same results, with an additional gain in computational time. Defining $\mathcal{D}_{\alpha\beta}$ as the first approximation of the binary diffusion matrix and realizing that the deviation of the ratio $\mathcal{D}_{\alpha\beta}^b/\mathcal{D}_{\alpha\beta}$ from unity is comparable to uncertainties in binary diffusion coefficients values ([18]), we assume $\mathcal{D}_{\alpha\beta}^b = \mathcal{D}_{\alpha\beta}$. The computation of $\mathcal{D}_{\alpha\beta}$ and $\alpha_{T,\alpha\beta}^b$ is described below.

7.1.2 Equation of state

The conservation equations (36)-(39) are coupled with the Peng-Robinson (PR) EOS

$$p = \frac{R_u T}{(v_{PR} - b_{mix})} - \frac{a_{mix}}{(v_{PR}^2 + 2b_{mix}v_{PR} - b_{mix}^2)} \tag{55}$$

from which T and p are obtained as an iterative solution which satisfies both values of ρ and of e, as obtained from the conservation equations [33]. Here v_{PR} is the molar PR volume, and $v = v_{PR} + v_s$ where v_s is the volume shift introduced for improving the accuracy of the PR EOS at high p; The v_s computation was described in detail elsewhere [33]. a_{mix} and b_{mix} are functions of T and X_i, and their expression is described in sec. 2.

7.1.3 Mixture viscosity

The mixture physical viscosity, μ_{ph}, is computed following the Wilke method [39],

$$\mu_{ph} = \sum_{\alpha=1}^{N} X_\alpha \omega_\alpha^M \mu_\alpha \tag{56}$$

where the individual species viscosities, μ_α, are computed using the Lucas method [39], which provides high accuracy while treating high pressure fluids. A description of these methods is reported in sec. 3.1. We distinguish between the physical viscosity, μ_{ph}, and a a reference viscosity, μ_R, defined in sec. 7.3, and used to carry out the DNSs.

7.1.4 Mixture thermal conductivity

The physical mixture thermal conductivity, λ_{ph}, is computed using the Wassiljewa-Mason-Saxena method [37].

$$\lambda_{ph} = \sum_{\alpha=1}^{N} X_\alpha \omega_\alpha^Q \lambda_\alpha \tag{57}$$

where the Stiel-Thodos method [39] is used to compute the individual species thermal conductivities, λ_α. Details of these methods can be found in sec. 3.3. We will explain how a scaled thermal conductivity is computed to perform DNSs in sec. 7.3.

7.1.5 Binary mass diffusivities

Matrix elements $\mathcal{D}_{\alpha\gamma}^b$ are the building blocks of $\mathbb{D}_{\alpha\gamma}$ and basically of $D'_{\alpha\gamma}$. To compute $\mathcal{D}_{\alpha\gamma}^b = \mathcal{D}_{\alpha\gamma}$, we adopt the method of [17] which gives (in cgs units)

$$n\mathcal{D}_{\alpha\gamma} = 2.81 \times 10^{-5} \frac{f_{D,\alpha\gamma}(T)}{r_D v_{c,\alpha\gamma}^{2/3}} \left[\left(\frac{1}{m_\alpha} + \frac{1}{m_\gamma} \right) T \right]^{1/2} \tag{58}$$

where $f_{D,\alpha\gamma}(T)$ is generically defined for each matrix element as $f_D(T) \equiv (T_{red})^s$ with $\ln s = \sum_{\zeta=0}^{5} a_\zeta^s (\ln T_{red})^\zeta$ where the a^s vector has elements {-0.84211, -0.32643, -0.10053, 0.07747, 0.0127, -0.00995}, and r_D is a constant $O(1)$ which provides an empirical adjustment for the specifics of the collisional interactions of a selected pair of species. $T_{red,\alpha\gamma} \equiv T/T_{c,\alpha\gamma}$ with $T_{c,\alpha\gamma}$; $v_{c,\alpha\gamma}$ as in sec. 2.

7.1.6 Binary thermal diffusion factors

According to Harstad & Bellan [18]

$$\alpha_{T,\alpha\gamma}^{b} = \zeta_{\alpha\gamma}\frac{(m_\alpha\omega_\gamma^T - m_\gamma\omega_\alpha^T)}{(m_\alpha + m_\gamma)\mathcal{D}_{\alpha\gamma}} \tag{59}$$

$$\omega_\alpha^T = \frac{\omega_\alpha^Q\lambda_\alpha}{R_u n}, \quad \zeta_{\alpha\gamma} = \frac{6}{5}C_{\alpha\gamma}^* - 1 \tag{60}$$

where ω_α^Q is computed from equations (23) and (33), and $C_{\alpha\gamma}^*$ is given by Hirsfelder et al. [20] and is function of a normalized temperature including the characteristic molecular interaction potential [18].

7.2 Numerical method

The differential equations described in sec. 7.1.1 combined with the equation of state 55 were numerically solved using a fourth-order explicit Runge-Kutta time integration and a sixth-order compact scheme spatial discretization [26]. Time stability is achieved by filtering spurious information from the conservative variables using the eighth-order compact filter described in [15]. The filter coefficient is sufficiently large to ensure that the filter only acts on the shortest wavelengths resolved on the grid, without affecting the physical content of the data. The code was parallelized using three-dimensional domain decomposition and message passing. The tridiagonal solvers for the compact derivative scheme and the compact filter were efficiently parallelized using the method of Muller & Scheerer [30]. The grid spacing is uniform in the three directions x_1, x_2, x_3, i. e. $\Delta x = \Delta y = \Delta z$, whose choice ensuring the resolution of the smaller scales relevant to dissipation. Typically, the choice of the grid spacing and its scaling with the Reynolds number can be predicted with consideration on the integral and the Kolmogorov length scales, leading to the grid spacing decreasing as a power law of the Reynolds number. This prediction is not straightforward while dealing with turbulent transitional flows with involved diffusion phenomena and high pressure conditions. Therefore, several tests have been performed increasing the grid refinement, and the finer mesh was kept for all realizations since they were performed at the same Reynolds number, allowing fine spatially-temporal representation of the smallest scales, even if the grid is not the optimal one for each simulation. The grid spacing used for the DNS realizations is listed in table 14. The domain length, L_i, in each direction is the same for all simulations. Given the choice on L_1 and the grid points $N_1 \times N_2 \times N_3$, the grid spacing is $\Delta x = \Delta y = \Delta z = L_1/N_1$, and $L_2 = \Delta y \times N_2$, $L_3 = \Delta z \times N_3$ are determined consequently.

7.3   Configuration, boundary conditions and initial conditions

A temporal mixing layer has been chosen as configuration for this case of study (see figure 12), with periodic boundary conditions in the streamwise (x_1) and spanwise (x_3) directions and non-reflecting boundary conditions in the cross-stream (x_2) direction. The domain lengths are $L_1 = 0.2\,m$, $L_2 = 0.22\,m$, $L_3 = 0.12\,m$ for all the simulations. The domain size in the cross-stream direction (L_2) is sufficiently wide to avoid boundary interference with the mixing layer at any time of the simulation, and large enough to have a high Froude number regime and then a negligible gravity term, $\rho g/Fr^2$, in the momentum equation, as can be seen from table 11, where the order of magnitude of the Froude number is shown as function of the computational domain length in the cross-stream direction, L_2, and the consequent characteristic length scale for the mixing layer, i.e. the initial vorticity thickness, $\delta_{\omega,0}$. The Froude number was computed as $Fr = \langle U \rangle / \sqrt{g\delta_{\omega,0}}$, where $\langle U \rangle$ represents the average among the characteristic velocities for the DNS simulations.
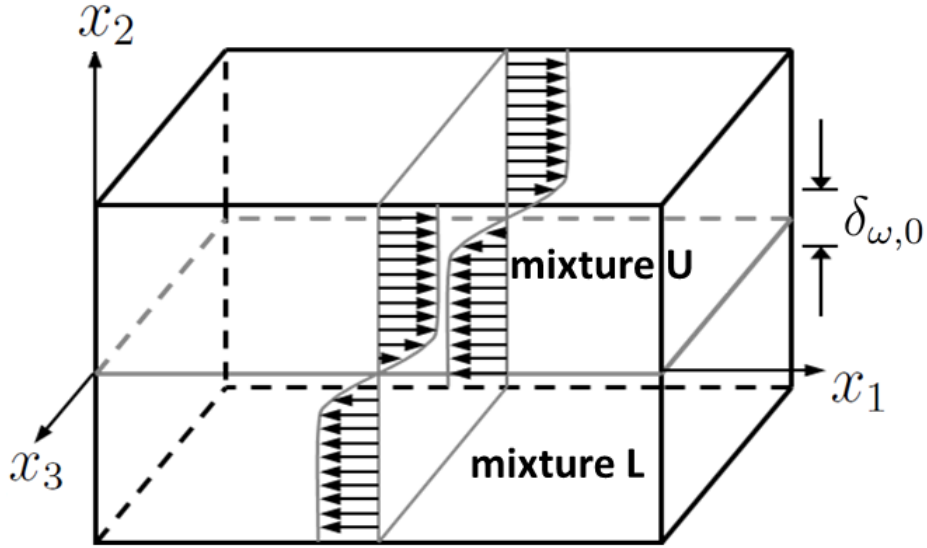

Figure 12: Configuration of the temporal mixing layer. The initial conditions for upper stream and lower stream for the DNS realizations are summarized in tables 12 and 13.

$L_2\ [m]$	$\delta_{\omega,0}\ [m]$	Froude number
0.22	0.00686	1378
1.11	0.0343	616
11.1	0.343	195
111	3.43	62
1110	34.3	20
11100	343	6

Table 11: Magnitude of the Froude number as function of the computational domain size in the cross-stream direction, L_2, and the initial vorticity thickness, $\delta_{\omega,0}$.

To hasten the flow transition to turbulence characteristics, an analytical perturbation is used in the streamwise and spanwise directions. The streamwise (L_1) and spanwise (L_3) domain lengths are such that to accommodate four vortices associated with the wavelengths λ_1 and λ_3 of perturbation: $\lambda_1/\delta_{\omega,0} = 7.29$ and $\lambda_3 = 0.6\,\lambda_1$ as in [28]. The amplitudes of the initial perturbations are $F_{3D} = 0.08$ and $F_{2D} = 0.05$. The initial mean flow derivation and the initial analytical perturbation are those of Masi et al. [27], the details of which are addressed in appendix B. In table 12 are listed the initial pressure and temperature conditions for the simulations; these are selected to simulate the mixing process at various altitudes on the planet, and they are the same for upper and lower streams for each realization. As already stated, the extremely large Reynolds number of the Venus atmosphere is not conducive to DNS, due to the computational cost restrictions. Therefore, all the simulations are necessarily performed at smaller values of the Reynolds number:

$$Re_0 \equiv \frac{0.5(\rho_U + \rho_L)\Delta U_0 \delta_{\omega,0}}{\mu_R} \qquad \text{with} \qquad \delta_{\omega,0} = \frac{\Delta U_0}{\left.\frac{\partial \langle U_0 \rangle}{\partial x_2}\right|_{\max}} \tag{61}$$

where $\langle\rangle$ symbolizes averages over homogeneous (x_1, x_3) planes. Subscripts U and L denote upper stream and lower stream respectively. Here, $\delta_{\omega,0}$ is the initial vorticity thickness, ρ_U and ρ_L are mixture initial densities, $\Delta U_0 = U_U - U_L$ is the initial free-stream velocity difference across the layer and μ_R is a reference viscosity. A physical initial mixture viscosity $\mu_{ph,0}$ is computed based on the physical initial species viscosities, then the reference value μ_R is obtained from the chosen value of Re_0, and finally a factor $\mathcal{F} \equiv \mu_R/\mu_{ph,0}$ is defined. All transport properties computed during the simulation are then scaled by $\mathcal{F}$, a procedure which allows the computation of accurate dimensionless numbers, which according to Batchelor (1999) [4] define the character of the solution. The value of $\mathcal{F}$ was computed at the initial time, for the initial constant p_0 and T_0, using a mixture composed of 2 or 7 species, each species being averaged over the entire domain. In this manner, a unique $\mathcal{F}$ value is employed

in the computational domain. The value of ΔU_0 is calculated from a specified value of the convective Mach number, M_c, through the expressions:

$$U_U = 2M_c a_U \left[1 + \left(\frac{a_U}{a_L}\right)\sqrt{\frac{\rho_U}{\rho_L}}\right]^{-1}, \qquad U_L = -\sqrt{\frac{\rho_U}{\rho_L}}U_U, \tag{62}$$

where a is the speed of sound computed from the EOS. The convective Mach number is set to $M_c = 0.4$ for all simulations.

A substantial DNS database is generated, allowing the analysis of the mixing process under several different conditions of pressure, temperature, number of the species considered and initial chemical composition for upper and lower streams typical of the Venus atmosphere, which is the aim of this part of the work. Each DNS realization is identified by an alphanumeric label of the type NsHx, where N is the number of the species considered (2 or 7), s is the species stratification type (i.e. high-stratification 'hs' or low-stratification 'ls'), and H is the approximate altitude on Venus. The number of species considered is 2 or 7, and the initial molar and mass fractions for the upper stream and the lower streams are listed in table 13. This approach allows to understand whether different assumptions on the chemical composition of the mixture produce variations in the mixing process and, in that case, the sensitivity of such variations to these assumptions.

Case	$H\,[km]$	$p\,[atm]$	$T\,[K]$
2lsH0.4			
2hsH0.4			
7lsH0.4	0.4	90	732
7hsH0.4			
2lsH10			
2hsH10			
7lsH10	10	45	652
7hsH10			
2lsH50			
2hsH50			
7lsH50	50	1	348
7hsH50			

Table 12: Initial pressure (p) and temperature (T) conditions for the DNS realizations. The corresponding approximate altitude on Venus is indicated (H).

Case	Stream	CO_2	N_2	SO_2	H_2O	H_2S	HCl	HF
2lsH50	$Y_{\alpha,U}$	96.593	3.407	0	0	0	0	0
2lsH10	$Y_{\alpha,L}$	98.879	1.121	0	0	0	0	0
2lsH0.4	$X_{\alpha,U}$	94.75	5.25	0	0	0	0	0
	$X_{\alpha,L}$	98.25	1.75	0	0	0	0	0
7lsH50	$Y_{\alpha,U}$	96.580	3.407	0.011	0.0019	0.00036	0.000076	0.00000035
7lsH10	$Y_{\alpha,L}$	98.846	1.121	0.033	0.0006	0.00012	0.000025	0.00000011
7lsH0.4	$X_{\alpha,U}$	94.737	5.251	0.0074	0.0046	0.00046	0.000080	0.00000076
	$X_{\alpha,L}$	98.226	1.750	0.0225	0.0015	0.00016	0.000030	0.00000024
2hsH50	$Y_{\alpha,U}$	0	100	0	0	0	0	0
2hsH10	$Y_{\alpha,L}$	100	0	0	0	0	0	0
2hsH0.4	$X_{\alpha,U}$	0	100	0	0	0	0	0
	$X_{\alpha,L}$	100	0	0	0	0	0	0
7hsH50	$Y_{\alpha,U}$	0	92.00	0	3.00	2.00	2.00	1.00
7hsH10	$Y_{\alpha,L}$	93.00	1.00	6.00	0	0	0	0
7hsH0.4	$X_{\alpha,U}$	0	90.87	0	4.61	1.62	1.52	1.38
	$X_{\alpha,L}$	94.23	1.59	4.18	0	0	0	0

Table 13: Initial mass (Y_α) and molar (X_α) fractions (in %) for upper and lower streams of the DNS realizations.

A different initial stratification of the species is assumed in the cases listed in 13. In the low-stratified cases (e.g. 7lsH50), the initial molar fractions for the upper and lower streams have a surplus of 50% in molar fraction respect to the nominal composition of the Venus lower atmosphere (table 1) for the heaviest species in the lower stream and a deficit of 50% in molar fraction for the lightest species in the lower stream. The average composition in the entire domain is therefore kept equal to the nominal composition in table 1. The nominal composition considered for the 2-species realizations is similar to that in table 1, the only difference being a larger amount of carbon dioxide to compensate for the lack of the other minor species not considered. The other category of DNSs is that of the high-stratified cases, (e.g. 7hsH50), where the initial composition is pure N_2 in the upper stream and pure CO_2 in the lower stream for the 2-species simulations, and a certain amount of minor species is added in the 7-species realizations (see table 13). Details on the DNS realizations and associated resolutions are provided in table 14.

Case	$\mathcal{F}$	p_0 $[atm]$	$\frac{\rho_L}{\rho_U}$	$\Delta\rho$ $\left[\frac{kg}{m^3}\right]$	$\frac{|\rho U|_L}{|\rho U|_U}$	$Re_{m,tr}$	t_{tr}^*
2lsH50	138	1	1.0131	0.02	1.0065	2227	85
2lsH10	2570	45	1.0141	0.51	1.0070	2220	85
2lsH0.4	4365	90	1.0145	0.93	1.0072	2221	85
7lsH50	138	1	1.0132	0.02	1.0066	2227	85
7lsH10	2571	45	1.0142	0.52	1.0071	2220	85
7lsH0.4	4365	90	1.0146	0.94	1.0073	2221	85
2hsH50	122	1	1.5761	0.57	1.2554	2207	85
2hsH10	2416	45	1.6083	14.06	1.2681	2224	85
2hsH0.4	4155	90	1.6221	25.15	1.2736	2217	85
7hsH50	126	1	1.6165	0.60	1.2714	2231	85
7hsH10	2463	45	1.6471	14.80	1.2833	2228	85
7hsH0.4	4230	90	1.6598	26.43	1.2883	2218	85

Table 14: List of the Direct Numerical Simulation realizations and associated resolution. Information regarding the initial pressure and temperature values and the initial upper stream and lower stream compositions are provided in tables 12 and 13 respectively. The subscript tr denotes the transitional time. The same initial Reynolds number, $Re_0 = 1000$, and the same grid spacing $N_1 \times N_2 \times N_3 = 660 \times 732 \times 396$ were chosen for all cases.

7.4   Results

All the simulations are conducted and time is accounted in time units $t^* = t\triangle U_0/\delta_{\omega,0}$. The simulations are stopped at a transitional time denoted t^*_{tr} at which the one-dimensional fluctuation-based energy spectra become smooth (figure 14), indicating that the initially laminar flow has reached turbulent characteristics. The only non smoothness in the spectra is due to the perturbation frequency introduced in the flow in order to hasten its turbulent transition. Almost all the analysis is conducted at t^*_{tr}. First, we show the quality of the database generated in sec. 7.4.1, providing information about the numerical resolution and the energy spectra at transition. Then, the development of the mixing layer over several time units is discussed in sec. 7.4.2 in order to provide an overview of the flow, whereas the evolution over the time of the integral quantities of the mixing layer is discussed in sec. 7.4.3. Subsequently, the formation of High Density Gradient Magnitude (HDGM) regions and their influence on the vorticity production is analyzed in sec. 7.4.4, followed by a discussion, in sec. 7.4.5, about the temperature distribution in the mixing layer. Finally, mass diffusion of the species is investigated in sec. 7.4.6.

7.4.1   Numerical resolution and spectra at transition

In order to highlight the quality of the DNS database generated, we show as first result the resolution of all the characteristic length scales associated with the turbulent flow. In a turbulent flow the length scales associated with the dynamic fluctuations extend over a wide range, with the smallest scales related to the turbulent kinetic energy dissipation $\langle\varepsilon\rangle \equiv \langle\sigma'_{ij}\partial u'_i/\partial x_j\rangle$, where $(\cdot)'$, denotes fluctuations from the average. The order of magnitude of the smallest dynamic scales is classically provided by the Kolmogorov length scale, defined as follows:

$$\eta_K = \left(\frac{\langle\mu\rangle^3}{\langle\rho\rangle^2\langle\varepsilon\rangle}\right)^{1/4}. \tag{63}$$

The order of magnitude of the thermal length scales related to heat transfer precesses is provided by the Prandtl number, which compares the momentum transfer with the heat transfer. For a binary mixture, the smallest scales involved in thermal transfer phenomena are given by $\eta_\theta = \eta_K \operatorname{Pr}^{-0.5}$; if $\operatorname{Pr} > 1$, it follows that the smallest thermal scales are smaller than the smallest dynamic scales, becoming the limiting factor for the grid spacing resolution. When dealing with multispecie mixtures, besides the dynamic and thermal scales, the length scales related to mass diffusion must also be taken into account. The Schmidt number Sc, which measure the importance of the momentum transfer compared to the mass diffusion transfer, classically provides an estimate of the smallest scales involved in mass diffusion. For a binary mixture, the Batchelor scale, η_B, is related to η_K by $\eta_B = \eta_K \operatorname{Sc}^{-0.5}$. For multispecies mixtures the Sc number can only be defined in an effective diffusion coefficient.

A recent definition of an effective species-specific Schmidt number, $Sc_{\alpha,eff}$ is provided by Masi et al. [27], which accounts the influence of the full matrix of diffusion.

Since in a DNS simulation all the characteristic length scales must be solved, the grid spacing, Δx, must be sufficiently fine to catch all the smallest length scales associated with the dynamic, thermal diffusion and mass diffusion processes. In figure 13 the cross-stream resolution of the dynamic and thermal scales are represented for all the DNS realizations, where the maximum $\Delta x/\eta_K|_{max} < 1.3$ and the maximum $\Delta x/\eta_\theta|_{max} < 1.1$, showing an appropriate spatial resolution of the length scales. The evidence of accurate resolution is presented in figure 14, where the one-dimensional fluctuation-based energy spectra at t_{tr}^*, in both streamwise and spanwise directions, are shown for the dynamic and thermodynamic variables for all the simulations, showing no accumulation of energy in the smallest scales, and therefore indicating that these are well solved on the utilized grid.
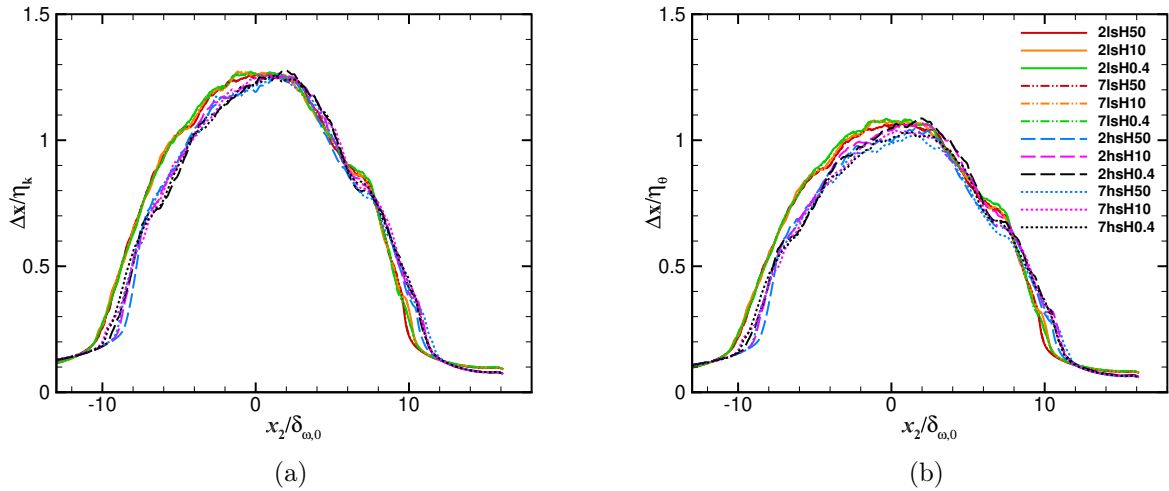

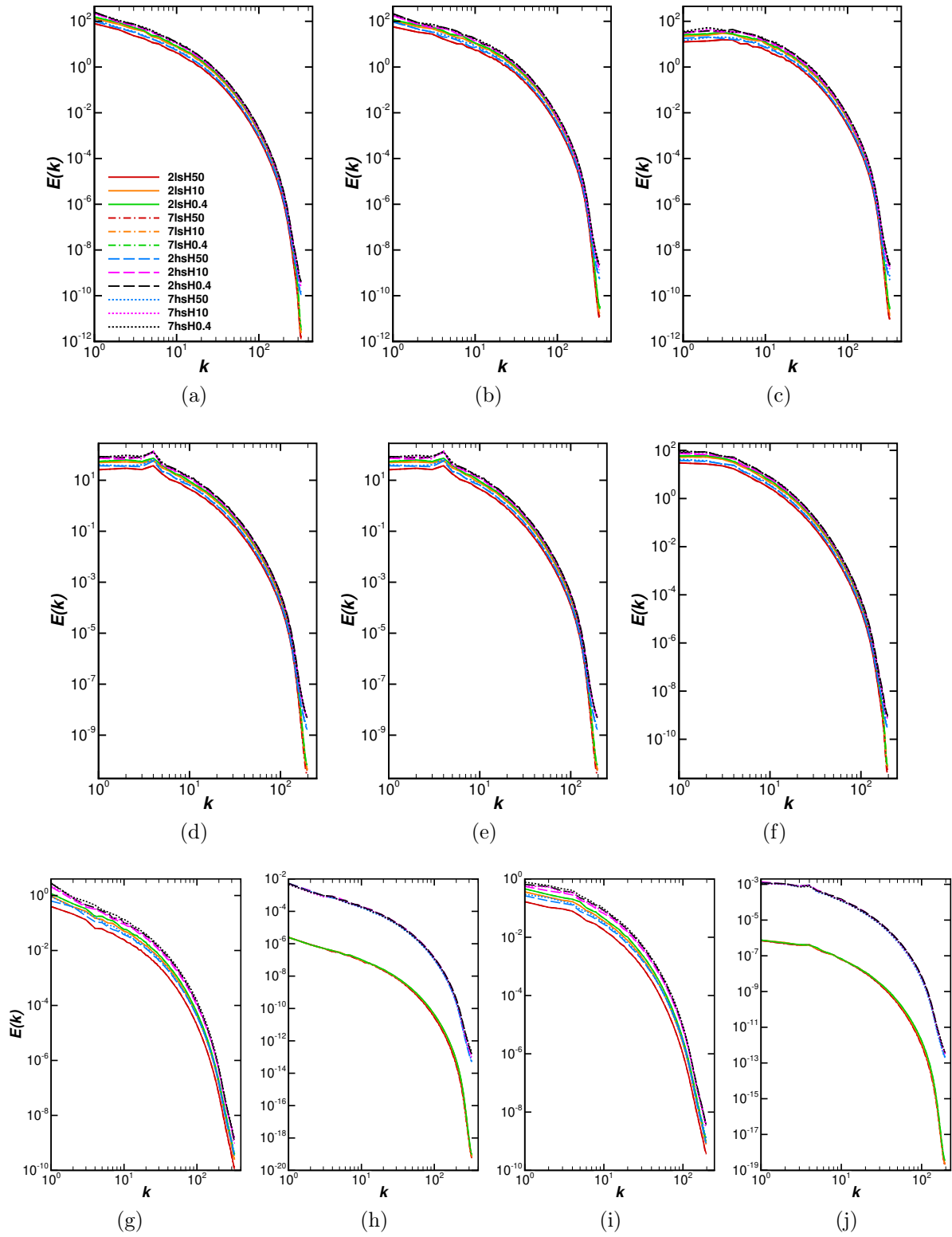Figure 13: Cross-stream resolution of the (a) dynamic and (b) thermal scales for the DNS realizations.

Figure 14: One-dimensional spectra at t_{tr}^* for several simulation: streamwise spectra of (a) u_1, (b) u_2, (c) u_3, (g) T, (h) Y_{CO_2}; spanwise spectra of (d) u_1, (e) u_2, (f) u_3, (i) T, (j) Y_{CO_2}.

7.4.2 Flow field overview

An overview of the mixing layer evolution over time is provided in figure 15, showing several quantities in both a between-the-braid plane ($x_3/L_3 = 0.5$) and the mid-cross plane ($x_1/L_1 = 0.5$), for five selected time steps, from $t^* = 5$ to $t^* = t_{tr}^*$. The initial perturbation is clearly visible in the frames corresponding to $t^* = 5$, then the formation of four vortices in both streamwise and spanwise directions; finally, the merging of the two formed vortices results in a single vortex in which transition to turbulent characteristics occurs. The mixing layer growth in the cross-wise direction is observable in both the between-the-braid plane and the mid-cross plane, a topic which will be addressed in sec. 7.4.3. In figures 15 (a) and (b), respectively, the between-the-braid plane and the mid-cross plane distributions of the local $|\nabla\rho|$ are represented, showing the formation of HDGM features. The influence of the pressure and temperature conditions as well as that of the stratification level on the formation of HDGM regions at t_{tr}^* is addressed in sec. 7.4.4. The between-the-braid plane and the mid-cross plane distribution of the local temperature is represented in figures 15 (c) and (d), respectively, where an increase in temperature is shown for certain regions, even though the initial temperature is set to the same value for both upper and lower streams. In sec. 7.4.5 the influence of the pressure and temperature conditions as well as that of the stratification level on the temperature distribution t_{tr}^* will be discussed. Finally, the between-the-braid plane and the mid-cross plane distributions of Y_{CO_2} are shown in figures 15 (e) and (f), respectively, where it is possible to observe the eventual CO_2 penetration in the upper stream as result of the coupled diffusion and convection phenomena. In sec. 7.4.6 we will discuss the influence of the pressure, temperature, and stratification conditions on the species mass diffusion.
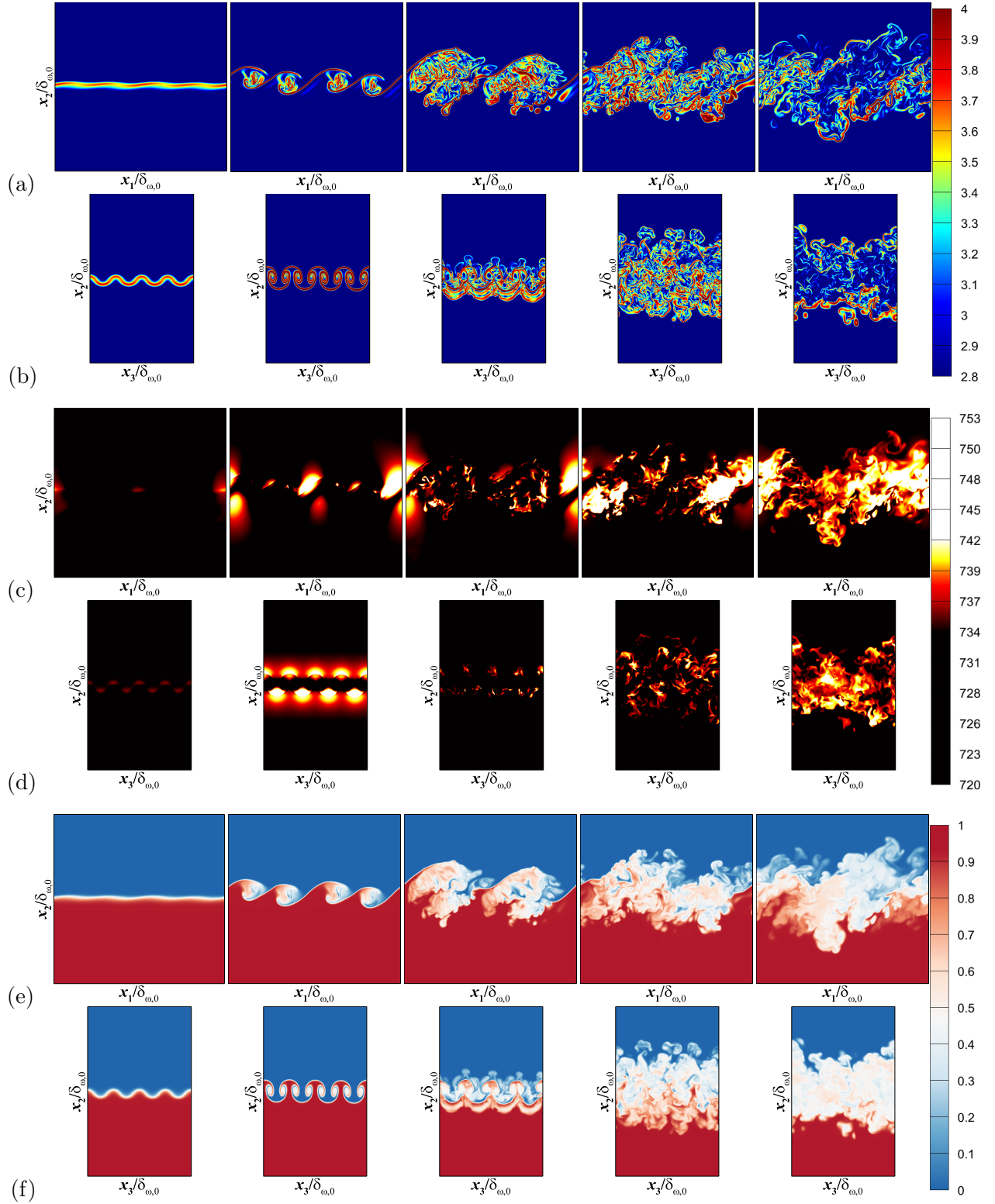
Figure 15: Evolution of several quantities at five time units $t^* = 5, 25, 45, 60, 85(t^*_{tr})$ for 7hsH0.4. (a) Between-the-braid plane ($x_3/L_3 = 0.5$) and (b) Mid-cross plane ($x_1/L_1 = 0.5$) distribution of the local $|\nabla\rho|$ in logarithmic scale $\log_{10}|\nabla\rho|$, units are kg/m^4. (c) Between-the-braid plane and (d) Mid-cross plane distribution of the local temperature, units are K. (e) Between-the-braid plane and (f) Mid-cross plane distribution of the local CO_2 molar fraction, Y_{CO_2}.

7.4.3 Evolution of integral quantities

A typical quantity used to describe the temporal growth of a mixing layer is the momentum thickness, which can be expressed as follows:

$$\delta_m = \frac{\int_{x_2,\min}^{x_2,\max} \left[\langle \rho u_1 \rangle_{x_2,\max} - \langle \rho u_1 \rangle \right] \left[\langle \rho u_1 \rangle - \langle \rho u_1 \rangle_{x_2,\min} \right] \mathrm{d}x_2}{\left(\langle \rho u_1 \rangle_{x_2,\max} - \langle \rho u_1 \rangle_{x_2,\min} \right)^2} \tag{64}$$

where $x_{2,\min} = -0.5L_2$, $x_{2,\max} = 0.5L_2$. The characteristic length scale corresponding to Re_0 is the initial vorticity thickness, $\delta_{\omega,0}$, whereas the momentum-thickness-based Reynolds number, Re_m, is computed using $\delta_m(t^*)$. Therefore, the ratio between the momentum thickness and the initial vorticity thickness at transitional time provides the corresponding, characteristic Reynolds number due to the mixing layer growth. Details of the transitional Reynolds number for all the simulation can be found in table 14. Figure 16 shows the evolution of the ratio $\delta_m/\delta_{\omega,0}$ as function of t^* for the runs listed in table 14. The initial perturbation speeds up the growth of the mixing layer, resulting in a fast increase in the $\delta_m/\delta_{\omega,0}$ slope, leading to an approximately constant growth rate. The growth rate increase monotonically for all the simulations, although a slight decrease in the slope is observed after the enstrophy peak (discussed below). The trend is similar for all the realizations, with a value of the ratio $\delta_m/\delta_{\omega,0}$ about 2.2 at t_{tr}^*, corresponding to a $Re_{m,t_{tr}^*} \simeq 2200$.
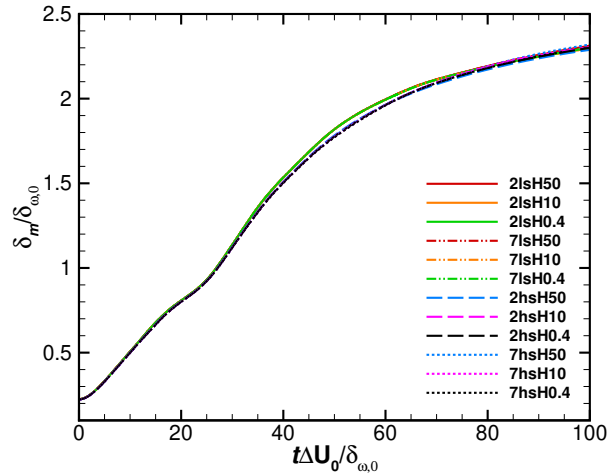

Figure 16: Time-wise evolution of the normalised momentum thickness $\delta_m/\delta_{\omega,0}$.

As the mixing layer starts to growth, the production of vortical structures increases as

shown in figure 17, due to tilting and stretching mechanisms, where the normalised positive spanwise vorticity $\left\langle\left\langle\omega_3^+\right\rangle\right\rangle \delta_{\omega,0}/\Delta U_0$ and the normalised enstrophy $\left\langle\left\langle\omega_i\omega_i\right\rangle\right\rangle \left(\delta_{\omega,0}/\Delta U_0\right)^2$ are displayed ($\left\langle\left\langle\right\rangle\right\rangle$ denotes entire domain averaging). The positive spanwise vorticity gives information about the small scales production, whereas the enstrophy represents the global activity of the turbulence, that is a balance between the vorticity production and the destruction mechanisms. A maximum around $t^* = 45$ is reached for both spanwise vorticity and enstrophy, after which dissipation becomes significant; maximum values are lower for high stratification simulations which correspond to larger ρ_L/ρ_U values, which lead to a smaller vorticity content, as already shown in [2, 35].
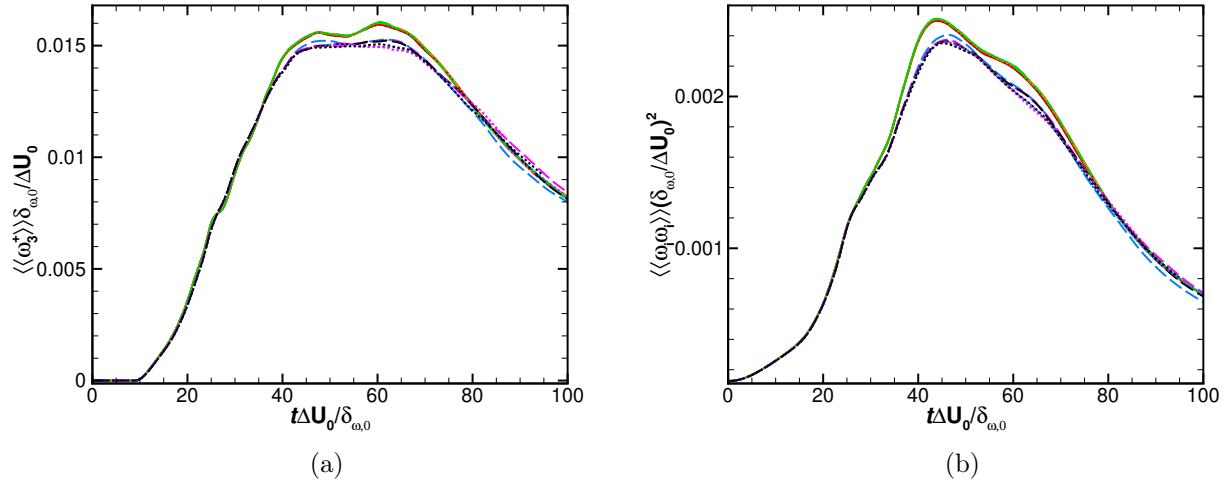

Figure 17: Time-wise evolution of integral quantities: (a) normalised positive spanwise vorticity $\left\langle\left\langle\omega_3^+\right\rangle\right\rangle \delta_{\omega,0}/\Delta U_0$, (b) normalised enstrophy $\left\langle\left\langle\omega_i\omega_i\right\rangle\right\rangle \left(\delta_{\omega,0}/\Delta U_0\right)^2$. Legend as in figure 16.

7.4.4   Density gradients and vorticity production

HDGM regions are generated during mixing under high pressure and temperature conditions, as can be observed in figure 19, where the between-the-braid plane distribution of the local $|\nabla\rho|$ t_{tr}^* is shown for the seven-species simulations at different pressure and temperature conditions and stratifications. The species stratification influences the morphology of the HDGM regions, leading to formation of HDGM features at the mixing layer in high stratification conditions, and to a more homogeneous density distribution in low stratification conditions. The magnitude of the density gradients increases with increasing pressure and temperature, i.e. decreasing the altitude, for both low and high stratification cases. The same conclusions about the influence of pressure, temperature and stratification level can be observed in Figure 18, where the pdfs of $|\nabla\rho|$ at t_{tr}^* are represented for the entire set of simulations. The influence of the number of species on $|\nabla\rho|$ seems to be negligible for the smaller higher-probability $|\nabla\rho|$ values, and it is only significant for the larger smaller-probability $|\nabla\rho|$ values. The larger $|\nabla\rho|$ values occurring for the larger number of species are due to the higher multitude of diffusional scales associated with the increased number of species.
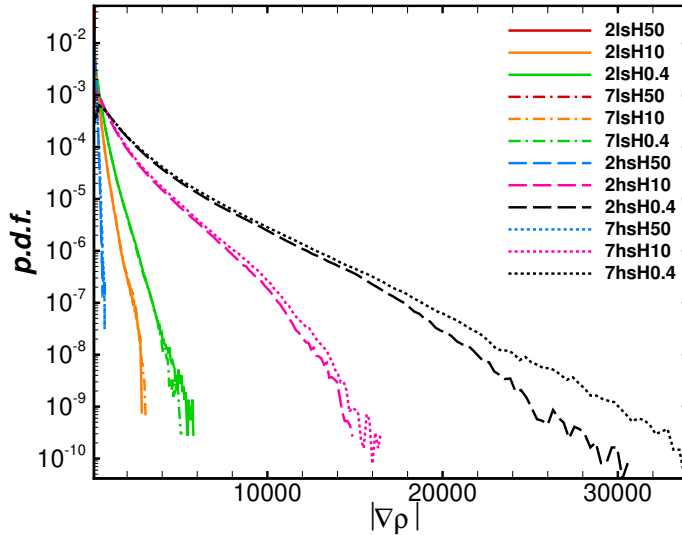

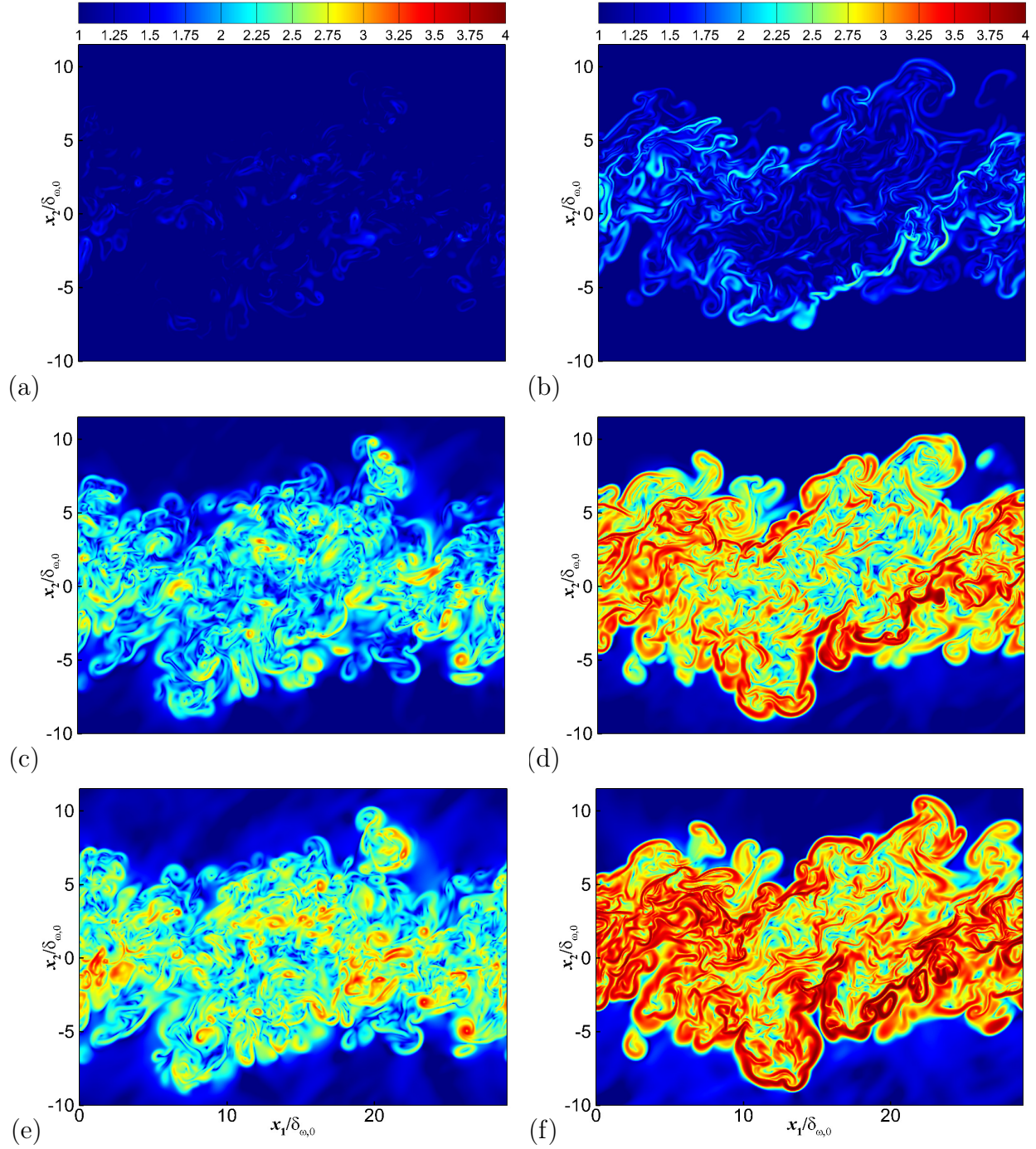Figure 18: Probability density function at t_{tr}^* of $|\nabla\rho|$ (units are kg (m^{-4})).

Figure 19: Between-the-braid plane ($x_3/L_3 = 0.5$) distribution of the local $|\nabla\rho|$ in logarithmic scale $\log_{10} |\nabla\rho|$ at t_{tr}^* for (a) 7lsH50, (b) 7hsH50, (c) 7lsH10, (d) 7hsH10, (e) 7lsH0.4, (f) 7hsH0.4. Units are kg/m^4.

Since HDGM regions have been observed in the mixing layer under high pressure and temperature conditions, one can ask about the impact of the density gradients on the turbulence production. The vorticity equation, which describes the temporal-spatial evolution of the vorticity due to its production and diffusion by various mechanisms, can be expressed as follows:

$$\frac{\partial \boldsymbol{\omega}}{\partial t} + (\mathbf{u} \cdot \nabla)\boldsymbol{\omega} = (\boldsymbol{\omega} \cdot \nabla)\mathbf{u} - \boldsymbol{\omega}(\nabla \cdot \mathbf{u}) + \frac{1}{\rho^2}\nabla\rho \times \nabla p + \nabla \times \left(\frac{\nabla \cdot \tau}{\rho}\right) + \nabla \times \left(\frac{\boldsymbol{B}}{\rho}\right). \quad (65)$$

Where $\boldsymbol{\omega}$ is the vorticity vector, $\mathbf{u}$ the tridimensional velocity, τ is the viscous stress tensor and $\boldsymbol{B}$ represents the sum of the external body forces. The first right-hand term represents the stretching and tilting of vorticity due to the flow velocity gradients; the second right-hand term describes the compressibility effect; the third right-hand term is the baroclinic term, which accounts for the changes in vorticity due to the misalignment of density and pressure gradients; the fourth right-hand term represents the transport of vorticity by the viscous effects; and the last right-hand term accounts for changes due to external body forces, such as gravity.

In figure 20, the between-the-braid plane distribution of the local normalised spanwise baroclinic term $-\left(1/\rho^2\nabla\rho \times \nabla p\right)/\left(\Delta U_0/\delta_{\omega,0}\right)^2$ at t_{tr}^* is represented for the 7-species runs. For all the cases the vorticity production through baroclinic effect increases in the cases with higher magnitude $|\nabla\rho|$, i.e. the high-stratification conditions. There is no a remarkable influence on the vorticity production due to the baroclinic term while simultaneously varying the pressure and temperature values according to table 12. As already observed in figure 17, the positive spanwise vorticity and the enstrophy trends are similar for various simulations, these are the result of not only the baroclinic term, but the sum of the production and transport terms in the equation 65.
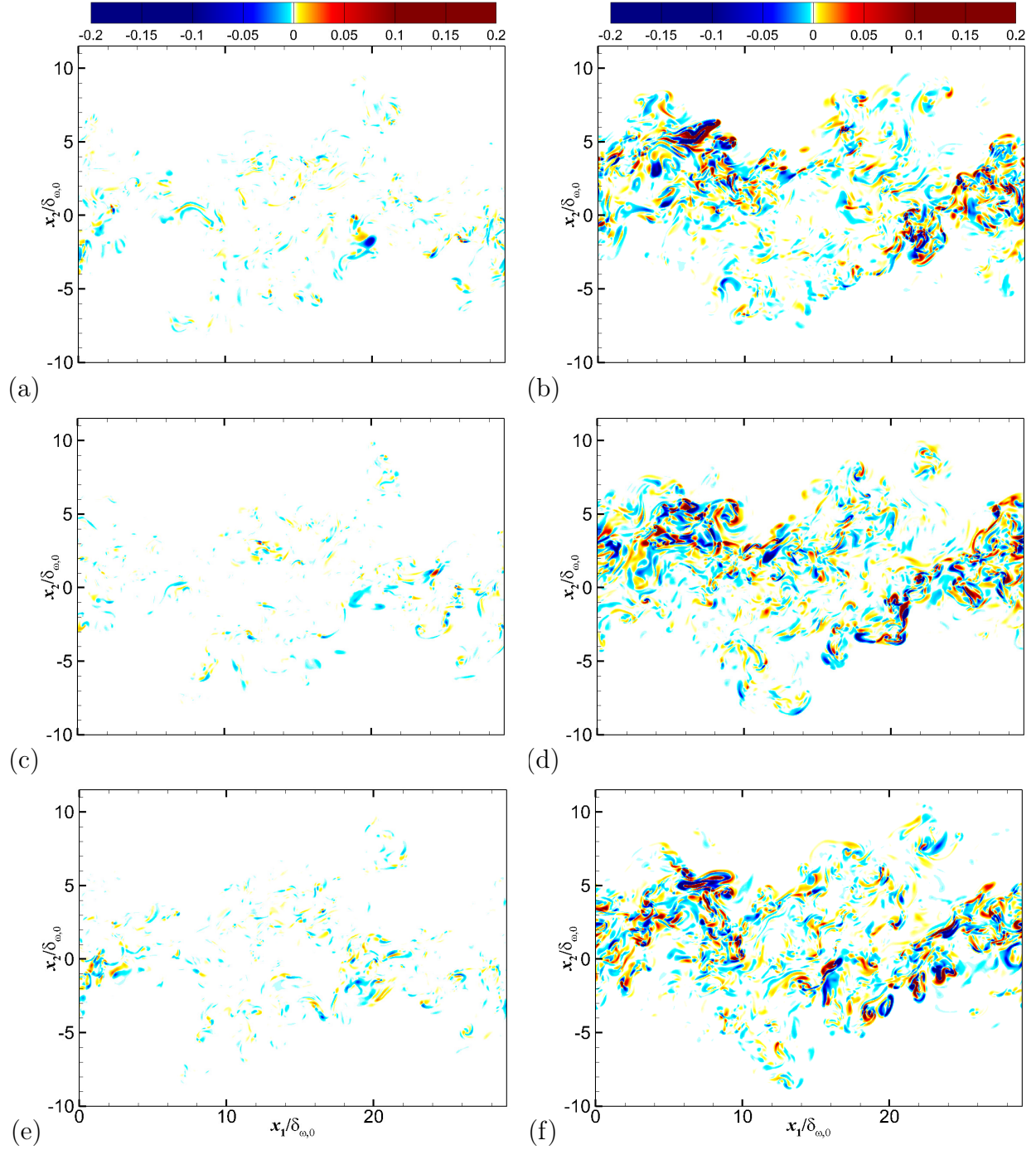
Figure 20: Between-the-braid plane ($x_3/L_3 = 0.5$) distribution of the local normalised spanwise baroclinic term $-\left(1/\rho^2 \nabla \rho \times \nabla p\right)/\left(\Delta U_0/\delta_{\omega,0}\right)^2$ at t_{tr}^* for (a) 7lsH50, (b) 7hsH50, (c) 7lsH10, (d) 7hsH10, (e) 7lsH0.4, (f) 7hsH0.4.

7.4.5 Temperature distribution

The distribution of the local temperature, T, in the between-the-braid plane at t_{tr}^* for the 7-species set of simulations is shown in figures 21, (a)-(f), where different range of temperatures were necessarily used according to altitude. In order to compare the thermal effects for various simulations, a normalized temperature is defined,

$$\theta = \frac{T - T_{ref}}{T_{ref}} \tag{66}$$

with $T_{ref} = T_L = T_U$ according to table 12. The local distribution of θ for the 7-species simulations above is displayed in figures 21, (g)-(l). Starting from the same temperature, mixing under higher stratification levels leads to higher values of temperature, as can be observed from both the computed quantities T and θ, suggesting enhanced dissipation effects at higher stratification. The pressure and the temperature conditions seem to slightly influence the complexity of the temperature distribution, whereas higher values of the normalized temperature are achieved in mixing at higher altitudes. Regions of $\theta < 0$, i.e. temperature lower than the free stream temperature, are overspeed regions in which the increase in speed corresponds to a decrease in temperature.
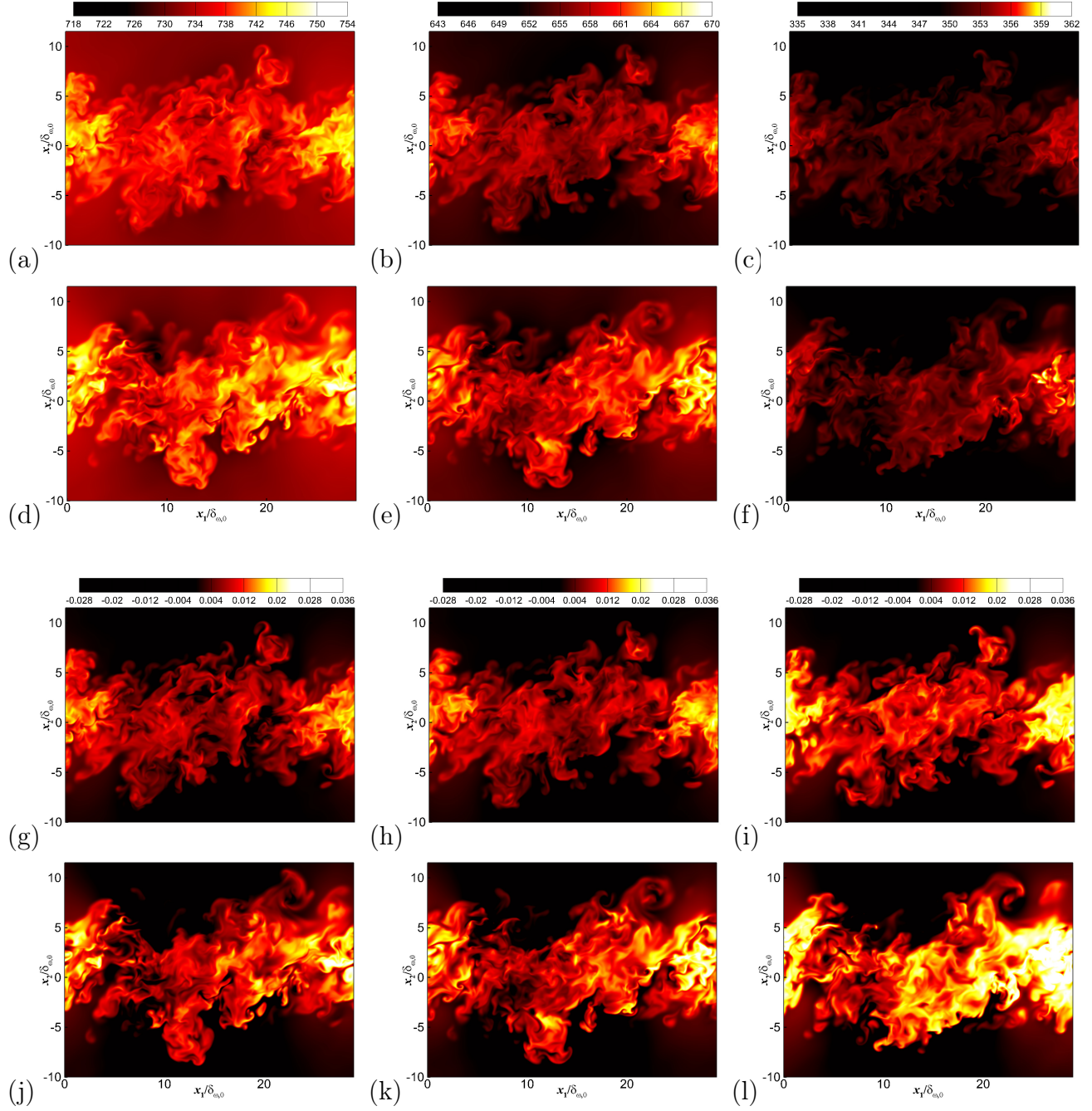
Figure 21: Between-the-braid plane ($x_3/L_3 = 0.5$) distribution of the local temperature, T, at t^*_{tr} for (a) 7lsH0.4, (b) 7lsH10, (c) 7lsH50, (d) 7hsH0.4, (e) 7hsH10, (f) 7hsH50, and normalized temperature, θ, at t^*_{tr} for (g) 7lsH0.4, (h) 7lsH10, (i) 7lsH50, (j) 7hsH0.4, (k) 7hsH10, (l) 7hsH50. Units are K.

7.4.6 Mass diffusion

To analyze the degree of mixing of the species in the mixing layer and compare simulations with different initial mass fractions for upper stream and lower stream, a normalized mass fraction variable is introduced,

$$\Xi_\alpha = \frac{Y_\alpha - Y_{\alpha,ref}^{\min}}{Y_{\alpha,ref}^{\max} - Y_{\alpha,ref}^{\min}} \tag{67}$$

where $Y_{\alpha,ref}^{\max} = max(Y_{\alpha,U}, Y_{\alpha,L})$ and $Y_{\alpha,ref}^{\min} = min(Y_{\alpha,U}, Y_{\alpha,L})$. Therefore, $\Xi_\alpha = 0$ and $\Xi_\alpha = 1$ represent the initial species mass fraction of the upper and lower streams or vice-versa, depending on the free-stream location of the species. In figure 22 we show the distribution of Ξ_{CO2} (a)-(f) and Ξ_{N2} (g)-(l) in the between-the-braid plane at t_{tr}^* for the 2-species runs. There seems to be no remarkable influence of the altitude conditions on the global complexity of the mixing layer. In figures 23 to 28 the Ξ_α distribution at t_{tr}^* in the between-the-braid plane is shown for each component of the 7-species mixture for various cases of species stratification and altitude conditions. Differences in morphology are present in the high stratified runs varying pressure and temperature, whereas no differences in morphology are significant in low stratification conditions. The presence of the minor species does not influence remarkably the Ξ_{CO2} and Ξ_{N2} distributions in the low stratification mixing, as can be seen comparing figures 22 and 23 to 28, whereas discrepancies in the distributions due to the minor species are highlighted in the high stratification mixing, where the lower the altitude is (i.e. higher pressure and temperature), the larger are the differences in the distributions of Ξ_{CO2} and Ξ_{N2}, with formation of structures penetrating the free streams in the 7-species cases. The last attention is given to the uphill diffusion phenomenon, whose existence has already been experienced [12], and simulated [8]. In our simulations values of $\Xi_\alpha < 0$ and $\Xi_\alpha > 0$ are $O(10^{-4})$, showing negligible presence of uphill diffusion regions.
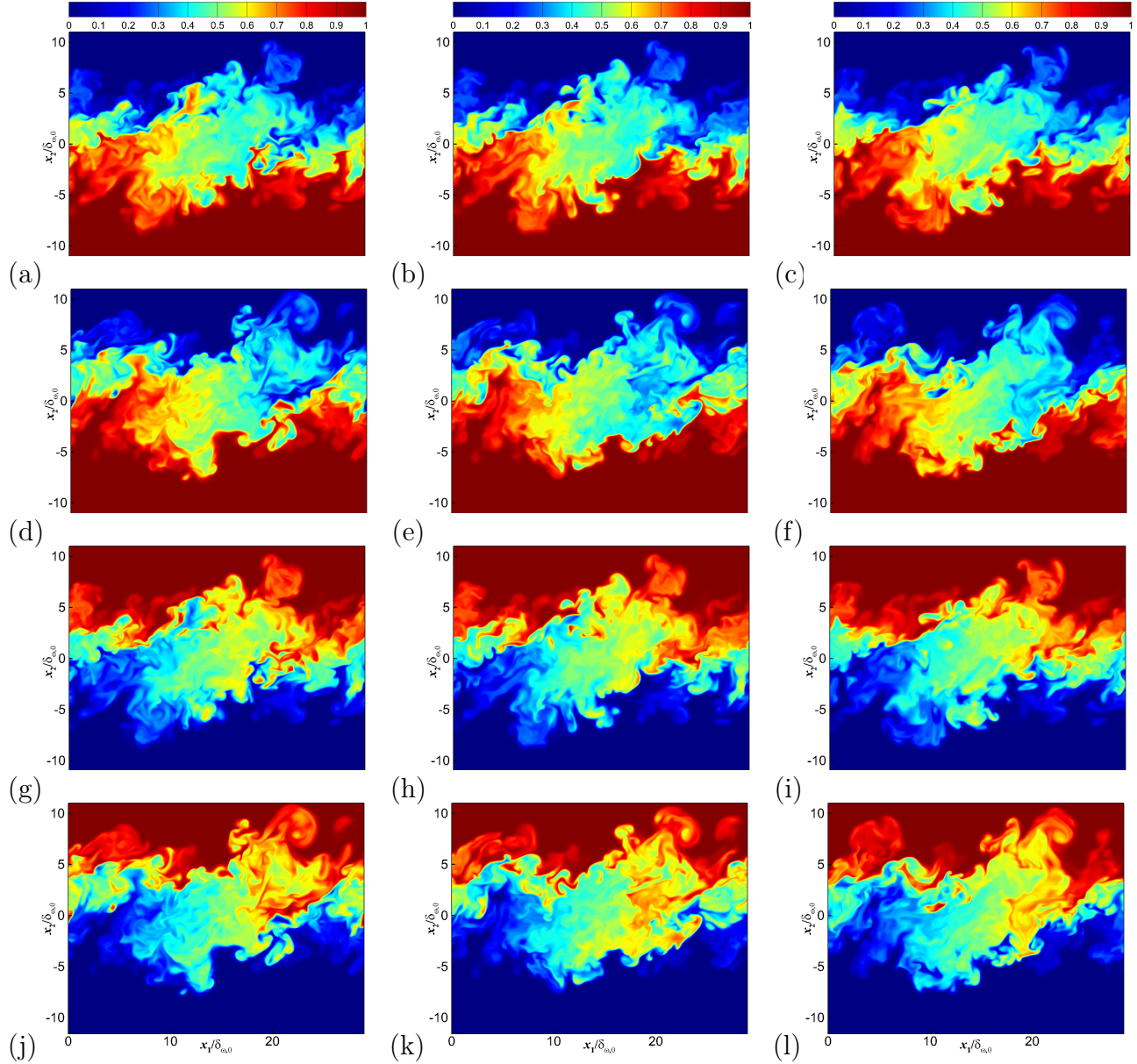
Figure 22: Between-the-braid plane ($x_3/L_3 = 0.5$) distribution of normalized mass fraction, Ξ_{CO_2}, at t_{tr}^* for (a) 2lsH0.4, (b) 2lsH10, (c) 2lsH50, (d) 2hsH0.4, (e) 2hsH10, (f) 2hsH50, and normalized mass fraction, Ξ_{N_2}, at t_{tr}^* for (g) 2lsH0.4, (h) 2lsH10, (i) 2lsH50, (j) 2hsH0.4, (k) 2hsH10, (l) 2hsH50.
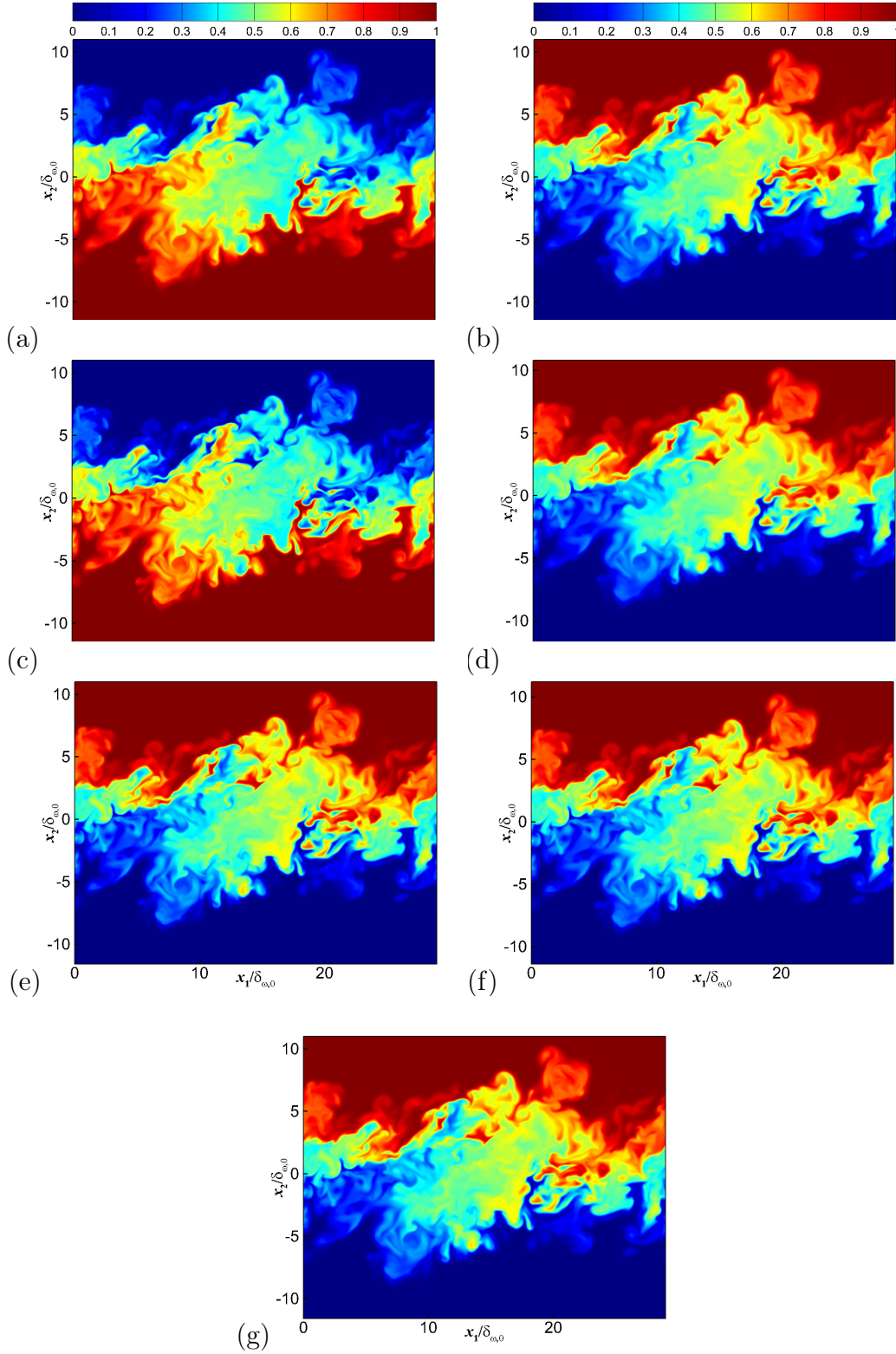
Figure 23: Between-the-braid plane ($x_3/L_3 = 0.5$) distribution of normalized mass fractions at t_{tr}^* for 7lsH0.4. (a) Ξ_{CO_2}, (b) Ξ_{N_2}, (c) Ξ_{SO_2}, (d) Ξ_{H_2O}, (e) Ξ_{H_2S}, (f) Ξ_{HCl}, (g) Ξ_{HF}.
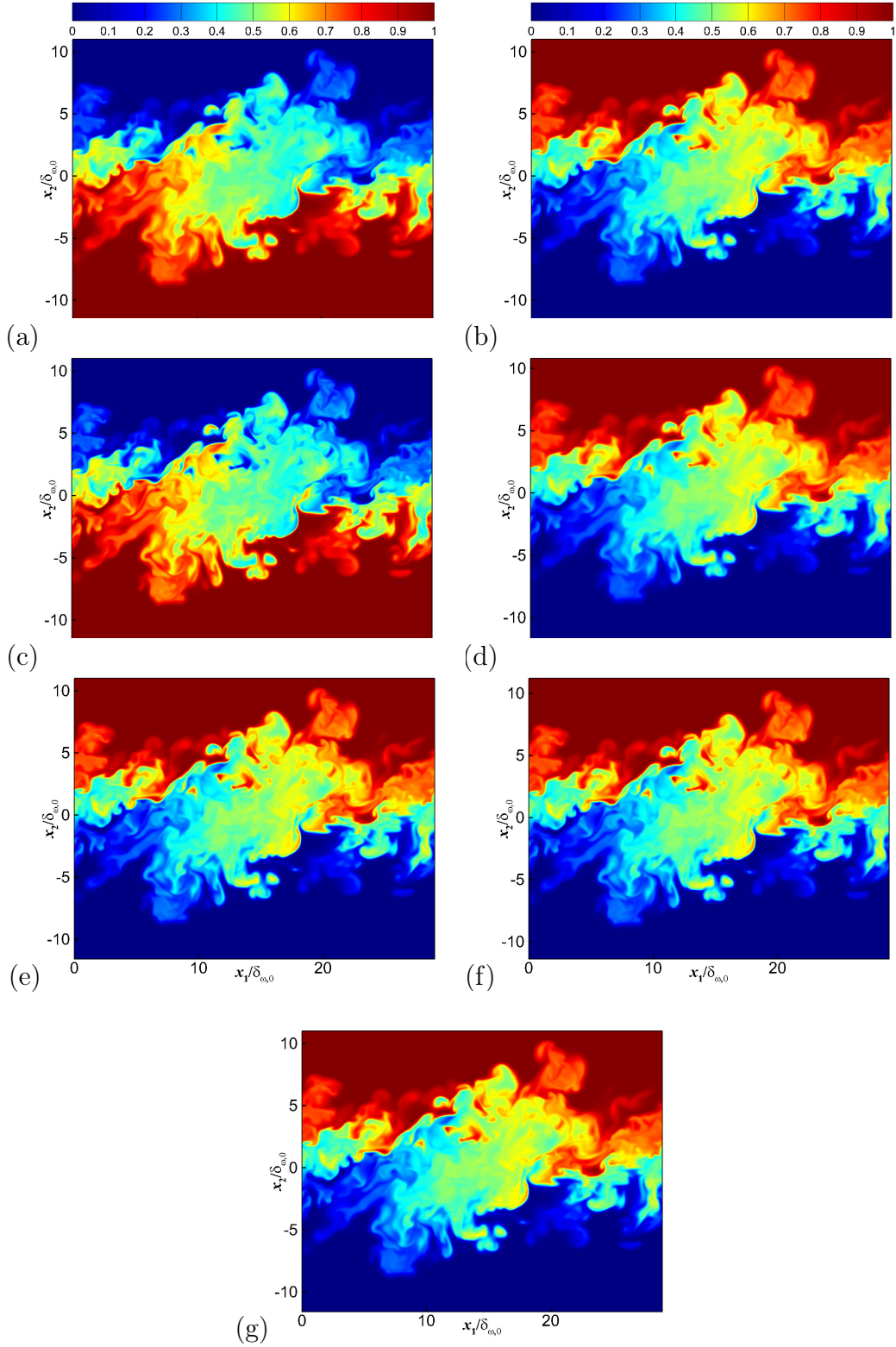
Figure 24: Between-the-braid plane $(x_3/L_3 = 0.5)$ distribution of normalized mass fractions at t_{tr}^* for 7lsH10. (a) Ξ_{CO_2}, (b) Ξ_{N_2}, (c) Ξ_{SO_2}, (d) Ξ_{H_2O}, (e) Ξ_{H_2S}, (f) Ξ_{HCl}, (g) Ξ_{HF}.

Figure 25: Between-the-braid plane ($x_3/L_3 = 0.5$) distribution of normalized mass fractions at t_{tr}^* for 7lsH50. (a) Ξ_{CO_2}, (b) Ξ_{N_2}, (c) Ξ_{SO_2}, (d) Ξ_{H_2O}, (e) Ξ_{H_2S}, (f) Ξ_{HCl}, (g) Ξ_{HF}.
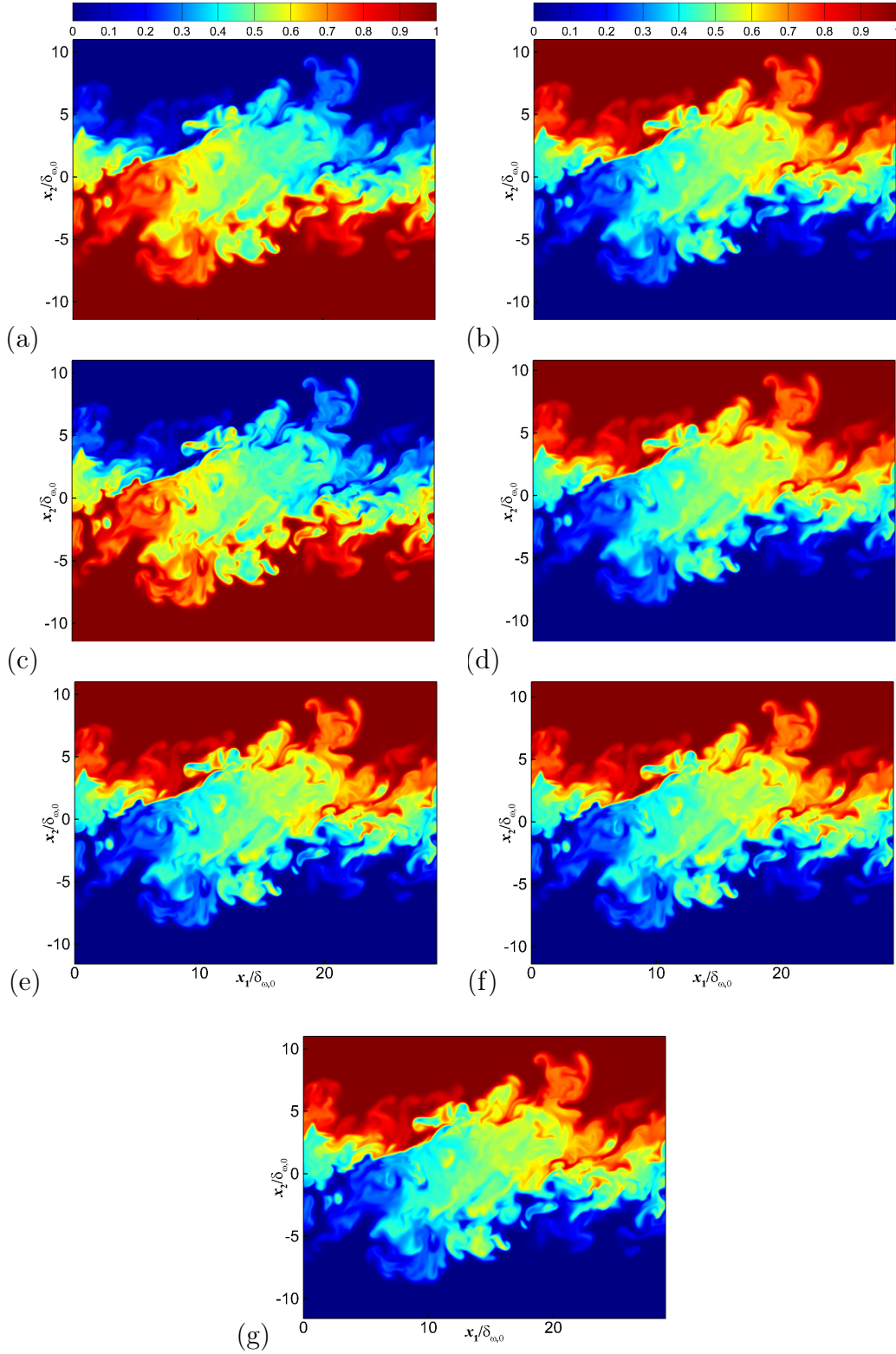
Figure 26: Between-the-braid plane ($x_3/L_3 = 0.5$) distribution of normalized mass fractions at t_{tr}^* for 7hsH0.4. (a) Ξ_{CO_2}, (b) Ξ_{N_2}, (c) Ξ_{SO_2}, (d) Ξ_{H_2O}, (e) Ξ_{H_2S}, (f) Ξ_{HCl}, (g) Ξ_{HF}.

Figure 27: Between-the-braid plane ($x_3/L_3 = 0.5$) distribution of normalized mass fractions at t_{tr}^* for 7hsH10. (a) Ξ_{CO_2}, (b) Ξ_{N_2}, (c) Ξ_{SO_2}, (d) Ξ_{H_2O}, (e) Ξ_{H_2S}, (f) Ξ_{HCl}, (g) Ξ_{HF}.
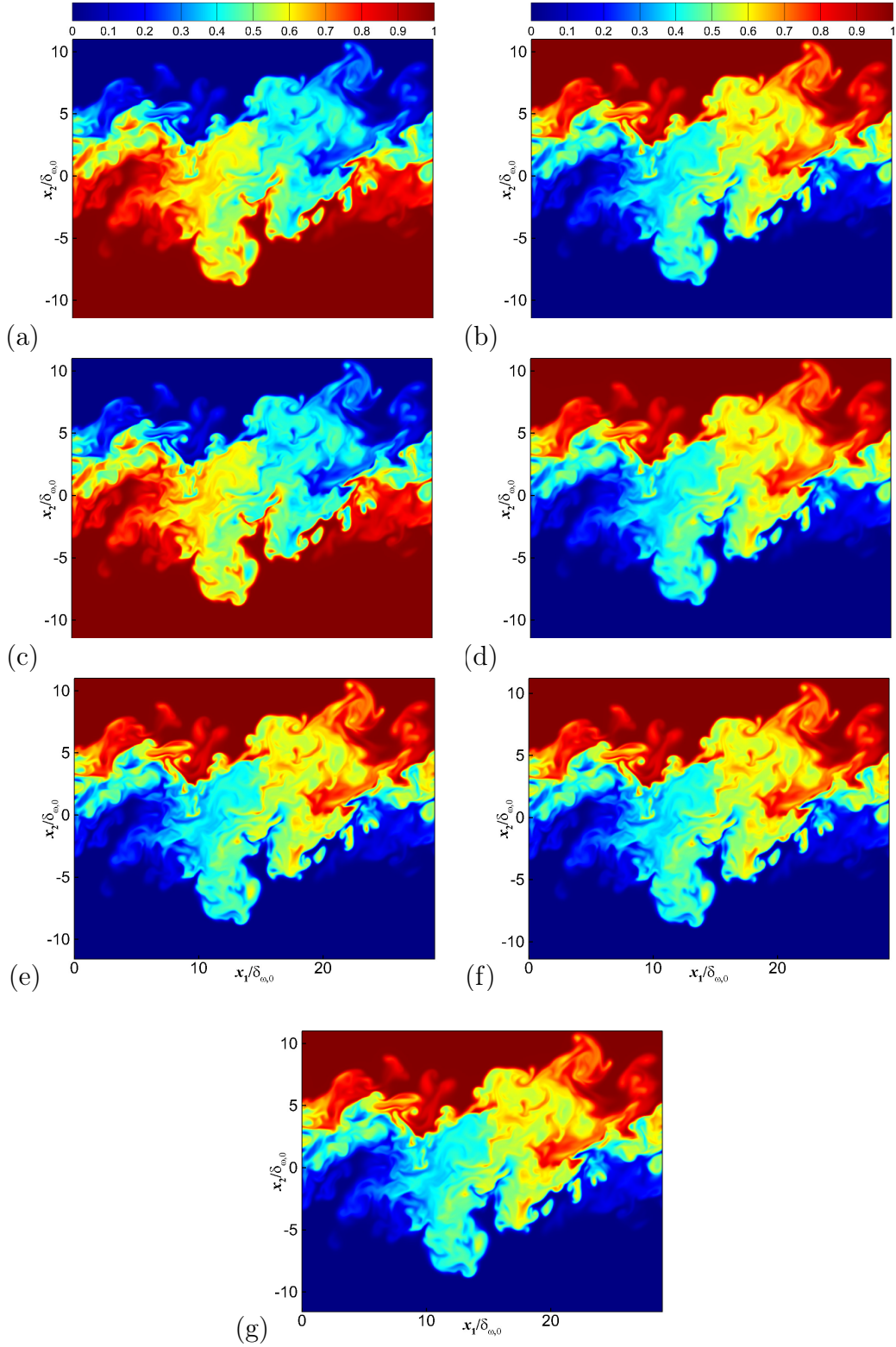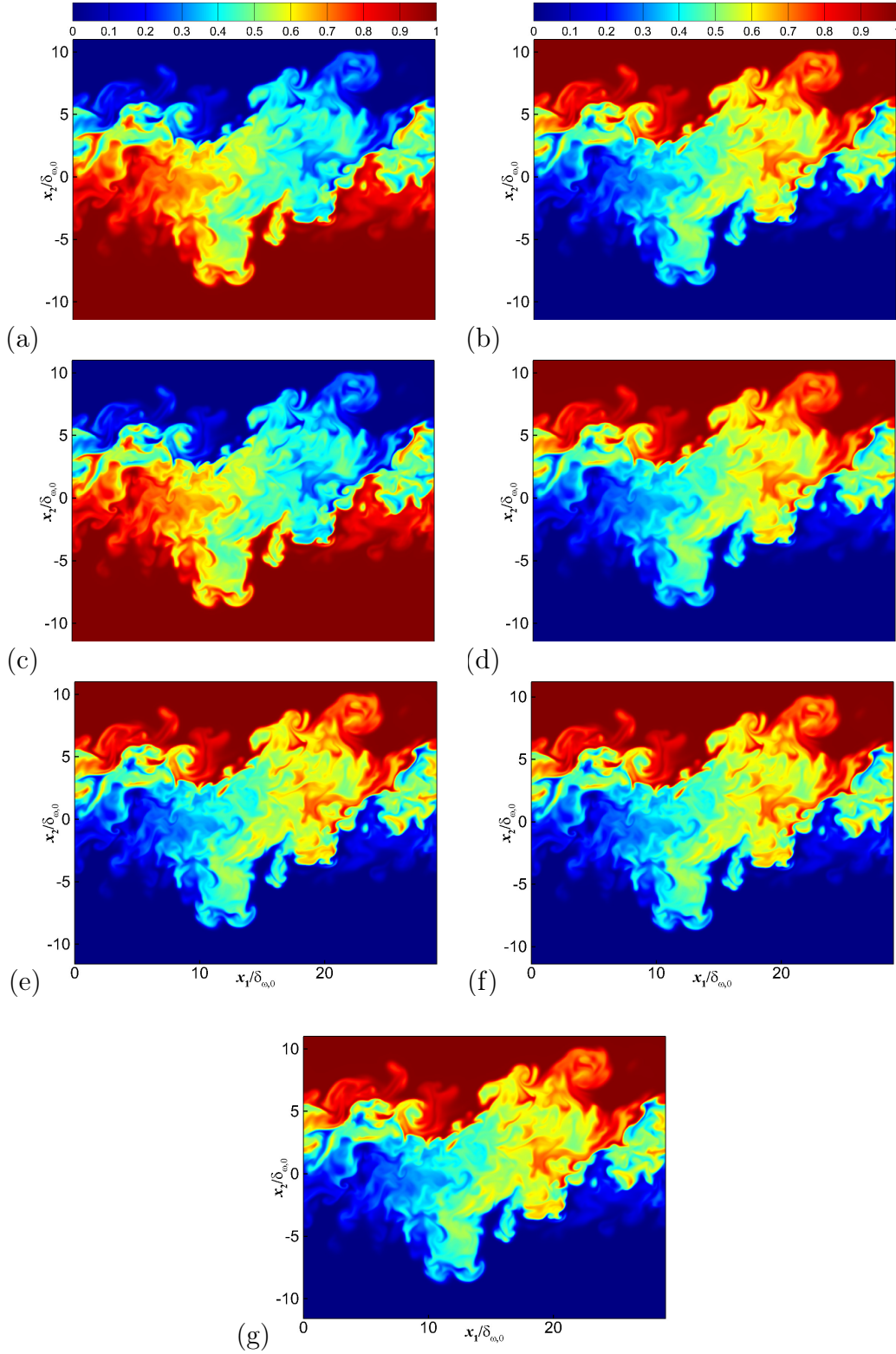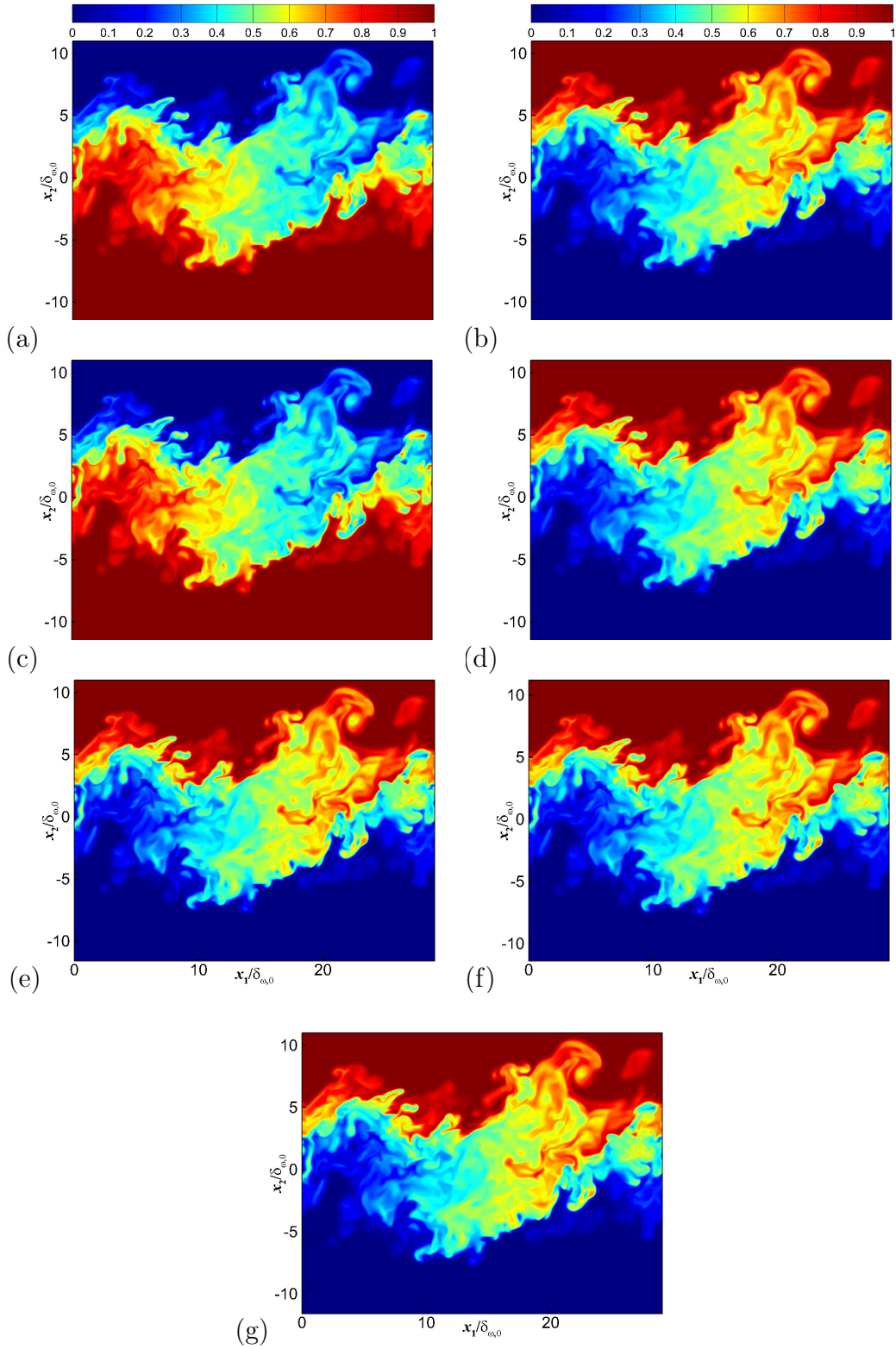
Figure 28: Between-the-braid plane ($x_3/L_3 = 0.5$) distribution of normalized mass fractions at t_{tr}^* for 7hsH50. (a) Ξ_{CO_2}, (b) Ξ_{N_2}, (c) Ξ_{SO_2}, (d) Ξ_{H_2O}, (e) Ξ_{H_2S}, (f) Ξ_{HCl}, (g) Ξ_{HF}.

8 Summary and conclusions

The general thermodynamics and transport characteristics of the Venus lower atmosphere have been calculated at different altitudes with particular attention to the models used to compute the density and the transport properties of the mixtures present. The results favorably match with those in literature, obtained under the same thermodynamic conditions, with errors depending on the models and the assumptions on the mixture composition. Real gas effects and presence of the very minor species seems not to change considerably the thermodynamic of the mixture, resulting in a compressibility factor nearly unity, with a maximum error varying from 1% to 3% respect to the ideal gas behavior, depending on the mixture composition. This error is perhaps negligible for those applications which require a rough value of the density, but it must be taken into account for high-accuracy modelling or scientific purposes.

The dynamic characteristics of the lower part of the atmosphere have been computed using the mixture properties calculated herein and data from Venus space missions and it was found that the entire lower atmosphere is in a fully-turbulent flow regime.

The thermodynamic regime of various mixtures of interest in the study of the Venus atmosphere has been computed, highlighting the stability and instabilities regions. The presence of nitrogen in the mixture changes significantly the limit of thermodynamic stability (i.e. the spinodal shape), whereas the minor species seem to do not have influence. Whatever the mixture considered, correspondent to a different degree of approximation towards the nominal Venus atmosphere, the thermodynamic regime at the realistic pressure and temperature on Venus is collocated in the stable-monophasic regime for the first 65 km, with supercritical conditions occurring in the first few kilometers. Following the thermodynamic theory, no transient-unstable phenomena such as rains are then expected to take place in the lower atmosphere of Venus.

A substantial mixing layer DNS database has been generated for several 2 and 7 species mixtures with different degrees of stratification and with realistic values of pressure and temperature present on Venus at different altitudes. High density-gradient magnitude regions were shown to form in high stratification conditions, with larger values obtained at low altitudes, where supercritical conditions occur. These regions were shown to increase the vorticity production through the baroclinic effect; mixing in low stratification conditions results in a more homogeneous distribution of the density. The influence of the minor species on the global behavior of the flow seems to be negligible under low stratification, whereas differences in the species-diffusion are observed in high stratification conditions.

Beside the fundamental results regarding mixing under different conditions of altitude and stratification, the DNS database generated might be used as good starting point for understanding the requirements for setting up LES simulations in order to simulate more realistic

cases such as large computational domains at high Reynolds number. For further studies, a template LES solution can be obtained by filtering and coarsening the DNS database, and it can be used to choose the most accurate LES model to describe the problem.

The level of influence of the minor species for modelling the Venus lower atmosphere depends upon the engineering or scientific application. If the atmosphere were really stratified, then the minor species may not be negligible; only experimental measurements on Venus will clarify the actual situation. As of now, accurate simulations are helpful to develop models for the exploration and the physical understanding of the planet.

A   Spinodal locus

This appendix duplicates information provided as a personal communication [9] to the author.

A.1   Pure components

The spinodal locus is characterized by the condition in which a macroscopic system is unstable. In case the system is formed by a pure substance only, the instability is simultaneously mechanical and thermal [11], while multispecies mixtures may have composition fluctuations [11, 44]. When working with EOS of the form $p = f(V, T, N)$ is convenient to write the stability condition as:

$$-\left(\frac{\partial p}{\partial V}\right)_{T,N} > 0 \tag{68}$$

where p is the pressure, V is the extensive volume, T is the temperature, and N is the number of molecules. Therefore the stability condition is first violated when

$$\left(\frac{\partial p}{\partial V}\right)_{T,N} = 0 \tag{69}$$

which is by definition the spinodal locus.

It is also interesting to re-write equation (68) in terms of measurable quantities, for instance

$$-\left(\frac{\partial p}{\partial v}\right)_{T} = \frac{1}{vK_T} > 0 \tag{70}$$

where K_T is the isothermal compressibility, and $v = V/n$ is the molar volume (n being the number of moles with $n = N/N_A$ where N_A is the Avogadro's number). From equation (70) we can see that at the spinodal line the isothermal compressibility for a pure substance diverges, i.e. $K_T \to \infty$.

Criticality condition

The coefficients for a cubic EOS, such as van der Waals or Peng-Robinson EOS, can be expressed in terms of the critical point. The critical point satisfies equation (69) and

$$\left(\frac{\partial^2 p}{\partial V^2}\right)_{T,N} = 0 \tag{71}$$

Peng-Robinson EOS

The intensive, molar form of the Peng-Robinson EOS is

$$p = \frac{RT}{(v-b)} - \frac{a}{v^2 + 2bv - b^2} \tag{72}$$

with

$$a = a_c \left[1 + C \left(1 - \sqrt{\frac{T}{T_c}} \right) \right]^2 \tag{73}$$

and

$$C = 0.37464 + 1.54222\omega - 0.2699\omega^2 \tag{74}$$

so we can write in compact form

$$a = a_c f(\omega, T) \tag{75}$$

where ω is the acentric (Pitzer) factor, while b and a_c are obtained from the criticality conditions (see equations (69) and (71)).

Spinodal locus for Peng-Robinson

From the Peng-Robinson EOS, equation (72), the spinodal locus is

$$\left(\frac{\partial p}{\partial v} \right)_T = -\frac{RT}{(v-b)^2} + \frac{2a(v+b)}{(v^2 + 2bv - b^2)^2} = 0 \tag{76}$$

and the critical point condition

$$\left(\frac{\partial^2 p}{\partial v^2} \right)_T = \frac{2RT}{(v-b)^3} + \frac{2a}{(v^2 + 2bv - b^2)^2} - \frac{8a(v+b)^2}{(v^2 + 2bv - b^2)^3} = 0 \tag{77}$$

By equating (76) with (77), and evaluating at the critical point (p_c, T_c, v_c), we can obtain the following relations

$$v_c = 3.95137303559144\,b \tag{78}$$

$$RT_c = 0.17014442007035\,\frac{a}{b} \tag{79}$$

$$p_c = 0.0132365678781272\,\frac{a}{b^2} \tag{80}$$

and the correspondent reciprocal relations

$$a_c = 0.457235528921383 \, \frac{R^2 T_c^2}{p_c} \tag{81}$$

$$b = 0.07779607390388851 \, \frac{R T_c}{p_c} \tag{82}$$

From equation (76) we get the spinodal temperature T_{sp} as function of the molar volume

$$\frac{T}{f(\omega, T)} = \frac{2a_c}{R} \frac{(v + b)(v - b)^2}{(v^2 + 2bv - b^2)^2} \tag{83}$$

note that this equation needs to be solved iteratively. From substituting equation (76) into equation (72) we get a relation between the spinodal pressure p_{sp} and the molar volume

$$p_{sp} = a_c f(\omega, T) \frac{(v^2 - 2bv - b^2)}{(v^2 + 2bv - b^2)^2} \tag{84}$$

Alternatively the pressure can be computed directly from the EOS once the temperature is computed from eq 83.

A.2 Mixtures

Spinodal locus of binary mixtures

In pure substances near the critical point density can have unbounded fluctuations. Unlike for pure substances in binary mixtures the fluctuations are of composition [11], the instability in this case is of thermodynamic nature and not mechanical. This type of instability is called diffusional or material instability. The stability condition for a binary mixture is [11, 44]

$$-\left(\frac{\partial \mu_1}{\partial N_1}\right)_{T,P,N_2} > 0 \tag{85}$$

where μ_i is the chemical potential of the component i and N_i is the number of molecules of component i. Equivalently we can write

$$-\left(\frac{\partial \mu_1}{\partial n_1}\right)_{T,P,n_2} > 0 \tag{86}$$

where n_i is the number of moles of component i. The spinodal locus for a binary mixture is located where (85) is first violated, therefore the spinodal locus is

$$\left(\frac{\partial \mu_1}{\partial n_1}\right)_{T,P,n_2} = 0 \tag{87}$$

For convenience, the spinodal locus can be rewritten for pressure-explicit EOS

$$\left(\frac{\partial \mu_1}{\partial n_1}\right)_{T,P,N_2} = \left(\frac{\partial \mu_1}{\partial n_1}\right)_{T,V,N_2} - V K_T \left[\left(\frac{\partial p}{\partial n_1}\right)_{T,V,N_2}\right]^2 = 0 \tag{88}$$

together with the identity [44]

$$\left(\frac{\partial \mu_1}{\partial n_1}\right)_{T,V,N_2} = \int_V^\infty \left(\frac{\partial^2 p}{\partial n_1^2}\right)_{T,V,N_2} dV + \frac{RT}{n_1} \tag{89}$$

we can get a fully pressure-explicit spinodal locus equation

$$\int_V^\infty \left(\frac{\partial^2 p}{\partial n_1^2}\right)_{T,V,N_2} dV + \frac{RT}{n_1} - V K_T \left[\left(\frac{\partial p}{\partial n_1}\right)_{T,V,N_2}\right]^2 = 0 \tag{90}$$

Where,

$$K_T = -\frac{1}{V}\left[\left(\frac{\partial p}{\partial V}\right)_T\right]^{-1} \tag{91}$$

Multi-components Peng-Robinson EOS

The molar extensive form of Peng-Robinson EOS is

$$p = \frac{nRT}{(V - nb_{mix})} - \frac{n^2 a_{mix}}{V^2 + 2nb_{mix}V - n^2 b_{mix}{}^2} \tag{92}$$

given the definitions of molar fraction $x_i = n_i/n$, therefore $n_i = x_i n$ with $n = \sum_\alpha n_\alpha$, it follows

$$n^2 a_{mix} = n^2 \sum_\alpha \sum_\gamma x_\alpha x_\gamma a_{\alpha\gamma}(T) = \sum_\alpha \sum_\gamma n_\alpha n_\gamma a_{\alpha\gamma}(T) \tag{93}$$

$$nb_{mix} = n \sum_\alpha x_\alpha b_\alpha = \sum_\alpha n_\alpha b_\alpha \tag{94}$$

where Greek indexes do not follow Einstein notation.

$$a_{\alpha\gamma}(T) = \left(1 - k'_{\alpha\gamma}\right) \sqrt{a_{\alpha\alpha} a_{\gamma\gamma}} \tag{95}$$

$$a_{\alpha\alpha}(T) = 0.457235528921383 \, \frac{R^2 T_{c\alpha}^2}{p_{c\alpha}} \left[1 + C_\alpha \left(1 - \sqrt{\frac{T}{T_{c\alpha}}}\right)\right]^2 \tag{96}$$

$$C_\alpha = 0.37464 + 1.54222\omega_\alpha - 0.2699\omega_\alpha^2 \tag{97}$$

where $p_{c\alpha}$, $T_{c\alpha}$, and ω_α are the species specific critical pressure, critical temperature, and acentric factor. The interaction parameters $k'_{\alpha\gamma}$ are derived experimentally. Finally

$$b_\alpha = 0.07779607390388851 \, \frac{RT_{c\alpha}}{p_{c\alpha}} \tag{98}$$

Note, the pseudo-critical mixture estimates are not be needed for the calculation of the spinodal locus.

Binary mixture spinodal locus for Peng-Robinson EOS

To compute equation (90) we are interested in computing the quantities $\left(\frac{\partial p}{\partial n_1}\right)_{T,v}$, $\left(\frac{\partial^2 p}{\partial n_1^2}\right)_{T,v}$, and $\left(\frac{\partial p}{\partial V}\right)_{T,n}$. In the Peng-Robinson EOS only a_{mix} and b_{mix} are dependent on the molar fraction. Therefore it is handy to compute the followings

$$\left(\frac{\partial n^2 a_{mix}}{\partial n_i}\right)_{T,V,n_j} = 2 \sum_\gamma n_\gamma a_{i\gamma}(T) = \alpha_i \tag{99}$$

$$\left(\frac{\partial nb_{mix}}{\partial n_i}\right)_{T,V,n_j} = b_i \tag{100}$$

$$\frac{\partial}{\partial n_j}\left[\left(\frac{\partial n^2 a_{mix}}{\partial n_i}\right)_{T,V,n_j}\right]_{T,V,n_k} = \frac{\partial}{\partial n_j}\left(\alpha_i\right)_{T,V,n_k} = 2a_{ij} \tag{101}$$

$$\frac{\partial}{\partial n_j}\left[\left(\frac{\partial nb_{mix}}{\partial n_i}\right)_{T,V,n_j}\right]_{T,V,n_k} = \frac{\partial}{\partial n_j}\left(b_i\right)_{T,V,n_k} = 0 \tag{102}$$

it follows

$$\left(\frac{\partial p}{\partial n_i}\right)_{T,V,n_j} = \frac{RT}{V - nb_{mix}} + nRT\frac{\left(\frac{\partial nb_{mix}}{\partial n_i}\right)_{T,V,n_j}}{\left(V - nb_{mix}\right)^2}$$
$$- \frac{\left(\frac{\partial n^2 a_{mix}}{\partial n_i}\right)_{T,V,n_j}}{V^2 + 2nb_{mix}V - n^2 b_{mix}^2}$$
$$+ \frac{n^2 a_{mix}\left[2\left(\frac{\partial nb_{mix}}{\partial x_i}\right)_{T,V,n_j}\left(V - nb_{mix}\right)\right]}{\left(V^2 + 2nb_{mix}V - n^2 b_{mix}^2\right)^2} \tag{103}$$

$$\left(\frac{\partial p}{\partial n_i}\right)_{T,V,n_j} = \frac{RT}{V - nb_{mix}} + nRT\frac{b_i}{\left(V - nb_{mix}\right)^2}$$
$$- \frac{\alpha_i}{V^2 + 2nb_{mix}V - n^2 b_{mix}^2}$$
$$+ \frac{n^2 a_{mix}\left[2b_i\left(V - nb_{mix}\right)\right]}{\left(V^2 + 2nb_{mix}V - n^2 b_{mix}^2\right)^2} \tag{104}$$

and

$$
\frac{\partial}{\partial n_j}\left[\left(\frac{\partial p}{\partial n_i}\right)_{T,v,n_j}\right]_{T,v,n_k} = \frac{RTb_j}{(V-nb_{mix})^2} + RT\frac{b_i}{(V-nb_{mix})^2} + nRTb_i\frac{2b_j}{(V-nb_{mix})^3}
$$
$$
- \frac{2a_{ij}}{V^2+2nb_{mix}V-n^2b_{mix}^2} + \alpha_i\frac{2b_j\left(V-nb_{mix}\right)}{(V^2+2nb_{mix}V-n^2b_{mix}^2)^2}
$$
$$
+ \alpha_j\frac{2b_i\left(V-nb_{mix}\right)}{(V^2+2nb_{mix}V-n^2b_{mix}^2)^2} + 0 + \frac{n^2a_{mix}2b_i\left(-b_j\right)}{(V^2+2nb_{mix}V-n^2b_{mix}^2)^2}
$$
$$
- \frac{n^2a_{mix}\left[2b_i\left(V-nb_{mix}\right)\right]}{(V^2+2nb_{mix}V-n^2b_{mix}^2)^3}2b_j\left(V-nb_{mix}\right) \tag{105}
$$

$$
\frac{\partial}{\partial n_j}\left[\left(\frac{\partial p}{\partial n_i}\right)_{T,v,n_j}\right]_{T,v,n_k} = \frac{RT(b_i+b_j)}{(V-nb_{mix})^2} + \frac{2nRTb_ib_j}{(V-nb_{mix})^3} - \frac{2a_{ij}}{V^2+2nb_{mix}V-n^2b_{mix}^2}
$$
$$
+ \frac{2(\alpha_ib_j+\alpha_jb_i)\left(V-nb_{mix}\right)}{(V^2+2nb_{mix}V-n^2b_{mix}^2)^2} - \frac{2n^2a_{mix}b_ib_j}{(V^2+2nb_{mix}V-n^2b_{mix}^2)^2}
$$
$$
- \frac{4n^2a_{mix}b_ib_j\left(V-nb_{mix}\right)^2}{(V^2+2nb_{mix}V-n^2b_{mix}^2)^3} \tag{106}
$$

Finally the last computation is the integral $\int_V^\infty \left(\frac{\partial^2 p}{\partial n_1^2}\right)_{T,V,n_2} dV$ which, for convenience, is done term by term below

$$
\left(\frac{\partial^2 p}{\partial n_1^2}\right)_{T,V} = \frac{C_1}{(V-nb_{mix})^2} + \frac{C_2}{(V-nb_{mix})^3} + \frac{C_3}{V^2+2nb_{mix}V-n^2b_{mix}^2}
$$
$$
+ \frac{C_4\left(V-nb_{mix}\right)}{(V^2+2nb_{mix}V-n^2b_{mix}^2)^2} + \frac{C_5}{(V^2+2nb_{mix}V-n^2b_{mix}^2)^2}
$$
$$
+ \frac{C_6\left(V-nb_{mix}\right)^2}{(V^2+2nb_{mix}V-n^2b_{mix}^2)^3} \tag{107}
$$

Where it follows that the constants $(C_1\text{-}C_6)$ are defined as follow

$$C_1 = RT(b_i + b_j) \tag{108}$$
$$C_2 = 2nRTb_ib_j \tag{109}$$
$$C_3 = -2a_{ij} \tag{110}$$
$$C_4 = 2(\alpha_i b_j + \alpha_j b_i) \tag{111}$$
$$C_5 = -2n^2 a_{mix} b_i b_j \tag{112}$$
$$C_6 = -4n^2 a_{mix} b_i b_j \tag{113}$$

First term (the subscript on b is dropped and the intensive molar form is used for compactness)

$$C_1 \int_v^\infty \frac{1}{(v-b)^2} dv = C_1 \frac{1}{-b+v}$$
$$= -\frac{C_1}{v-b} \tag{114}$$

Second term

$$C_2 \int_v^\infty \frac{1}{(v-b)^3} dv = C_2 \frac{1}{2b^2 - 4bv + 2v^2}$$
$$= \frac{C_2}{2(v-b)^2} \tag{115}$$

Third term

$$C_3 \int_v^\infty \frac{1}{v^2 + 2bv - b^2} dv = -C_3 \frac{1}{b} \left(-\frac{\sqrt{2}}{4} \log\left(b + \sqrt{2}b + v \right) + \frac{\sqrt{2}}{4} \log\left(-\sqrt{2}b + b + v \right) \right)$$
$$= \frac{C_3 \sqrt{2}}{4b} \log\left(\frac{b(1+\sqrt{2}) + v}{b(1-\sqrt{2}) + v} \right) \tag{116}$$

Fourth term

$$C_4 \int_v^\infty \frac{(v-b)}{(v^2 + 2bv - b^2)^2} dv =$$

$$= C_4 \left[-\frac{v}{-2b^3 + 4b^2 v + 2bv^2} - \frac{1}{b^2} \left(-\frac{\sqrt{2}}{8} \log\left(b + \sqrt{2}b + v\right) + \frac{\sqrt{2}}{8} \log\left(-\sqrt{2}b + b + v\right) \right) \right]$$

$$= \frac{C_4}{2b} \left[-\frac{v}{v^2 + 2bv - b^2} + \frac{\sqrt{2}}{4b} \log\left(\frac{b(1 + \sqrt{2}) + v}{b(1 - \sqrt{2}) + v} \right) \right] \tag{117}$$

Fifth term

$$C_5 \int_v^\infty \frac{1}{(v^2 + 2bv - b^2)^2} dv =$$

$$= C_5 \left[\frac{b + v}{-4b^4 + 8b^3 v + 4b^2 v^2} - \frac{1}{b^3} \left(\frac{\sqrt{2}}{16} \log\left(b + \sqrt{2}b + v\right) - \frac{\sqrt{2}}{16} \log\left(-\sqrt{2}b + b + v\right) \right) \right]$$
$$\tag{118}$$

$$= \frac{C_5}{4b^2} \left[\frac{b + v}{-b^2 + 2bv + v^2} - \frac{\sqrt{2}}{4b} \log\left(\frac{b(1 + \sqrt{2}) + v}{b(1 - \sqrt{2}) + v} \right) \right] \tag{119}$$

Sixth term

$$C_6 \int_v^\infty \frac{(v - b)^2}{(v^2 + 2bv - b^2)^3} dv =$$

$$= C_6 \left[-\frac{-b^3 - 7b^2 v + 15bv^2 + 5v^3}{16b^6 - 64b^5 v + 32b^4 v^2 + 64b^3 v^3 + 16b^2 v^4} \right.$$
$$\left. - \frac{1}{b^3} \left(-\frac{5\sqrt{2}}{64} \log\left(b + \sqrt{2}b + v\right) + \frac{5\sqrt{2}}{64} \log\left(-\sqrt{2}b + b + v\right) \right) \right]$$
$$= C_6 \left[\frac{3v - b}{4 (v^2 + 2bv - b^2)^2} - \frac{5 (v + b)}{16b^2 (v^2 + 2bv - b^2)} + \frac{5}{16} \frac{\sqrt{2}}{4b^3} \log\left(\frac{b(1 + \sqrt{2}) + v}{b(1 - \sqrt{2}) + v} \right) \right] \tag{120}$$

A.3   Method of Heidemann and Khalil

The stability condition presented in section A.2 is costly to compute as it involves the calculation of the first and second derivative with respect to the number of moles and the derivative with respect to volume. Another method, computationally less expensive, has been proposed in the past by Heidemann and Khalil [1, 19, 32]. Critical criteria are found by examining the stability of homogeneous phases. A given phase held at a specific condition will be stable if for every isothermal variation

$$\left[A - A_0 + p_0(V - V_0) - \sum_i \mu_{i0}(n_i - n_{i0}) \right] > 0 \tag{121}$$

where A is the Helmholtz free energy. A scalar variation of volume and number of moles does not qualify as a change of phase, to discard this possibility ΔV is set to zero

$$\left[A - A_0 - \sum_i \mu_{i0}(n_i - n_{i0}) \right] > 0 \tag{122}$$

The Helmholtz free energy can be expanded in a Taylor series around the test point

$$\left[A - A_0 + p_0(V - V_0) - \sum_i \mu_{i0}\Delta n_i \right] = \frac{1}{2!} \sum_j \sum_i \left(\frac{\partial^2 A}{\partial n_j \partial n_i} \right) \Delta n_i \Delta n_i$$
$$+ \frac{1}{3!} \sum_k \sum_j \sum_i \left(\frac{\partial^3 A}{\partial n_k \partial n_j \partial n_i} \right) \Delta n_i \Delta n_j \Delta n_k + O(\Delta n^4) \tag{123}$$

The stability is assured if the quadratic term in equation (123) is positive definite. A necessary condition for a point to lie on the limit of stability is that the matrix $\mathbf{Q}$ defined as

$$q_{ij} = \frac{\partial^2 A}{\partial n_j \partial n_i} \tag{124}$$

should have zero determinant. The stability condition is therefore given by the condition $\det \mathbf{Q} > 0$, where

$$q_{ij} = \left(\frac{\partial^2 A}{\partial n_i \partial n_j} \right)_{T,v} = RT \left(\frac{\partial \log f_i}{\partial n_j} \right)_{T,v} \tag{125}$$

where f_i the fugacity function.

Fugacity function for Peng-Robinson EOS

The fugacity function for a mixture is defined as [44]

$$RT\, log\left(\frac{f_i}{x_i p}\right) = -\int_{\infty}^{V}\left[\left(\frac{\partial p}{\partial n_i}\right)_{T,V,n_j} - \frac{RT}{V}\right]dV - RT\, logZ \tag{126}$$

with $Z = pV/nRT$. The molar extensive form of Peng-Robinson EOS is

$$p = \frac{nRT}{(V - nb_{mix})} - \frac{n^2 a_{mix}}{V^2 + 2nb_{mix}V - n^2 {b_{mix}}^2} \tag{127}$$

given the definitions of molar fraction $x_i = n_i/n$, therefore $n_i = x_i n$ with $n = \sum_\alpha n_\alpha$, it follows

$$n^2 a_{mix} = \sum_\alpha \sum_\gamma n_\alpha n_\gamma a_{\alpha\gamma}(T) \tag{128}$$

$$nb_{mix} = \sum_\alpha n_\alpha b_\alpha \tag{129}$$

$$\left(\frac{\partial n^2 a_{mix}}{\partial n_i}\right)_{T,V,n_j} = 2\sum_\gamma n_\gamma a_{i\gamma}(T) = \alpha_i \tag{130}$$

$$\left(\frac{\partial nb_{mix}}{\partial n_i}\right)_{T,V,n_j} = b_i \tag{131}$$

$$\frac{\partial}{\partial n_j}\left[\left(\frac{\partial n^2 a_{mix}}{\partial n_i}\right)_{T,V,n_j}\right]_{T,V,n_i} = \frac{\partial}{\partial n_j}\left(\alpha_i\right)_{T,V,n_i} = 2a_{ij} \tag{132}$$

$$\frac{\partial}{\partial n_j}\left[\left(\frac{\partial nb_{mix}}{\partial n_i}\right)_{T,V,n_j}\right]_{T,V,n_i} = \frac{\partial}{\partial n_j}\left(b_i\right)_{T,V,n_i} = 0 \tag{133}$$

Then we can compute

$$\left(\frac{\partial p}{\partial n_i}\right)_{T,V,n_j} = \frac{RT}{V - nb_{mix}} + nRT\frac{\left(\frac{\partial nb_{mix}}{\partial n_i}\right)_{T,V,n_j}}{(V - nb_{mix})^2}$$

$$- \frac{\left(\frac{\partial n^2 a_{mix}}{\partial n_i}\right)_{T,V,n_j}}{V^2 + 2nb_{mix}V - n^2 b_{mix}^2}$$

$$+ \frac{n^2 a_{mix}\left[2\left(\frac{\partial nb_{mix}}{\partial x_1}\right)_{T,V,n_j}(V - nb_{mix})\right]}{\left(V^2 + 2nb_{mix}V - n^2 b_{mix}^2\right)^2} \tag{134}$$

substituting (130) and (131)

$$\left(\frac{\partial p}{\partial n_i}\right)_{T,V,n_j} = \frac{RT}{V - nb_{mix}} + nRT \frac{b_i}{(V - nb_{mix})^2}$$
$$- \frac{-\alpha_i}{V^2 + 2nb_{mix}V - n^2b_{mix}^2}$$
$$+ \frac{n^2 a_{mix} 2b_i (V - nb_{mix})}{(V^2 + 2nb_{mix}V - n^2b_{mix}^2)^2} \tag{135}$$

Finally we need to calculate the integral in (126). Term by term:

$$\int_\infty^V \left[\frac{RT}{V - nb_{mix}}\right] dV = RT \, log(V - nb_{mix}) - \infty \tag{136}$$

$$\int_\infty^V \left[\frac{RTnb_i}{(V - nb_{mix})^2}\right] dV = -\frac{RTnb_i}{V - nb_{mix}} \tag{137}$$

$$\int_\infty^V \left[-\frac{\alpha_i}{V^2 + 2nb_{mix}V - n^2b_{mix}^2}\right] dV = -\alpha_i \frac{\sqrt{2}}{4nb_{mix}} \log\left(\frac{nb_{mix}(1 - \sqrt{2}) + V}{nb_{mix}(1 + \sqrt{2}) + V}\right) \tag{138}$$

$$\int_\infty^V \left[\frac{n^2 a_{mix} 2b_i (V - nb_{mix})}{(V^2 + 2nb_{mix}V - n^2b_{mix}^2)^2}\right] dV =$$

$$= \frac{n^2 a_{mix} 2b_i}{2nb_{mix}} \left[\frac{V}{V^2 + 2nb_{mix}V - n^2b_{mix}^2} + \frac{\sqrt{2}}{4nb_{mix}} \log\left(\frac{nb_{mix}(1 - \sqrt{2}) + V}{nb_{mix}(1 + \sqrt{2}) + V}\right)\right] \tag{139}$$

$$\int_\infty^V \left[-\frac{RT}{V}\right] dV = -RT \, log(V) + \infty \tag{140}$$

Plus and minus infinity between (136) and (140) cancel each other out. The first term in (139) can be re-written using the EOS (127)

$$\frac{b_i V}{nb_{mix}} \left[\frac{n^2 a_{mix}}{V^2 + 2nb_{mix}V - n^2b_{mix}^2}\right] = \frac{b_i V}{nb_{mix}} \left[\frac{nRT}{V - nb_{mix}} - p\right] \tag{141}$$

and combining with (138)

$$\frac{b_i}{b_{mix}}\left[\frac{VRT}{V-nb_{mix}}-\frac{pV}{n}\right]-\frac{RTnb_i}{V-nb_{mix}}=\frac{b_i}{b_{mix}}\left[\frac{VRT}{V-nb_{mix}}-\frac{pV}{n}-\frac{RTnb_{mix}}{V-nb_{mix}}\right]$$

$$=\frac{b_i}{b_{mix}}\left[\frac{VRT-\frac{pV}{n}(V-nb_{mix})-RTnb_{mix}}{V-nb_{mix}}\right]$$

$$=\frac{b_i}{b_{mix}}\left[\frac{RT(V-nb_{mix})-\frac{pV}{n}(V-nb_{mix})}{V-nb_{mix}}\right]$$

$$=\frac{b_i}{b_{mix}}\left[RT-\frac{pV}{n}\right] \tag{142}$$

Summing (136) with (140)

$$RTlog(V-nb_{mix})-RTlogV=RTlog\left(\frac{V-nb_{mix}}{V}\right)$$

$$=RTlog\left(1-\frac{B}{Z}\right) \tag{143}$$

with $B=b_{mix}p/RT$. Finally we can compute the fugacity function

$$RT\,log\left(\frac{f_i}{x_ip}\right)=-RTlog\left(1-\frac{B}{Z}\right)-\frac{b_i}{b_{mix}}\left[RT-\frac{pV}{n}\right]$$

$$+\alpha_i\frac{\sqrt{2}}{4nb_{mix}}\log\left(\frac{nb_{mix}(1-\sqrt{2})+V}{nb_{mix}(1+\sqrt{2})+V}\right)$$

$$-\frac{na_{mix}b_i}{b_{mix}}\left[\frac{\sqrt{2}}{4nb_{mix}}\log\left(\frac{nb_{mix}(1-\sqrt{2})+V}{nb_{mix}(1+\sqrt{2})+V}\right)\right]-RT\,logZ \tag{144}$$

substituting for Z, B, and $A=a_{mix}P/R^2T^2$ we get the fugacity function for the Peng-Robinson EOS [44, 1]

$$logf_i=\frac{b_i}{b_{mix}}(Z-1)-log\left(\frac{Z-B}{x_ip}\right)+\frac{A}{2\sqrt{2}B}\left[\frac{\alpha_i}{a_{mix}}-\frac{b_i}{b_{mix}}\right]\log\left(\frac{B(1-\sqrt{2})+Z}{B(1+\sqrt{2})+Z}\right) \tag{145}$$

To calculate the derivative of the fugacity function we re-start from the derivation of the fugacity function before the EOS substitution in term (139)

$$
\begin{aligned}
RTlog\left(\frac{f_i}{x_i p}\right) = & -RTlog\left(\frac{V - nb_{mix}}{V}\right) + \frac{RTnb_i}{V - nb_{mix}} \\
& + \frac{\sqrt{2}\alpha_i}{4nb_{mix}} \log\left(\frac{nb_{mix}(1 - \sqrt{2}) + V}{nb_{mix}(1 + \sqrt{2}) + V}\right) \\
& - \frac{n^2 a_{mix} b_i}{nb_{mix}} \left[\frac{V}{V^2 + 2Vnb_{mix} - n^2 b_{mix}^2} + \frac{\sqrt{2}}{4nb_{mix}} \log\left(\frac{nb_{mix}(1 - \sqrt{2}) + V}{nb_{mix}(1 + \sqrt{2}) + V}\right)\right] \\
& - RTlog\left(\frac{pV}{nRT}\right)
\end{aligned} \tag{146}
$$

combining $RTlog$ terms and dividing by RT

$$
\begin{aligned}
log(f_i) = & log\left(x_i p \frac{nRT}{pV} \frac{V}{V - nb_{mix}}\right) + \frac{nb_i}{V - nb_{mix}} \\
& + \frac{\sqrt{2}\alpha_i}{4RTnb_{mix}} \log\left(\frac{nb_{mix}(1 - \sqrt{2}) + V}{nb_{mix}(1 + \sqrt{2}) + V}\right) \\
& - \frac{n^2 a_{mix} b_i}{RTnb_{mix}} \left[\frac{V}{V^2 + 2Vnb_{mix} - n^2 b_{mix}^2} + \frac{\sqrt{2}}{4nb_{mix}} \log\left(\frac{nb_{mix}(1 - \sqrt{2}) + V}{nb_{mix}(1 + \sqrt{2}) + V}\right)\right]
\end{aligned} \tag{147}
$$

$$
\begin{aligned}
log(f_i) = & log\left(\frac{n_i RT}{V - nb_{mix}}\right) + \frac{nb_i}{V - nb_{mix}} \\
& + \frac{\sqrt{2}\alpha_i}{4RTnb_{mix}} \log\left(\frac{nb_{mix}(1 - \sqrt{2}) + V}{nb_{mix}(1 + \sqrt{2}) + V}\right) \\
& - \frac{n^2 a_{mix} b_i}{RTnb_{mix}} \left[\frac{V}{V^2 + 2Vnb_{mix} - n^2 b_{mix}^2} + \frac{\sqrt{2}}{4nb_{mix}} \log\left(\frac{nb_{mix}(1 - \sqrt{2}) + V}{nb_{mix}(1 + \sqrt{2}) + V}\right)\right]
\end{aligned} \tag{148}
$$

We can now compute the derivative of the fugacity function

$$\frac{\partial \log(f_i)}{\partial n_j} = \frac{V - nb_{mix}}{n_i RT} \frac{\partial}{\partial n_j}\left(\frac{n_i RT}{V - nb_{mix}}\right) + \frac{b_i}{V - nb_{mix}}\frac{\partial n}{\partial n_j} + nb_i\frac{\partial}{\partial n_j}\left(\frac{1}{V - nb_{mix}}\right)$$

$$+ \frac{\partial \alpha_i}{\partial n_j}\frac{\sqrt{2}}{4RTnb_{mix}}log\left(\frac{nb_{mix}(1-\sqrt{2})+V}{nb_{mix}(1+\sqrt{2})+V}\right) + \alpha_i\frac{\partial}{\partial n_j}\left(\frac{1}{nb_{mix}}\right)\frac{\sqrt{2}}{4RT}log\left(\frac{nb_{mix}(1-\sqrt{2})+V}{nb_{mix}(1+\sqrt{2})+V}\right)$$

$$+ \frac{\sqrt{2}\alpha_i}{4RTnb_{mix}}\frac{\partial}{\partial n_j}\left[log\left(\frac{nb_{mix}(1-\sqrt{2})+V}{nb_{mix}(1+\sqrt{2})+V}\right)\right]$$

$$- \frac{\partial\left(n^2 a_{mix}\right)}{\partial n_j}\frac{b_i}{RTnb_{mix}}\left[\frac{V}{V^2 + 2Vnb_{mix} - n^2 b_{mix}^2} + \frac{\sqrt{2}}{4nb_{mix}}\log\left(\frac{nb_{mix}(1-\sqrt{2})+V}{nb_{mix}(1+\sqrt{2})+V}\right)\right]$$

$$- \frac{n^2 a_{mix}b_i}{RT}\frac{\partial}{\partial n_j}\left(\frac{1}{nb_{mix}}\right)\left[\frac{V}{V^2 + 2Vnb_{mix} - n^2 b_{mix}^2} + \frac{\sqrt{2}}{4nb_{mix}}\log\left(\frac{nb_{mix}(1-\sqrt{2})+V}{nb_{mix}(1+\sqrt{2})+V}\right)\right]$$

$$- \frac{n^2 a_{mix}b_i}{RTnb_{mix}}\frac{\partial}{\partial n_j}\left[\frac{V}{V^2 + 2Vnb_{mix} - n^2 b_{mix}^2} + \frac{\sqrt{2}}{4nb_{mix}}\log\left(\frac{nb_{mix}(1-\sqrt{2})+V}{nb_{mix}(1+\sqrt{2})+V}\right)\right]$$

$$(149)$$

$$\frac{\partial}{\partial n_j}\left[log\left(\frac{nb_{mix}(1-\sqrt{2})+V}{nb_{mix}(1+\sqrt{2})+V}\right)\right] =$$

$$= +\frac{nb_{mix}(1+\sqrt{2})+V}{nb_{mix}(1-\sqrt{2})+V}\left[\frac{b_j(1-\sqrt{2})}{nb_{mix}(1+\sqrt{2})+V} - \frac{b_j(1+\sqrt{2})\left(nb_{mix}(1-\sqrt{2})+V\right)}{\left(nb_{mix}(1+\sqrt{2})+V\right)^2}\right]$$

$$= \frac{b_j(1-\sqrt{2})}{nb_{mix}(1+\sqrt{2})+V} - \frac{b_j(1-\sqrt{2})}{nb_{mix}(1+\sqrt{2})+V}$$

$$= \frac{b_j(1-\sqrt{2})\left(nb_{mix}(1+\sqrt{2})+V\right) - b_j(1+\sqrt{2})\left(nb_{mix}(1-\sqrt{2})+V\right)}{n^2 b_{mix}^2(1-\sqrt{2})(1+\sqrt{2}) + nb_{mix}V(1-\sqrt{2}) + nb_{mix}V(1+\sqrt{2}) + V^2}$$

$$= \frac{Vb_j(1-\sqrt{2}) - nb_j b_{mix} - (-nb_j b_{mix} + vb_j(1+\sqrt{2}))}{V^2 + 2Vnb_{mix} - n^2 b_{mix}^2}$$

$$= -\frac{2\sqrt{2}\,Vb_j}{V^2 + 2Vnb_{mix} - n^2 b_{mix}^2}$$

$$(150)$$

$$\frac{\partial \log(f_i)}{\partial n_j} = \frac{\delta_{ij}}{n_i} + \frac{b_j}{V - nb_{mix}} + \frac{b_i}{V - nb_{mix}} + \frac{nb_ib_j}{(V - nb_{mix})^2}$$

$$+ 2a_{ij}\frac{\sqrt{2}}{4RTnb_{mix}}log\left(\frac{nb_{mix}(1 - \sqrt{2}) + V}{nb_{mix}(1 + \sqrt{2}) + V}\right) - \frac{\alpha_ib_j}{n^2b_{mix}^2}\frac{\sqrt{2}}{4RT}log\left(\frac{nb_{mix}(1 - \sqrt{2}) + V}{nb_{mix}(1 + \sqrt{2}) + V}\right)$$

$$- \frac{2\sqrt{2}\sqrt{2}\alpha_ib_j}{4RTnb_{mix}}\frac{V}{V^2 + 2Vnb_{mix} - n^2b_{mix}^2}$$

$$- \frac{\alpha_jb_i}{RTnb_{mix}}\frac{V}{V^2 + 2Vnb_{mix} - n^2b_{mix}^2}$$

$$- \frac{\alpha_jb_i}{RTnb_{mix}}\frac{\sqrt{2}}{4nb_{mix}}\log\left(\frac{nb_{mix}(1 - \sqrt{2}) + V}{nb_{mix}(1 + \sqrt{2}) + V}\right)$$

$$+ \frac{n^2a_{mix}b_ib_j}{RTn^2b_{mix}^2}\left[\frac{V}{V^2 + 2Vnb_{mix} - n^2b_{mix}^2} + \frac{\sqrt{2}}{4nb_{mix}}\log\left(\frac{nb_{mix}(1 - \sqrt{2}) + V}{nb_{mix}(1 + \sqrt{2}) + V}\right)\right]$$

$$- \frac{n^2a_{mix}b_i}{RTnb_{mix}}\left[-\frac{V(2Vb_j - 2nb_{mix}b_j)}{(V^2 + 2Vnb_{mix} - n^2b_{mix}^2)^2} + \frac{\sqrt{2}}{4}\left(-\frac{b_j}{n^2b_{mix}^2}\right)\log\left(\frac{nb_{mix}(1 - \sqrt{2}) + V}{nb_{mix}(1 + \sqrt{2}) + V}\right)\right.$$

$$\left. + \frac{\sqrt{2}}{4nb_{mix}}\left(-\frac{2\sqrt{2}\,Vb_j}{V^2 + 2Vnb_{mix} - n^2b_{mix}^2}\right)\right] \tag{151}$$

$$\frac{\partial \log(f_i)}{\partial n_j} = \frac{\delta_{ij}}{n_i} + \frac{b_i + b_j}{V - nb_{mix}} + \frac{nb_ib_j}{(V - nb_{mix})^2}$$

$$+ \frac{\sqrt{2}}{4RTnb_{mix}}\left(2a_{ij} - \frac{\alpha_ib_j}{nb_{mix}} - \frac{\alpha_jb_i}{nb_{mix}} + 2\frac{n^2a_{mix}b_ib_j}{n^2b_{mix}^2}\right)log\left(\frac{nb_{mix}(1 - \sqrt{2}) + V}{nb_{mix}(1 + \sqrt{2}) + V}\right)$$

$$+ \frac{1}{RTnb_{mix}}\left(2\frac{n^2a_{mix}b_ib_j}{nb_{mix}} - \alpha_ib_j - \alpha_jb_i\right)\frac{V}{V^2 + 2Vnb_{mix} - n^2b_{mix}^2}$$

$$+ 2\frac{n^2a_{mix}b_ib_j}{RTnb_{mix}}\frac{V(V - nb_{mix})}{(V^2 + 2Vnb_{mix} - n^2b_{mix}^2)^2} \tag{152}$$

Equivalently, in intensive from

$$n\frac{\partial \log(f_i)}{\partial n_j} = \frac{\delta_{ij}}{x_i} + \frac{b_i + b_j}{v - b_{mix}} + \frac{b_i b_j}{(v - b_{mix})^2}$$
$$+ \frac{\sqrt{2}}{4RTb_{mix}} \left(2a_{ij} - \frac{\alpha_i b_j}{b_{mix}} - \frac{\alpha_j b_i}{b_{mix}} + 2\frac{a_{mix} b_i b_j}{b_{mix}^2}\right) \log\left(\frac{b_{mix}(1 - \sqrt{2}) + v}{b_{mix}(1 + \sqrt{2}) + v}\right)$$
$$+ \frac{1}{RTb_{mix}} \left(2\frac{a_{mix} b_i b_j}{b_{mix}} - \alpha_i b_j - \alpha_j b_i\right) \frac{v}{v^2 + 2vb_{mix} - b_{mix}^2}$$
$$+ 2\frac{a_{mix} b_i b_j}{RTb_{mix}} \frac{v(v - b_{mix})}{(v^2 + 2vb_{mix} - b_{mix}^2)^2} \tag{153}$$

or in compact notation, handy for numerical implementation

$$n\frac{\partial \log(f_i)}{\partial n_j} = \frac{\delta_{ij}}{x_i} + \frac{b_i + b_j}{c_0} + \frac{b_i b_j}{c_0^2}$$
$$+ c_3 c_4 c_5 \left(2a_{ij} - c_4 \alpha_i b_j - c_4 \alpha_j b_i + 2c_4^2 a_{mix} b_i b_j\right) c_2$$
$$+ c_4 c_5 \left(2c_4 a_{mix} b_i b_j - \alpha_i b_j - \alpha_j b_i\right) \frac{v}{c_1}$$
$$+ 2c_4 c_5 a_{mix} b_i b_j \frac{vc_0}{c_1^2} \tag{154}$$

where c_0-c_5 are defined as follow

$$c_0 = v - b_{mix} \tag{155}$$
$$c_1 = v^2 + 2vb_{mix} - b_{mix}^2 \tag{156}$$
$$c_2 = \log\left(\frac{b_{mix}(1 - \sqrt{2}) + v}{b_{mix}(1 + \sqrt{2}) + v}\right) \tag{157}$$
$$c_3 = \frac{\sqrt{2}}{4} \tag{158}$$
$$c_4 = \frac{1}{b_{mix}} \tag{159}$$
$$c_5 = \frac{1}{RT} \tag{160}$$

Implementation notes

Only the method of Heidemann and Khalil has been implemented for mixtures of arbitrary number of species; this is due to the well known properties of robustness and speed of the method [37, 1, 19, 32]. The actual implementation is a bounded Newton-Raphson method [38] and uses the difference in temperature between iterations to check convergence. For further information regarding the method implementation and testing refer to [8].

B Initial profile derivation

This appendix duplicates information available in [27].

B.1 Mean profiles

The mean profiles are only functions of x_2

$$u_1(x_2) = u_1(x_{2,min}) + \left[1 + erf\left(\frac{\sqrt{\pi}x_2}{\delta_{\omega,0}}\right)\right]\frac{1}{2}\left[u_1(x_{2,max}) - u_1(x_{2,min})\right] \tag{161}$$

$$T(x_2) = T(x_{2,min}) + \left[1 + erf\left(\frac{\sqrt{\pi}x_2}{\delta_{\omega,0}}\right)\right]\frac{1}{2}\left[T(x_{2,max}) - T(x_{2,min})\right] \tag{162}$$

$$Y_\alpha(x_2) = Y_\alpha(x_{2,min}) + \left[1 + erf\left(\frac{\sqrt{\pi}x_2}{\delta_{\omega,0}}\right)\right]\frac{1}{2}\left[Y_\alpha(x_{2,max}) - Y_\alpha(x_{2,min})\right] \tag{163}$$

$$p = p_\infty, \quad u_2 = 0, \quad u_3 = 0 \tag{164}$$

$$\frac{\partial u_1}{\partial x_2} = \frac{\left[u_1(x_{2,max}) - u_1(x_{2,min})\right]}{\delta_{\omega,0}}\exp\left[-\left(\frac{\sqrt{\pi}x_2}{\delta_{\omega,0}}\right)^2\right] = \frac{\Delta U_0}{\delta_{\omega,0}}\exp\left[-\left(\frac{\sqrt{\pi}x_2}{\delta_{\omega,0}}\right)^2\right] \tag{165}$$

where $u_1(x_{2,max}) = U_U$ and $u_1(x_{2,min}) = U_L$ where L_2 is the length of the domain in the x_2 direction. The values of U_U and U_L are obtained by invoking a null convective velocity U_c computed according to [36] as

$$U_c = \frac{\sqrt{\rho_U}U_U + \sqrt{\rho_L}U_L}{\sqrt{\rho_U} + \sqrt{\rho_L}}. \tag{166}$$

For $U_c = 0$, and defining a_s the speed of sound,

$$U_U = \frac{2M_c a_{sU}}{\left(1 + \frac{a_{sU}}{a_{sL}}\sqrt{\frac{\rho_U}{\rho_L}}\right)}, \quad U_L = -\sqrt{\frac{\rho_U}{\rho_L}}U_U. \tag{167}$$

B.2 Perturbations

The simulations are started with streamwise and spanwise vorticity perturbations superimposed on the mean initial velocity profile

$$\omega_1(x_2, x_3) = F_{3D}\frac{\lambda_3 \Delta U_0}{\Gamma_1}f_2(x_2)f_3(x_3) \tag{168}$$

$$\omega_3(x_1, x_2) = F_{2D} \frac{\lambda_1 \Delta U_0}{\Gamma_3} f_1(x_1) f_2(x_2) \tag{169}$$

where Γ_1 and Γ_3 are the circulations,

$$f_1(x_1) = A_k \sin\left(\frac{2\pi x_1}{2^k \lambda_1}\right) \tag{170}$$

$$f_2(x_2) = \exp\left[-\pi \left(\frac{x_2}{\delta_{\omega,0}}\right)^2\right] \tag{171}$$

$$f_3(x_3) = B_k \sin\left(\frac{2\pi x_3}{2^k \lambda_3}\right) \tag{172}$$

Unlike for simulations for binary-species systems [33, 34], for each vorticity component (ω_1, ω_3), the velocity components are computed from the analytical solution of a system consisting of the vorticity component equation

$$\omega_1 = \frac{\partial u_3}{\partial x_2} - \frac{\partial u_2}{\partial x_3}, \quad \omega_2 = \frac{\partial u_1}{\partial x_3} - \frac{\partial u_3}{\partial x_1}, \quad \omega_3 = \frac{\partial u_2}{\partial x_1} - \frac{\partial u_1}{\partial x_2} \tag{173}$$

and the divergence-free condition. To ensure divergence-free initial conditions, the analytical perturbation is obtained separately for each wavelength ($2^k \lambda_1$ and $2^k \lambda_3$), and then the perturbations are added together after being weighted according to A_k or B_k. The analytical perturbation at a given wavelength is separately derived for the spanwise and streamwise directions. Let u_i and ω_i be the generic perturbation velocity and perturbation vorticity fields. In a x_3 plane, for the spanwise vorticity

$$\frac{\partial u_2}{\partial x_1} - \frac{\partial u_1}{\partial x_2} = \omega_3 \tag{174}$$

$$\frac{\partial u_1}{\partial x_1} + \frac{\partial u_2}{\partial x_2} = 0. \tag{175}$$

Introducing wavelength $n\lambda_1$ (wavenumber $\alpha_n = 2\pi/(n\lambda_1)$) we define

$$\alpha_n^* = \alpha_n \delta_{\omega,0}, \quad x_2^* = \frac{x_2}{\delta_{\omega,0}}, \quad \hat{\omega}_3^* = \hat{\omega}_3 \delta_{\omega,0} \tag{176}$$

and the perturbations

$$u_1 = \hat{u}_1(x_2^*) \exp(i\alpha_n^* x_1^*), \quad u_2 = \hat{u}_2(x_2^*) \exp(i\alpha_n^* x_1^*) \quad \omega_3 = \hat{\omega}_3(x_2^*) \exp(i\alpha_n^* x_1^*) \tag{177}$$

where $\hat{u}_1$, $\hat{u}_2$ and $\hat{\omega}_3$ are the perturbation amplitudes. Solving (174) and (175) for the form of (177) and applying far field boundary conditions $\hat{u}_2(x_{2,min}) = 0$ and $\hat{u}_2(x_{2,max}) = 0$ yields

$$\hat{u}_1 = ia_1 \exp(\alpha_n^* x_2^*) - ia_2 \exp(-\alpha_n^* x_2^*), \tag{178}$$

$$\hat{u}_2 = a_1 \exp(\alpha_n^* x_2^*) + a_2 \exp(-\alpha_n^* x_2^*), \tag{179}$$

where

$$a_1 = i\frac{1}{4} \exp\left[\left(\frac{\alpha_n^*}{2\sqrt{\pi}}\right)^2\right] \left[erf\left(\sqrt{\pi}x_2^* + \frac{\alpha_n^*}{2\sqrt{\pi}}\right) - 1\right], \tag{180}$$

$$a_2 = -i\frac{1}{4} \exp\left[\left(\frac{\alpha_n^*}{2\sqrt{\pi}}\right)^2\right] \left[erf\left(\sqrt{\pi}x_2^* - \frac{\alpha_n^*}{2\sqrt{\pi}}\right)^2 + 1\right]. \tag{181}$$

A similar solution is obtained for the streamwise vorticity perturbation by solving the equations

$$\frac{\partial u_2}{\partial x_3} - \frac{\partial u_3}{\partial x_2} = -\omega_1,$$

$$\frac{\partial u_3}{\partial x_3} + \frac{\partial u_2}{\partial x_2} = 0,$$

in a x_1 plane with boundary conditions $\hat{u}_2(x_{2,min}) = 0$ and $\hat{u}_2(x_{2,max}) = 0$. Formally, we replace x_1 by x_3, λ_1 by λ_3 (the relevant wavelength is $n\lambda_3$(wavenumber $\alpha_n = 2\pi/(n\lambda_3)$)), u_1 by u_3 and ω_3 by $(-\omega_1)$. The final result is

$$\hat{u}_3 = ia_1 \exp(\alpha_n^* x_2^*) - ia_2 \exp(-\alpha_n^* x_2^*) \tag{182}$$

$$\hat{u}_2 = a_1 \exp(\alpha_n^* x_2^*) + a_2 \exp(-\alpha_n^* x_2^*) \tag{183}$$

with the same formal expressions (180) and (181) for a_1 and a_2, but where α_n^* is now related to λ_3 instead of to λ_1.

References

[1] Abu-Eishah, S. I., Darwish, N. A., and Aljundi, I. H. Prediction of critical properties of binary mixtures using the prsv-2 equation of state. International journal of thermophysics, 19(1):239–258, 1998.

[2] Almagro, A., Garcia-Villalba, M., & Flores, O. 2017 A numerical study of a variable-density low-speed turbulent mixing layer. Journal of Fluid Mechanics 830, 569-601.

[3] Basilevsky, A. T., Head, J. W. 2003 The surface of Venus. Rep. Prog. Phys. 66 1699

[4] Batchelor, G. K. 1999 An Introduction to Fluid Dynamics. Cambridge University Press.

[5] Bellan, J. 2017 Direct numerical simulation of a high-pressure turbulent reacting temporal mixing layer. Combustion and Flame **176**, 245–262.

[6] Bengtsson, L., Bonnet, R. M., Grinspoon, D., Koumoutsaris, S., Lebonnois, S., Titov, D. 2013 Towards Understanding the Climate of Venus - Applications of Terrestrial Models to Our Sister Planet. ISSI Scientific report Series.

[7] Blumenthal, G., Kay, L., Palen, S., Smith, B., 2012 Understanding Our Universe. New York: W.W. Norton & Company. p. 167.

[8] Castiglioni, G., Bellan, J., 2018 On models for predicting thermodynamic regimes in high-pressure turbulent mixing and combustion of multispecies mixtures. J. Fluid Mech., vol. 843, pp. 536-574.

[9] Castiglioni, G. 2018, personal communication.

[10] De Groot, S. R., Mazur, P. 1984 Non-equilibrium Thermodynamics. Dover.

[11] Debenedetti, P. G. Metastable liquids: concepts and principles. Princeton University Press, 1996.

[12] Duncan, J. B. & Toor, H. L. 1962 An experimental study of three component gas diffusion. AIChE J. 8 (1), 38-41.

[13] Dutt, A., Limaye, S. S., 2018 Adiabatic Lapse Rate and Static Stability in the Venus Atmosphere calculated from Real Gas Mixture Models. arXiv:1806.06835 [astro-ph.EP].

[14] Ern, A. & Giovangigli, V. 1998 Thermal diffusion effects in hydrogen–air and methane–air flames. Combust. Theory Modelling **2**, 349-372.

[15] Gaitonde, D. V., & Visbal, M. R. 1998 High-order schemes for Navier-Stokes equations: algorithm and implementation into FDL3DI. Air Force Research Lab Wright-Patterson AFB OH Air Vehicles Directorate AFRL-VA-WP-TR-1998-3060.

[16] Harstad, K. G., Bellan, J., 2011 Computation of Laminar Premixed Flames Using Reduced Kinetics Based on Constituents and Species. AIAA.

[17] Harstad, K. & Bellan, J. 2004b High-pressure binary mass-diffusion coefficients for combustion applications. Ind. & Eng. Chem. Res. **43**(2), 645–654.

[18] Harstad, K. & Bellan, J. 2004a Mixing rules for multicomponent mixture mass diffusion coefficients and thermal diffusion factors. J. Chem. Phys. **120**(12), 5664–5673.

[19] Heidemann, R. A. and Khalil, A. M. The calculation of critical points. AIChE journal, 26(5):769–779, 1980.

[20] Hirshfelder, J., Curtis, C. & Bird, R. 1964 Molecular Theory of Gases and Liquids. John Wiley and Sons.

[21] Holton, J. R. 2004 An Introduction to Dynamic Meteorology. Academic Press. p. 64. ISBN 0-12-354015-1.

[22] Jacobson, N. S., et al., 2017 Thermodynamic Constraints in the Lower Atmosphere of Venus. ACS Earth and Space Chem. 1,422-430

[23] Kennedy, C. & Carpenter, M. 1994 Several new numerical methods for compressible shear layer simulations. Appl. Num. Math. **14**, 397–433.

[24] Knapp, H., Döring, R., Oellrich, L., Plöcker, U., & Prausnitz, J. M. 1982 Vapor-liquid Equilibria for Mixtures of Low Boiling Substances, vol VI. Dechma

[25] Landis, G. A., Colozza, A., LaMarre, C. M. 2002 Atmospheric Flight on Venus. NASA/TM-2002-211467. AIAA-2002-0819.

[26] Lele, S. K. 1992 Compact finite difference schemes with spectral-like resolution. Journal of computational physics **103(1)**, 16–42.

[27] Masi, E., Bellan, J., Harstad, K. G., & Okong'o, N. A., 2013 Multi-species turbulent mixing under supercritical-pressure conditions: modelling, direct numerical simulation and analysis revealing species spinodal decomposition. J. Fluid Mech. 721, 578-626.

[28] Moser, R. & Rogers, M. 1991 Mixing transition and the cascade to small scales in a plane mixing layer. Phys. Fluids A **3**(5), 1128–1134.

[29] Moshkin, B. E.; Ekonomov, A. P.; Golovin, Iu. M. 1979 Dust on the surface of Venus. Cosmic Research, vol. 17, no. 2, Sept., p. 232-237.

[30] Muller, S. M. & Scheerer, D. 1991 A method to parallelize tridiagonal solvers. Parallel Computing **17**, 181–188.

[31] National Institute of Standards and Technology. Website: https://webbook.nist.gov/chemistry/fluid/

[32] Nichita, D.V., and Gomez, S. Efficient and reliable mixture critical points calculation by global optimization. Fluid Phase Equilibria, 291(2):125–140, 2010.

[33] Okong'o, N., Harstad, K., & Bellan, J. 2002 Direct numerical simulations of O_2/H_2 temporal mixing layers under supercritical conditions. AIAA J. **40**(5), 914–926.

[34] Okong'o, N. & Bellan, J. 2002a Direct numerical simulations of a transitional supercritical binary mixing layer: heptane and nitrogen. J. Fluid Mech. 464, 1-34.

[35] Pantano, C., & Sarkar, S. 2002 A study of compressibility effects in the high-speed turbulent shear layer using direct simulation. J. Fluid Mech. 451, 329-371.

[36] Papamoschou, D. & Roshko, A. 1988 The compressible turbulent shear layer: an experimental study. J. Fluid Mech. 197, 453-477.

[37] Poling, B. E., Prausnitz, J. M., & O'Connell, J. P., 2001 The Properties of Gases and Liquids. McGraw-Hill.

[38] Press, W. H., Teukolsky, S. A., Vetterling, W. T. and Flannery, B.P. Numerical recipes in fortran, 1992.

[39] Reid, R. C., Prausnitz, J. M., Poling, B. E. 1987 The Properties of Gases and Liquids. 4th edn. McGraw-Hill.

[40] Seiff, A., et al., 1985 Models of The Structure of The Atmosphere of Venus from the Surface to 100 kilometers Altitude. Adv. Space Res. Vol. 5, No. 11, pp. 3-58.

[41] Svedhem, H. S., Titov, D. V., Taylor, F. V., Witasse, O. 2007 Venus as a more Earth-like planet. Nature. 450 (7170): 629–632.

[42] Taylor, R. & Krishna, R. 1993 Multicomponent Mass Transfer, Wiley Series in Chemical Engineering. Wiley.

[43] Tester, J. W., Modell, M., Thermodynamics and its applications. Prentice Hall PTR, 1997

[44] Tester, J. W., Modell, M., Thermodynamics and Its Applications. 3rd edition. Prentice Hall International Series.

[45] Wyngaard, J. C. 1992 Atmospheric Turbulence. Annu. Rev. Fuid Mech. 24: 205-33.